Optomechanical Manipulation of Particles and Biological Systems at the Mesoscale

Carla Pernpeintner

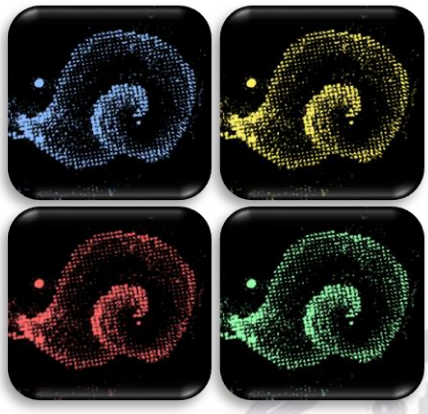

Optomechanical Manipulation of Particles and Biological Systems at the Mesoscale

Dissertation

an der Fakultät für Physik der

Ludwig-Maximilians-Universität München

vorgelegt von

Carla Pernpeintner

aus München

München

Juli 2017

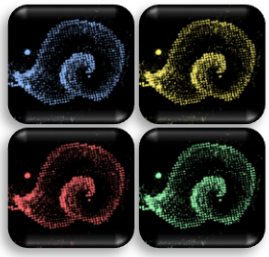

Cover: pseudocolor picture of laser reflection on the cover slide of a holographic optical tweezer image (dark-field microscopy)

Erstgutachter:	PD Dr. Theobald Lohmüller
Zweitgutachter:	Prof. Dr. Jan Lipfert
Datum der Abgabe:	18. Juli 2017
Datum der Verteidigung:	19. Oktober 2017

Zusammenfassung

Kraftspektroskopie auf der Mikro- und Nanoskala unter annähernd physiologischen Bedingungen ist eine besondere Herausforderung, da unter diesn Umständen kleine Bewegungen von nanoskaligen Objekten von thermischen Fluktuationen dominiert werden. Mit optische Pinzetten ist es möglich Kräfte von wenigen Pikonewton (10^{-12} N) mit hoher Auflösung in Raum und Zeit zu messen. Um eine noch höhere Sensitivität für kleine Kräfte zu erreichen, wurden in dieser Arbeit neue Konzepte entwickelt, die auf einer Kombination des Lock-in Prinzips und optischer Kraftdetektion beruhen.

Im Vergleich zu chemischen oder mechanischen Manipulationstechniken sind optische Methoden sowohl vielseitig anwendbar als auch reversibel. Sie besitzen zudem einen hohen Grad an räumlicher und zeitlicher Auflösung. In dieser Arbeit wurde demonstriert, dass es möglich ist, ein biologisches Modellsystem mithilfe photoschaltbarer Phospholipide optisch zu kontrollieren. Es wurde gezeigt, dass die mechanischen Eigenschaften von Vesikelmembranen, die vollständig aus solchen Photolipiden aufgebaut sind, mittels optischer Anregung im UV-Bereich stark beeinflusst werden können. Beispielsweise ermöglichte das optische Schalten einer Vesikelmembran zwischen einem "harten" und einem "weichen" Zustand kontrollierte Formveränderungen des ganzen Vesikels. Darüber hinaus wurde eine Methode entwickelt, um mechanische Arbeit lokal zu speichern, die bei Bedarf mithilfe eines Lichtimpulses abrufbar ist.

Im nächsten Schritt wurde der Einfluss der mechanischen Eigenschaften ganzer Zellen auf die umgebende Mikrofluidik untersucht. Hierzu wurden einzelne Zellen mit holographischen optischen Pinzetten periodisch geschüttelt. Ein in der Nähe der Zelle positioniertes, optisch gefangener Partikel diente zur gleichzeitigen Detektion des fluidischen Feldes. Die Trajektorie des Partikels wurde dazu im Fourierraum analysiert. Ein Vergleich der charakteristischen Fourierspektren einzelner Zellen ermöglichte so, Veränderungen mechanischer Parameter der Zelle oder des umgebenden Fluids zu analysieren.

Um die Grenzen der Kraftauflösung mittels optofluidischer Detektion zu quantifizieren, wurde ein optisch gefangenes Goldnanopartikel als Kraftdetektor verwendet. Durch Beleuchtung mit Licht, dessen Wellenlänge in Resonanz mit dem Partikelplasmon gewählt wurde, konnte der Partikel um wenige Nanometer gegenüber seiner Gleichgewichtsposition ausgelenkt werden. Grund für die Auslenkung sind optische Streukräfte, die mittels einer spektralen Analyse der Brownschen Bewegung des Partikels mit einer Genauigkeit von

weniger als 3 Femtonewton ($3 \times 10^{-15}\,\mathrm{N}$) bestimmt werden konnten. Laut Fachliteratur ist dies die kleinste schaltbare Kraft, die in Fluid und bei Raumtemperatur gemessen wurde. In einer ersten Anwendung wurde diese sensitive Methode eingesetzt, um fluidische Kräfte im Umfeld einer lichtgetriebene Mikroschraube und eines optisch gefangenen Bakteriums zu bestimmen.

Die Ergebnisse dieser Arbeit könnten dazu beitragen, intra- und interzelluläre Kraftmessungen mit einer Auflösung von wenigen Femtonewton und in Gegenwart thermischer Kräfte zu realisieren. Die gezielte Anwendung und hochaufgelöste Messung kleinster Kräfte bietet außerdem eine vielversprechende experimentelle Grundlage für optomechanische Manipulation auf der Nanoskala.

Abstract

When approaching physiological conditions, force spectroscopy on the nano- and microscale becomes challenging as small deflections of nanoscale objects are usually overwhelmed by thermal fluctuations. Optical tweezers have become an established tool to investigate forces down to a few piconewtons (10^{-12} N) with high spatiotemporal precision. In this thesis, optical force detection is combined with a lock-in approach in order to reach even lower force regimes. The novel concepts presented are more sensitive compared to the state-of-the-art technologies.

Compared to chemical or mechanical manipulation of matter, light is a versatile and reversible type of stimulation with a high level of spatiotemporal control. Here, optical switching of a biological model system was demonstrated using photoswitchable phospholipids. It was shown that UV light excitation of vesicle membranes entirely made of such photolipids can significantly change the mechanical properties of these bilayers. Photoswitching the vesicle membrane between a rigid and a soft state enabled controlled shape transitions of the entire vesicle. Furthermore, a strategy was devised for locally storing mechanical energy that could be released on demand by irradiation with visible light.

Moving from the investigation of vesicles to entire cells, the impact of the mechanical properties of moving cells on the surrounding microfluidics was explored. With the use of holographic optical tweezers, individual cells were shaken periodically. At the same time, the microfluidic field was detected by an optically trapped detector particle in close vicinity to the cell. Its trajectory was subsequently analyzed in Fourier space. By comparing the characteristic Fourier spectra, changes in mechanical parameters of either the cell or its fluidic environment could be discerned.

Finally, to quantify the limits of force resolution in optofluidic detection, an optically trapped gold nanoparticle was used as a sensitive force detector. Illumination of the particle with light resonant with its plasmon frequency resulted in a displacement of the particle of only a few nanometers from its equilibrium position. The reason are optical scattering forces that could be revealed to be less than 3 fN (3×10^{-15} N) by a spectral analysis of the particle's Brownian motion. To date, this is the smallest reported switchable force that was measured in fluid at room temperature. In a first application, the method was used to quantify fluidic forces around a light-driven micro-screw and an optically trapped bacterium.

The results of this thesis are valuable, e. g., for the realization of intra- and intercellular force measurements that require fN resolution in the presence of thermal forces. The possibility to apply and measure small forces provides a promising experimental platform for optomechanical manipulation on the nanoscale.

List of Publications

Scientific publications of results presented in this work

C. Pernpeintner[#], J.A. Frank[#], P. Urban, C.R. Roeske, S. Pritzl, D. Trauner[*], and T. Lohmüller[*]. Light-controlled membrane mechanics and shape transitions of photoswitchable lipid vesicles; *Langmuir* **33**, 4083 (2017); doi: 10.1021/acs.langmuir.7b01020

C. Zensen[#], N. Villadsen[#], F. Winterer, S.R. Keiding, and T. Lohmüller[*]. Pushing nanoparticles with light - A femtonewton resolved measurement of optical scattering forces; *APL Photonics* **1**, 026102 (2016); doi: 10.1063/1.4945351

C. Zensen, I.E. Fernandez, O. Eickelberg, J. Feldmann, and T. Lohmüller[*]. Detecting swelling states of red blood cells by "cell-fluid coupling spectroscopy"; *Advanced Science* **4**, 1600238 (2016); doi: 10.1002/advs.201600238

C. Pernpeintner[#], S.R. Kirchner[#], C. Schamel, A. Mader, P. Urban, L.J. Anderson, M. Opitz, P. Fischer, T. Lohmüller[*], and J. Feldmann. Measurement of the flow field around colloidal micro-screws and the bacterium *Bacillus Subtilis*; *in preparation.*

Additional publications in the course of the PhD thesis

K. Stoiber, O. Naglo, C. Pernpeintner, S. Zhang, A. Koeberle, M. Ulrich, O. Werz, R. Müller, S. Zahler, T. Lohmüller, J. Feldmann, and S. Braig[*]. Targeting de novo lipogenesis as a novel approach in anti-cancer therapy; *British Journal of Cancer* (published online november 2017); doi: 10.1038/bjc.2017.374

B. Buchmann, F.M. Hecht, C. Pernpeintner, T. Lohmüller, and A.R. Bausch[*]. Controlling non-equilibrium structure formation on the nanoscale; *ChemPhysChem* (published online october 2017); doi: 10.1002/cphc.201700844

F. Winterer, C.M. Maier, C. Pernpeintner, and T. Lohmüller[*]. Optical controlled guiding and manipulation of gold nanoparticles by thermocapillary convection; *in review.*

P. Urban, S. Pritzl, C. Pernpeintner, J.A. Frank, C. Roeske, D. Trauner, and T. Lohmüller*. Reversible aggregation of photoswitchable lipids in multicomponent bilayers; *in preparation.*

C. Zensen, K. Schönleber, F. Kemeth, and K. Krischer*. A capacitance mediated positive differential resistance oscillator model for electrochemical systems involving a surface layer; *The Journal of Physical Chemistry C* **118**, 24407 (2014); doi: 10.1021/jp505418x

K. Schönleber, C. Zensen, A. Heinrich, and K. Krischer*. Pattern formation during the oscillatory photoelectrodissolution of n-type silicon: turbulence, clusters and chimeras; *New Journal of Physics* **16**, 063024 (2014); doi: 10.1088/1367-2630/16/6/063024

N. Elkhatib, M.B. Neu, C. Zensen, K.M. Schmoller, D. Louvard, A.R. Bausch, T. Betz, and D.M. Vignjevic*. Fascin plays a role in stress fiber organization and focal adhesion disassembly; *Current Opinion in Biology* **24**, 1492 (2014); doi: 10.1016/j.cub.2014.05.023

# – equal contributions; ∗ – corresponding author

Conference Contributions and Awards

Oral presentations

Probing Mechanobiological Properties of Cells Using Holographic Optical Tweezers;
Workshop on Photonics and Optoelectronics in Riezlern, September 2014.

Optical Shaking of Single Cells;
DPG spring meeting in Berlin, March 2015.

Pushing (at) the Limits of Resolution;
NIM summer retreat in Fall/Lenggries, July 2015.

Trapping, Shaking and Pulling Biological Objects with Light;
Aarhus University (Invited Talk) in Aarhus/Denmark, August 2015.

Ultrasensitive and Directional Force Spectroscopy in Living Cells (Poster Talk);
NIM winter school in Austria, March 2016.

Tuning Shape and Mechanical Propertiesof *azo*–**PC** Vesicles with Light;
Photonics and Optoelectronics with New Materials in Lenggries, July 2016.

Underwater Nanomusic;
Science Rocks (Invited Talk) in München, January 2017.

From Cell Biology to Biophysical Membrane Models;
Photonics and Optoelectronics with New Materials in Siracusa/Sicily, March 2017.

Small, Warm and Alive: Challenges of Optical Force Spectroscopy at the Mesoscale;
TOPTICA developers' seminar (Invited Talk) in München, May 2017.

Poster presentations

Direct optical monitoring of flow generated by bacterial flagellar rotation;
Bionanomed, Austria, March 2014.
> **Poster Award of the Erwin Schrödinger Society** (3rd prize)

Holographic Manipulation of Biologic Matter;
NIM summer retreat, Tegernsee, March 2014.
> **NIM Poster Award 2014** (1st prize)

"Optical Shaking" of Red Blood Cells: A Strategy to Measure Cell-Fluid Coupling with Optical Tweezers; *60th Meeting of the Biophysical Society*, LA/USA, February 2016.
> funded by **CeNS Travel Award**

fN-resolved Determination of Optical Forces acting on a Single Gold Nanoparticle;
CeNS Workshop, Venice, September 2015.

Ultrasensitive and Directional Force Spectroscopy in Living Cells;
NIM winter school, Austria, March 2016.
> **NIM Poster Award 2016** (1st prize)

Other

Contribution to "TARDIGRADIA – von mikrobiotischen Lebenskünstlern";
Ein Radiofeature von Maria A. Schmidt, Masterarbeit Bauhaus-Universität Weimar, 2017.

Presentation of "Nanopartikel für biomedizinische Diagnostik";
NIM Nanoday, Deutsches Museum, München, 2014.

NIM – Nanosystems Initiative Munich, CeNS – Center of Nanoscience

Contents

Zusammenfassung **I**

Abstract **III**

1 Introduction: *Welcome to the Mesoscale!* **1**

2 Fundamentals: Optomechanical Manipulation of Small Particles **5**

2.1 Types and magnitudes of forces at small scales 6

2.2 Fluidic forces on small particles 6

2.3 Interaction of small particles with visible light 13

2.4 Theory of optical tweezers 20

3 Experimentals: From Particle Trapping to Cell Tracking **27**

3.1 Laser microscopy and optical spectroscopy 27

3.2 Data acquisition and processing 33

3.3 Samples and materials 37

4 Manipulation of Phospholipid Vesicle Mechanics with Light **41**

4.1 Vesicles as a biomechanical model system 42

4.2 Controlling vesicle shape and mechanics with light 46

4.3 Local storage of mechanical energy 52

4.4 *Discussion:* Switching membrane mechanics with light 55

5 Cell-Fluid Coupling Spectroscopy **59**

5.1 The cell as a mechanical filter 60

5.2 Distinguishing swelling states of RBCs 66

5.3 Dynamical mechanical analysis of single cells 71

5.4 *Discussion:* Cell-fluid coupling in biomechanics 76

6 Optofluidic Force Measurement with Optically Trapped Particles **79**

6.1 Principle of fN-resolved force measurements 80

6.2 Measuring the scattering force on plasmonic particles 83
6.3 Detection and measurement of fluidic force fields 90
6.4 *Discussion:* Optical measurement of fN forces in biological systems 96

7 Conclusion: *Controlling Mesoscale Mechanics with Light* **101**

A Appendix **103**
A.1 Molecular collision frequency and speed 103
A.2 Fourier transform of the periodic step force $F_{\text{ext}}(t)$ 105
A.3 Maximum error calculation 106
A.4 Optical heating of a gold nanoparticle 107
A.5 Reaction scheme of *azo*–**PC** 109
A.6 Measured vesicle bending rigidities 110

Bibliography **111**

List of Abbreviations and Variables **125**

Acknowledgements **129**

Chapter 1

Introduction: *Welcome to the Mesoscale!*

The definition of a *mesoscale*, literally meaning 'in-between-scale', clearly depends on the scientific field of interest. For example, the metereological mesoscale lies between 2 and 2000 km [1], whereas the mesoscale of condensed matter and biological physics, illustrated in Fig. 1.1, ranges between the size of an individual atom (Å) and a single cell (10 µm). It is this regime which will be considered in the following.

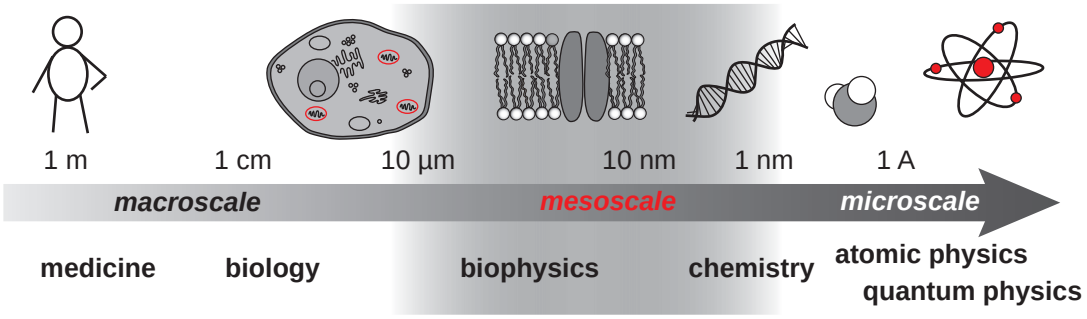

Figure 1.1 – Illustration of the mesoscopic regime. The mesoscale ranges roughly between the size of an individual atom (Å) and a single cell (10 µm). Each length scale corresponds to a certain field of science and associated techniques.

Techniques to perform physical measurements usually correspond to characteristic length scales, indicating wether an approach is *macroscopic* or *microscopic*. For various scales, the underlying principle of many investigations is a coupling of optical means of manipulation to mechanical degrees of freedom. Here, applications range from the ability to cool down atoms and ions in atomic physics [2], gravitational wave interferometry in cavity optomechanics [3], and single-molecule force spectroscopy in biophysics [4, 5]. The difficulties in force spectroscopy of mesoscale systems, however, cannot be underestimated. Many approximations providing simplified models that are valid either on very small or on very large scales, fail. To give an example, for a description of light-matter interaction of objects whose diameter is comparable to the wavelength of visible light, neither ray geometric optics nor the Rayleigh approximation can be considered alone. Furthermore, for mesoscopic particles, both classical and quantum effects can play a role. Hence, while on

the subnanometer scale and the large microscale, optomechanical manipulation is already an established technique that enables precise force determination, in between, quantitative force measurements are not as well explored [3, 6].

The goal of this work is to develop novel optical techniques that are useful to detect and quantify small changes in mechanical parameters on the mesoscale. Optical tweezers, which are generated by tightly focused laser beams that can hold a particle in the focal spot of highest laser intensity [7], have turned out to be the method of choice when it comes to reaching the detection limits [4, 8]. Most approaches investigated in this thesis are based on using an optically trapped nano- or microscopic particle as a sensitive force detector. Interestingly, this idea dates back to A. Einstein who already suggested Brownian particles as versatile molecular probes of the environment more than 100 years ago [9]. The sensitive detection of nanoscale vibrations using an optically trapped gold nanoparticle (*optofluidic detection*) [10] was recently applied to record characteristic vibration spectra of biological [11, 12] and microfluidic systems [13]. In the present work, I take a step further and extend the technique of optofluidic detection by introducing active mechanical manipulation to the system.

When dealing with biological samples, it is desirable to carry out the experiments close to physiological conditions. This means that rather high temperatures (at least room temperature, $T \approx 300\,\mathrm{K}$) and the presence of ions in the liquid medium should not be in conflict with the respective measurement conditions. Also, experimental time scales and laser powers must be chosen appropriately to avoid photodamage of the samples. For most biophysical applications, the dynamics can be assigned between the microscopically fast and the macroscopically slow as

$$k_B T \approx 4\,\mathrm{pN\,nm} \qquad \text{and} \qquad k_B T/\eta \approx 4\,\mu\mathrm{m}^3/\mathrm{s}, \tag{1.1}$$

with η being the viscosity of the liquid environment for room temperature [14]. The regime where Eqs. (1.1) are applicable is however dominated by fluctuations and thermal forces. These fluctuations are literally quite vital here, since living systems function out of equilibrium [15]. At the same time, these circumstances do not only complicate biological communication on a molecular level but also impose challenges on the experimental realization and theoretical description of quantitative force measurements at the mesoscale. In this work, it is demonstrated that analytical modelling based on the Langevin equation enables a successful measurement of biologically relevant periodic femtonewton (fN, $10^{-15}\,\mathrm{N}$) forces below the Brownian noise threshold.

This thesis is organized as follows: In the theory chapter, the fundamentals of optomechanical manipulation of small particles are reviewed. Fluidic and optical forces are introduced from a theoretical point of view, giving the most important equations. In Chapter 3, experimental setups as well as evaluation routines will be presented. Chapters 4 to 6 form the Results part of the PhD thesis.

In Chapter 4, it will be demonstrated that shape transitions such as budding or pearling of vesicles made from azobenzene containing phospholipids can be induced by optical stimulation. The observations are explained with a decrease in bending rigidity of up to 1.5 orders of magnitude on UV-A illumination. Commonly, shape and other mechanical properties are tuned by parameters like temperature or chemical composition, which suffer from long ramping times, irreversibility or lack in physiologic compatibility [16, 17]. The use of light as a stimulus allows for switching phospholipid vesicles mechanics within seconds and thus represents a promising model systems for shape and mechanics of biological membranes.

In Chapter 5, I turn from the investigation of material properties of cell models towards cell-fluid coupling experiments. This is a rather unexplored field even though it is known that cell movement is strongly depending on the rigidity of substrate [18, 19] and a similar effect might be possible for the surrounding fluid. The fluid-mediated transduction of the cell's mechanical response to a mechanical stimulus is described in terms of signal processing. Optical tweezers were used to both detect and create a microflow around an individual cell. In proof-of-principle experiments, red blood cells and two different cancer cell lines were tested. As fluctuations dominate in fluid at room temperature, in-fluid measurements require a subtle strategy to distinguish directed forces from ubiquitous thermal forces.

In Chapter 6, the quantitative resolution limits of optical tweezer based force measurements in case of a periodic stimulus are investigated. At the example of a plasmonic nanoparticle exposed to optical scattering forces, a force resolution of only 2.2 fN could be demonstrated. To the best of my knowledge, this is the smallest force ever measured by optical tweezers [6, 20]. The strategy is then applied to determine force fields around a colloidal micro-screw and a single bacterial cell.

Every chapter concludes with a discussion of the results where the applicability of the developed strategies to biological systems is carved out, and an outlook to possible future experiments is given. In Chapter 7, all findings are summarized.

Chapter 2

Fundamentals: Optomechanical Manipulation of Small Particles

Though its large importance for biological systems, the mesoscale is difficult to handle from both an experimental and a theoretical perspective. The main reason is that at all times, mechanical stimulation is in competition with thermal fluctuations. A thermal equilibrium can hardly be assumed in these systems where dissipation plays a crucial role. Furthermore, at small length scales, fluid dynamics is strikingly different compared to the macroscopic world [21, 22]. A famous example is the 'scallop theorem' [23] stating that a mesoscopic swimmer must deform time-invariantly in order to achieve propulsion in a Newtonian fluid. In order to qualitatively capture the characteristics of flow for a given flow speed v and length scale L, the dimensionless Reynolds number,

$$Re = \frac{\rho \cdot L \cdot v}{\eta}, \tag{2.1}$$

is an extremely helpful quantity. It describes the ratio of inertial and viscous forces [24, 25]. Thus, for small Reynolds numbers (e.g. $Re < 0.1$), a flow can be assumed laminar. The condition of low Reynolds numbers is assumed throughout this thesis (cf. examples given in Table A.2). Inertia is then unimportant compared to viscous damping, as in most optical manipulation applications.

In the following, theoretical fundamentals of both hydrodynamics and optics will be reviewed with a strong focus on the coupling of mechanical and optical degrees of freedom and finally, its application in optical tweezers.

2.1 Types and magnitudes of forces at small scales

The mechanical world at small scales is substantially different from the macroscopic world. To get an idea of manipulation at small scales, it is important to be aware of the magnitudes of the forces acting on the systems of interest: A bar of chocolate causes a weight force of 1 N whereas the weight force of *E.coli* equals 1 femtonewton (10^{-15} N). *Gravitational forces* of micro- and nanoparticles particles are smaller. A single gold nanoparticle of a diameter of 80 nm causes a weight force of 1 attonewton (10^{-18} N), which can be neglected. In contrast, due to thermally-induced motion or external flow, the same gold particle experiences a *drag force* (or *viscous force*) in the order of a femtonewton (10^{-15} N). *Thermal forces* are caused by collisions of the particle with water molecules, leading to *Brownian motion* of the particle. The net thermal force associated with this random movement is a result of a huge number of random collisions (see Appendix A.1), summing up to a force that is comparable in magnitude to the drag force. Photons colliding with the particle exert a tiny *optical force* corresponding to the momentum of a single photon (e.g. 1.0×10^{-27} N for $\lambda \approx 532$ nm [26]). In laser microscopy, a huge number of photons is focussed so that optical forces can indeed be used as an external manipulation of small particles.

For a motivation of the use of light to manipulate small particles, it is interesting to recognize some similarities and differences of fluidic and optical forces. One of the most interesting results of quantum mechanics is that light can be described as both waves and particles. Here, the latter description is the more intuitive approach to the concept, since then, both optical and fluidic forces can be classified as collisional. For green light, a single photon then possesses a momentum of $4.5 \times 10^{-26}\,\mathrm{kg\,m\,s^{-1}}$. The momentum of a single water molecule at room temperature is substantially higher with $1.8 \times 10^{-23}\,\mathrm{kg\,m\,s^{-1}}$.

In order to move a microscopic or nanoscopic particle, a huge amount of impacts is necessary for both photons and water molecules, that are summing up to a measurable net force. Thermal impacts of water molecules are random and cause a stochastic trajectory of their target. In contrast, incident photons can be guided in a directed fashion and thus push an object in a designated direction. Compared to thermal forces, light provides the advantage that it can be reversibly tuned in strength on a fast timescale and that its energy per quantum can be chosen by the wavelength and not by temperature.

2.2 Fluidic forces on small particles

As a starting point, a small particle of mass m and velocity v immersed in fluid and at room temperature was considered. As Reynolds numbers are low, gravity does not play a significant role and inertia becomes irrelevant. Though, the particle will never be at rest even in the absence of external forces. The reason for the particle trajectory are collisions with molecules stemming from the fluid. This phenomenon was first systematically studied by the botanist R. Brown, in 1827, who observed the movement of small particles contained

in the pollen of *Clarkia pulchella* [27]. It was about eighty years later, that *Brownian motion* was linked to the phenomenon of *diffusion* on a quantitave level by A. Einstein [9], M. Smoluchowski [28], and P. Langevin [29]. Historically, this insight turned out to be an important milestone as the confirmation of the molecular-kinetic theory of heat brought forward by Nobel laureate J.P. Perrin [30] based on Einstein's paper from 1905 [9]. Since more than 100 years, the theoretical description of fluidic forces on small particles has remained a topic of current interest [14, 31, 32].

Brownian motion

Whenever an object is surrounded by a liquid at $T > 0$, the molecules of the liquid will collide with the object (Fig. 2.1). In water, a rough estimate of the collision frequency (cf. Appendix A.1) provides a number as high as 1.5×10^{19} water molecules per second hitting the surface of a 1 µm sized SiO_2 sphere. It will serve as a reference system in the following. The consequence of the collisions is a random walk of the object called *thermal fluctuations* or *Brownian motion*.

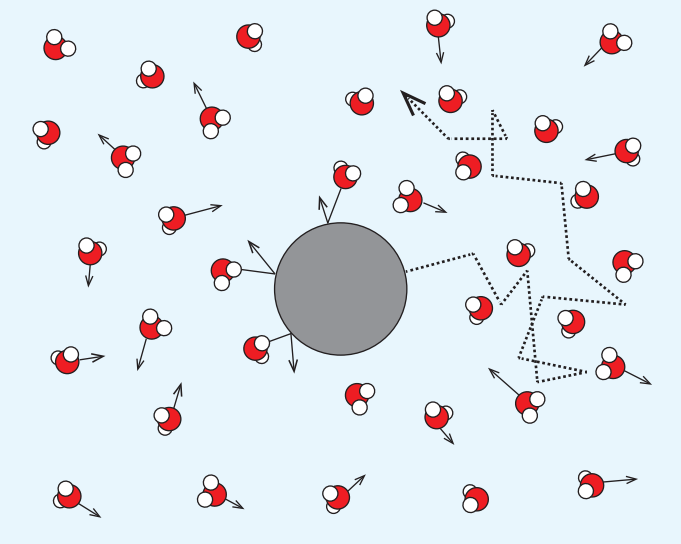

Figure 2.1 – Brownian motion of a fluid-immersed particle. A spherical particle (grey) immersed in water is subject to multiple collisions with water molecules causing a net movement (dashed trajectory). The water molecules' velocities are orders of magnitude higher than the particle's velocity.

Any particle moving through the fluid will experience nonisotropic collisions with molecules leading to frictional resistance. This dissipative force, also known as *drag* or *viscous force*, can be imagined as leaching kinetic energy from the particle and converting it into heat. This leads to a damping of the motion and is thus proportional to the velocity itself:

$$F_{\mathrm{drag}}(t) = -\gamma \cdot v(t) \tag{2.2}$$

Provided laminar flow and a spherical bead, Stokes' law [33] states a simple expression for the proportionality constant γ in Eq. (2.2):

$$\gamma = 6\pi\eta r \tag{2.3}$$

This expression has a strong dependence on external parameters such as temperature, which are given implicitely, e.g. by $\eta(T)$. Since the drag coefficient is associated with a particular surface shape it will vary significantly for a particle geometry other than a sphere [34]. The movement of the particle under the influence of the dissipative force is described by a set of differential equations:

$$\begin{aligned} \dot{x}(t) &= \frac{v(t)}{m} \\ \dot{v}(t) &= F_{\text{drag}} \end{aligned} \tag{2.4}$$

These equations are solved by

$$v(t) = v(0)\, e^{-t/t_{\text{mom}}}$$

with $t_{\text{mom}} = \frac{m}{\gamma}$ being the momentum relaxation time. Typical values (0.1 µs for a 1 µm sized silica bead in water) are much shorter than the used acquisition times. For this reason, no momentaneous velocity can be resolved. Following an exponential decay, on the long term, the drag force alone would necessarily lead to an extinction of any motion. This is however in contradiction with the *equipartion theorem* [35]:

$$\begin{aligned} \frac{m}{2}\langle v^2(t)\rangle &= \frac{3}{2}\cdot k_B T \\ \Rightarrow \quad \langle v(t)\rangle &= \sqrt{\frac{3k_B T}{m}} \end{aligned} \tag{2.5}$$

The last equation states that the mean velocity of a Brownian particle will assume a finite, temperature dependent value. The resolution to this seeming contradiction is the presence of a second, *stochastic* net force acting on the particle. It stems from the individual water molecules that can be seen as particles themselves, constanly pushing the Brownian particle. As detailed in Appendix A.1, water molecules reach speeds of up to $586\,\mathrm{m\,s^{-1}}$ and for a micron sized bead, each second more than 1.5×10^{19} collisions take place that sum up to an appreciable high net force.

In consequence, the particle diffuses through the surrounding liquid with speeds of the order of $\mu\mathrm{m\,s^{-1}}$, which was estimated using Eq. (2.5). It is driven by a multitude of collisions adding up to a stochastic force $\xi(t)$ that must be described by the means of statistical mechanics. Here, the means of variables over an appropriate time interval will be considered instead of the momentaneous values. For the averaged stochastic force it is assumed that

$$\langle \xi(t)\rangle = 0 \tag{2.6}$$

$$\langle \xi(t_1)\cdot \xi(t_2)^*\rangle = 2\gamma k_B T \delta_{t_1 t_2}, \quad \text{where } \delta_{t_1 t_2} = \begin{cases} 1 & \text{for } t_1 = t_2 \\ 0 & \text{for } t_1 \neq t_2 \end{cases} \tag{2.7}$$

This implies several assumptions: (i) $\xi(t)$ is an independent, stochastic variable, (ii) $\xi(t)$ is independent of $v(t)$ and varies rapidly compared to $v(t)$. Then, the *central limit theorem* [36] is applicable, stating that the mean of a sufficiently large number of independent random variables will be approximately Gaussian distributed.

Hot Brownian motion

A special case of Brownian motion occurs in case of particles persistently hotter than the liquid environment [37, 38]. *Hot Brownian Motion* happens, for example, in case of light-irradiated metallic nanoparticles. Due to the limited capacities of water to distribute heat to the entire volume, these particles can be maintained at temperatures that are several orders of magnitude higher than the temperature of the surrounding liquid [39]. Hence, the particle movement can no longer be described by the temperature T_0 of the surrounding liquid. Instead, an effective temperature that lies between the particle temperature and the temperature of the liquid has to be assumed. Falasco *et al.* have provided a simple formula to calculate the effective temperature T_{HBM} of a heated particle trapped in a harmonic potential [40]:

$$T_{\mathrm{HBM}} = T_0 + \frac{5}{12}\Delta T. \tag{2.8}$$

Equation (2.8) is valid for optical trapping of a gold nanoparticle. Since the velocities of Hot Brownian nanoparticles are Maxwell-Boltzmann distributed according to nonuniversal effective temperatures [40], using this temperature allows for an effective equilibrium description of Brownian motion.

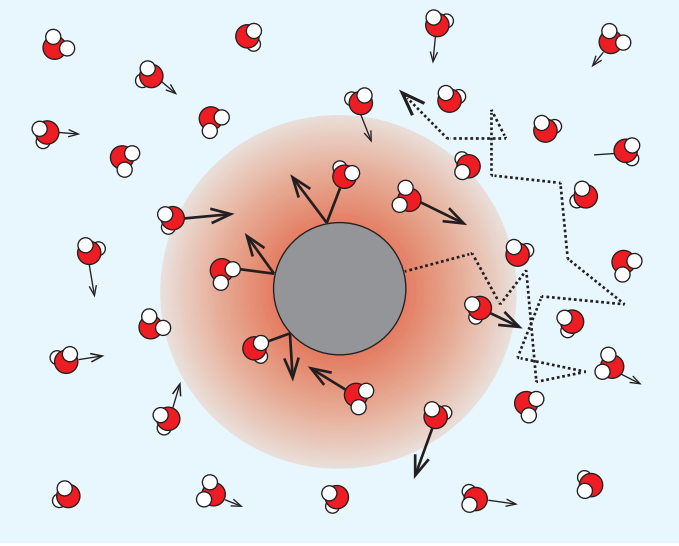

Figure 2.2 – Hot Brownian Motion. If a liquid immersed particle is persistently hotter than its fluid environment, Brownian motion is increased close to its surface. For calculations, the bulk temperature T_0 of the surrounding liquid must then be replaced by an effective temperature T_{HBM}.

Fluctuation dissipation theorem and diffusion equation

The stochastic trajectory of a small particle in water is due to the interplay of a frictional and a random force and represents a very descriptive application of the *fluctuation disspipation theorem* [41]. Being one of the most fundamental results of statistical mechanics, the theorem states a general relationship between the response of a given system to an external disturbance and the internal fluctuation of the system in the absence of the disturbance. It applies both to classical and quantum mechanical systems [41].

Originally, the fluctuation-disspation theorem was formulated for electrical circuits by Nyquist in 1928 [42], but later, in 1951, generalized by Callen and Welton [43]. The *Stokes-Einstein relation* [9, 44] is one of the most comprehensive formulations of the fluctuation dissipation theorems (and probably the earliest):

$$D = \frac{k_B T}{\gamma} \tag{2.9}$$

Here, D is known as *diffusion constant* and relates the variance of the stochastic, thermal force to the damping constant, or drag coefficient, γ. At the same time, a link between microscopic properties and macroscopic observables D and γ is created via the temperature, T. Expanding on this point leads to a probabilistic derivation of the *diffusion equation* for a species of concentration c, first performed by A. Einstein in 1905 [9]:

$$\partial_t c\left(\mathbf{r}, t\right) = D\nabla^2 c\left(\mathbf{r}, t\right) \tag{2.10}$$

This partial differential equation relates the spatial and temporal derivatives of the time-dependent variable c via the diffusion coefficient, and thus describes density fluctuations of a material during a diffusion process. The concept of diffusion is not at all restricted to Brownian motion [45, 46], but can be translated to many other physically relevant systems such as electrical circuits [42, 47], transport in condensed matter physics [48], or even economics [49, 50]. The value of the diffusion coefficient D depends on the dimensionality d of the problem:

$$D = \frac{\langle \partial \mathbf{r}\left(t\right)^2 \rangle}{2 \cdot d \cdot t} \tag{2.11}$$

This linear case however applies to *normal diffusion*, only. Otherwise, *anomalous diffusion* [51] must be considered, described by a more general diffusion coefficient D_α:

$$D_\alpha = \frac{\langle \partial \mathbf{r}\left(t\right)^2 \rangle}{2 \cdot d \cdot t^\alpha} \tag{2.12}$$

For $\alpha = 1$, normal diffusion is retained. Anomalous diffusion predominates, e.g., in the context of subcellular processes and intracellular diffusion [52, 53], where obstacles slow down (*subdiffusion*, $0 < \alpha < 1$) or molecular motors accelerate (*superdiffusion*, $\alpha > 1$) mean particle displacements.

The numerator of Eqs. (2.11) and (2.12) is the mean squared displacement (MSD) for the respective dimension of the problem. It is the most common measure for the spatial extent of diffusion processes involving N particles:

$$MSD\left(\tau\right) = \left\langle \left(x\left(\tau\right) - x_0\right)^2 \right\rangle = \frac{1}{N}\sum_{n=1}^{N}\left(x_n\left(\tau\right) - x_n\left(0\right)\right)^2 \tag{2.13}$$

by following its dependence on the time lag τ usually using a log-log-plot, the kind of diffusion taking place in a certain frequency interval can be derived easily. In case of an optically trapped particle in water, the assumption of normal diffusion is valid making optically trapped particles a convenient tool for vibration sensing. For extending the techniques to intracellular measurements, anomalous diffusion and memory effects of the cytosol must be taken into account in order to derive quantitative physical material parameters and dynamics.

The Langevin equation

The original Langevin equation [54] is the equation of motion describing the apparently random movement of a particle in a fluid due to collisions with the molecules of the fluid. In statistical mechanics, a more general form is also termed Langevin equation, which allows for using it in a broader context. The one-dimensional dynamics of a free Brownian particle, or *Wiener process* [55], can be described by a second order differential equation

$$m\ddot{x}\left(t\right) = -\gamma\dot{x}\left(t\right) + \xi\left(t\right) \tag{2.14}$$

In a next step, the presence of an additional potential, and thus, a force following its negative spatial derivation, can be considered in the equation of motion. The *Einstein-Ornstein-Uhlenbeck theory* [56] of Brownian motion describes the motion of a Brownian particle in a harmonic potential:

$$m\ddot{x}\left(t\right) = -\kappa x\left(t\right) - \gamma\dot{x} + \xi\left(t\right) \tag{2.15}$$

In order to use Brownian particles as force sensors, as I seek to do in this work, another force term is added to the Langevin equation (2.15):

$$\boxed{\begin{aligned}\sum_i F_i\left(t\right) &= F_{\text{drag}}\left(t\right) + F_{\text{harmonic}}\left(t\right) + F_{\text{thermal}}\left(t\right) + F_{\text{ext}}\left(t\right)\\ m\ddot{x}\left(t\right) &= -\kappa x\left(t\right) - \gamma\dot{x} + \xi\left(t\right) + F\left(t\right)\end{aligned}} \tag{2.16}$$

In the low Reynolds number regime, the inertial term can usually be neglected, so that Eq. (2.16) can be rewritten as *overdamped Langevin equation*:

$$\dot{x} = -\frac{\kappa}{\gamma}x\left(t\right) + \xi\left(t\right) \tag{2.17}$$

For most problems considered here, Eq. (2.17) is sufficient as a description. However, for the sake of completeness and illustration, the solution of the driven Langevin equation (2.16) will be presented in the following. An elegant solution of Eq. (2.16), and forming the basis for the results of Section 6.2, can be derived in frequency space. Assuming a very long measurement time t_m, the Fourier transformation is defined as

$$\hat{X}(f) = \int_{-t_\mathrm{m}/2}^{t_\mathrm{m}/2} x(t) \cdot e^{2\pi i f} dt. \tag{2.18}$$

In Fourier space, Eq. (2.16) then reads

$$m\ddot{\hat{X}} = -\kappa\hat{X} - \gamma\dot{\hat{X}} + \hat{\xi}(f) + \hat{F}(f) \tag{2.19}$$

Using that $\dot{\hat{X}}(f) = i2\pi f\hat{X}(f)$, the variable $\hat{X}(f)$ can be isolated. With the definitions of two designated frequencies of the system, that are

$$f_0 = \frac{1}{2\pi}\sqrt{\frac{\kappa}{m}} \qquad \text{(resonance frequency)} \tag{2.20}$$

$$f_c = \frac{\kappa}{2\pi\gamma} \qquad \text{(corner frequency)} \tag{2.21}$$

the expression for the solution of the Langevin equation in frequency space reads

$$\hat{X}(f) = \frac{\hat{\xi}(f) + \hat{F}(f)}{\kappa\left(1 + i\frac{f}{f_c} - \frac{f^2}{f_0^2}\right)} \tag{2.22}$$

Due to the small momentum relaxation time $t_\mathrm{mom} = \frac{m}{\gamma} \approx 0.1\,\mu\mathrm{s}$ (for an 1 µm silica bead in water) compared to the trap relaxation time $t_\mathrm{tr} = \frac{\gamma}{\kappa} \approx 0.1\,\mathrm{ms}$ and thus

$$\frac{f_0}{f_c} = \sqrt{\frac{t_\mathrm{tr}}{t_\mathrm{mom}}} \approx 10^3 \gg 1,$$

using Eqs. (2.20) and (2.21), the last term in the denominator can be neglected. This is equivalent to the neglection of the intertial term ($m\ddot{x}$) in Eq. (2.16) and defines the overdamped Langevin equation in the regime of low Reynolds numbers. Finally, the back-transformation of $\hat{X}(f)$ provides the general solution of Eq. (2.16) in real space:

$$x(t) = \int_{-t_\mathrm{m}/2}^{t_\mathrm{m}/2} \hat{X}(f) \cdot e^{-2\pi i t} df \tag{2.23}$$

For a quantitative evaluation based on the analytic expression, the expressions for the Fourier transforms forces need to be determined (see Section 6.1 and Appendix A.2).

Flow and hydrodynamic coupling

With the introduction of diffusion, a spatial dimension was introduced to the problem of small particle movement (see Eq. (2.10)). For the modeling of velocity fields of the liquid, the particle picture of fluid molecules provided by the Langevin equation, Eq. (2.16), is now left behind and a momentum equation is now applied on a continuum, opening the field

of hydrodynamics [57]. Here, the *Navier-Stokes equations* [58] provide a solid theoretical basis for practical calculations of flow for all kind of applications.

For low Reynolds numbers, the Navier-Stokes equations for an incompressible Newtonian fluid simplify to the *Stokes equations* [59] describing slow viscous flow

$$\begin{aligned} -\nabla p\left(\mathbf{r}\right) + \eta \nabla^2 \mathbf{v}\left(\mathbf{r}\right) &= -\mathbf{F}\delta\left(\mathbf{r}\right) \\ \nabla \cdot \mathbf{v}\left(\mathbf{r}\right) &= 0 \end{aligned} \tag{2.24}$$

and are, as a linearization of the Navier-Stokes equation, accessible to standard solution methods for linear differential equations [34]. In the context of this work, the solution of the flow caused by a point source is of interest, which is the reason for the delta-like force term on the right hand side of the first Eq. (2.24).

The fundamental solution to this set of equations is called *stokeslet*. A derivation of the solution of Eq. (2.24) e.g. via Fourier transform can be found in the textbook of Zapryanov and Tabakova [60]. As a result, the following expressions for velocity and pressure fields are obtained:

$$\mathbf{v}\left(\mathbf{r}\right) = \frac{G\left(\mathbf{r}\right)\mathbf{F}}{8\pi\eta} \tag{2.25}$$

$$p\left(\mathbf{r}\right) = \frac{\mathbf{F}\cdot\mathbf{r}}{4\pi r^3}. \tag{2.26}$$

Here G is called *Oseen tensor*,

$$G\left(\mathbf{r}\right) = \frac{\mathbb{1}}{r} + \frac{\mathbf{r}\cdot\mathbf{r}}{r^3}, \tag{2.27}$$

with $\mathbb{1}$ denoting the identity matrix, and describes the spatial propagation of a point force in a viscous liquid that can be describes by the Stokes equations (2.24). In Chapters 5 and 6, processes related to hydrodynamic coupling between cells will be investigated and discussed. In Section 6.3, Eq. (2.27) will explicitely be needed for the calculation of a point-source force field.

2.3 Interaction of small particles with visible light

In a classical picture, light-matter interactions are a result of an oscillating electromagnetic field resonantly interacting with charged particles. Quantum mechanically, light fields act in order to couple quantum states of the matter. In consequence, light-matter interaction is by far not limited to momentum transfer, but leads to various processes of different quality determined by object size and chemical composition. Further, the irradiation wavelength λ and its ratio to the oject size play a crucial role. Comprehensive reviews on the theoretical foundations of the interaction of light with small particles are available in the literature, see e.g. the books by C.F. Bohren and D.R. Huffman [61], L. Novotny and B. Hecht [62], A. Ashkin [63], the text by H. Rubinsztein-Dunlop *et al.* [64] or relavant PhD theses on this topic [65–69]. In the following, a short general overview of optical processes and forces occurring for visible light incident on small particles will be given.

Overview of optical processes

When light is incident on an object, a part can be reflected while the remainder propagates through the object. Depending on the material and structure of this object, different linear or nonlinear processes may lead to absorption or deflection of photons so that only a part of the incoming light will be transmitted:

$$R + A + T = 1 \tag{2.28}$$

R is the reflectivity and describes the efficiency of interaction between photons and matter. For a perfectly absorbing medium, $R = 0$, whereas for a perfectly reflecting medium, $R = 1$. Together with the absorption A and the transmission T, it amounts up to unity.

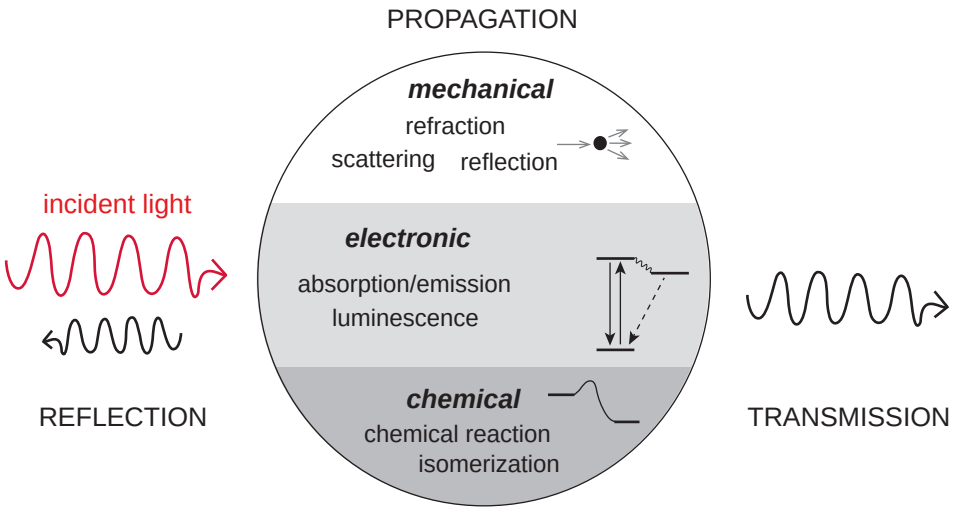

Figure 2.3 – Optical processes. Overview of possible interactions between visible light incident on particles characterized by their size and materials. Qualitatively, the processes are divided in light-induced mechanical, electronic and chemical responses.

Figure 2.3 illustrates different classes of interaction of visible light with matter, roughly divided in mechanical, electronic and chemical processes, associated with different physical and chemical phenomena. All of these are based on photons incident on the surface or propagating through the bulk material of the considered object. Mechanical interactions are characterized by a momentum transfer of the incident photon to the particle interface or its subunits down to the atomic level. *Reflection* and *refraction* are interface effects between media of different refractive index n. These can well be described by the solution of the Maxwell equation for a light ray, known as *Fresnel equations*. More generally, the deflection of light from a straight path is defined as *light scattering*, which does not necessarily follow the laws of reflection. A very general description is provided by *Mie scattering*, describing a full wave solution of the scattering of an electromagnetic wave with a homogeneous sphere. Light scattering has a strong dependence on both particle diameter and incident wavelength.

Optical spectroscopy is often done on the basis of a spectral analysis of scattered light. If a change in wavelength (*Stokes shift*) and thus in detected photon energy can be stated, photons have either been absorbed or emitted and the scattering process was therefore *inelastic*. The process of *photon absorption* is related to a change in the electronic configuration of matter and describes the conversion of incident electromagnetic energy to other forms, including thermal energy. Depending on the electronic energy levels of the material, photon absorption can lead to *luminescence*, which is the re-radiation of photons after photoexcitation.

In a *photochemical* reaction, not only the electronic configuration of atoms or molecules, but also the chemical structure is changed due to incident photons. This includes both photo-induced chemical reactions (e.g. phototoxic reactions) or pure structural changes such as photoisomerization. Photochemical paths access high energy intermediates that cannot be generated thermally.

It is important to note that the optical processes listed in Fig. 2.3 are usually not restrictive. An example are Raman or Brillouin scattering, where a photon is scattered at optical or acoustic phonons, respectively, resulting in a detectable Stokes shift of the emitted photons. In this work, a strong focus lies on optomechanical manipulation and optical forces in connection to photochemical processes (Chapter 4) and mechanical (Chapter 5 and 6) processes. These are derived as solutions of Maxwell's equations using formalisms of varying complexity. At the end of the present section, a review on the photochemistry of azobenzene is provided, which will later be used as a photochemical switch on fast time scales.

Optical forces

In the framework of classical electrodynamics, the basis of optical forces lies in the conservation of linear momentum, which is a direct consequence of *Maxwell's equations* [62]. Using some vector analysis and the *Lorentz force law*,

$$\mathbf{F}\left(\mathbf{r},t\right) = q[\mathbf{E}\left(\mathbf{r},t\right) + \mathbf{v}\left(\mathbf{r},t\right) \times \mathbf{B}\left(\mathbf{r},t\right)], \tag{2.29}$$

where q is a charge, an elegant relationship between the world of electromagnetism and the world of mechanics can be expressed via *Maxwell's Stress Tensor*

$$\mathbb{T} = \epsilon_0 \epsilon E_i E_j - \mu_0 \mu H_i H_j - \frac{1}{2}\left(E^2 + H^2\right)\mathbb{1}. \tag{2.30}$$

It is valid for surrounding media that can be described sufficiently well by a dielectric constant ϵ and a magnetic susceptibility μ.

$$\boxed{\begin{aligned}\int_{\partial V} \mathbb{T}\cdot\hat{\mathrm{n}}\; dA &= \frac{d}{dt}[G_{\text{field}} + G_{\text{mech}}] \\ &= \frac{d}{dt}\frac{1}{c^2}\int [\mathbf{E}\times\mathbf{H}]\; dV + \mathbf{F}\end{aligned}} \tag{2.31}$$

Here, G_{field} and G_{mech} denote field momentum and mechanical momentum. In order to express the average optical force on an arbitrarily shaped object, $\langle \mathbf{F} \rangle$, it is noted that the time average over one full period is zero for the field momentum and thus

$$\boxed{\langle \mathbf{F} \rangle = \int_{\partial V} \langle \mathbb{T}(\mathbf{r}, t) \rangle \cdot \mathbf{n}(\mathbf{r}) \, dA} \tag{2.32}$$

This force is thus entirely determined by the electric and magnetic fields incident on an aribitrary surface enclosing the object of interest. One important restriction here is that the body is rigid since otherwise, magneto- and electrostricitive force would have to be considered. Importantly, then neither material nor size of the body play a role so that Eq. (2.32) remains valid for arbitrary objects. In the following, two different cases are presented where forces are derived first using Maxwell's stress tensor and second, a less formal approach.

Radiation pressure

In the simplest case, optical forces arise due to the interaction of an electromagnetic wave with a large object. As a starting point, an infinitely extended surface irradiated by monochromatic light propagating in z-direction is considered:

$$\mathbf{E}(\mathbf{r}, t) = E_0 \cdot \mathrm{Re}\left[\left(e^{ikz} + re^{-ikz}\right) e^{-i\omega t}\right] \hat{n}_x$$

$$\mathbf{H}(\mathbf{r}, t) = \sqrt{\frac{\epsilon_0}{\mu_0}} E_0 \cdot \mathrm{Re}\left[\left(e^{ikz} - re^{-ikz}\right) e^{-i\omega t}\right] \hat{n}_y$$

Since for these fields, the first two terms in Eq. (2.30) give no contribution to the stress tensor $\mathbb{T}$, Eq. (2.32) yields for the force on the considered object

$$\langle \mathbf{F}_{\text{rp}} \rangle = \int_A \langle \mathbb{T}(\mathbf{r}, t) \rangle \cdot \hat{n}_z \, dA = \frac{\epsilon_0}{2} E_0^2 (1 + R) \cdot A \cdot \hat{n}_z, \tag{2.33}$$

where R is the reflectivity from Eq 2.28 and A the irradiated surface. With the intensity

$$I_0 = \frac{\epsilon_0 c}{2} E_0^2$$

of a plane wave, the radiation pressure p_{rp} is defined as

$$\boxed{p_{\text{rp}} = \frac{\langle |\mathbf{F}_{\text{rp}}| \rangle}{A} = Q \frac{I_0}{c} \cdot (1 + R).} \tag{2.34}$$

Q is a quality factor describing the efficiency with which photon momentum is transferred to the object and is determined entirely by the geometry of the scattering. As illustrated in Fig. 2.4, for $Q = 0$, all light is transmitted through the object, while for $Q = 2$, all light is reflected back and $Q = 1$ represents a perfectly absorbing surface. On all length scales, radiation pressure can be used to accelerate or trap particles and objects in a medium [70].

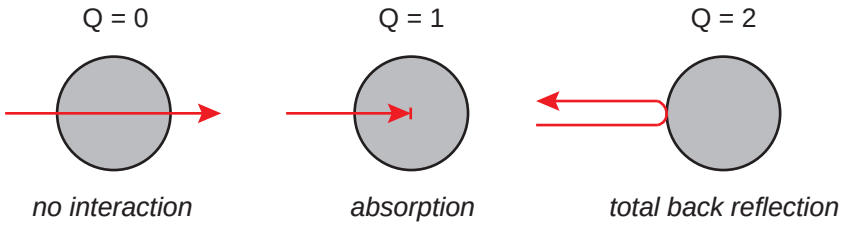

Figure 2.4 – The quality factor Q. Three limiting cases of light-particle interaction.

Dipole approximation

The second limiting case are particles whose diameter is much smaller than the wavelength of the incident light (*Raleigh particles*). In this approximation, the particles are uniquely characterized by their dipole moment and each dipole can be seen as two oppositely charged particles at locations $\mathbf{r}_1$,$\mathbf{r}_2$ connected by a certain binding energy. Using center-of-mass coordinates and the dipole moment $\mathbf{p} = q\,(\mathbf{r}_1 - \mathbf{r}_2)$, the Lorentz force equation, Eq. (2.29), can be expressed as follows:

$$\mathbf{F} = (\mathbf{p}\cdot\nabla)\,\mathbf{E} + \dot{\mathbf{p}}\times\mathbf{B} + \dot{\mathbf{r}}\times(\mathbf{p}\cdot\nabla)\,\mathbf{B} \tag{2.35}$$

In the time average, the last term vanishes and the average force thus results in

$$\langle\mathbf{F}\rangle = \sum_i \langle p_i\,(t)\,\nabla E_i\,(t)\rangle. \tag{2.36}$$

In case of a monochromatic incident wave,

$$\mathbf{E}\,(\mathbf{r},t) = \mathrm{Re}\left[\mathbf{E}\,(\mathbf{r})\,e^{-i\omega t}\right] \quad \text{and}$$

$$\mathbf{B}\,(\mathbf{r},t) = \mathrm{Re}\left[\mathbf{B}\,(\mathbf{r})\,e^{-i\omega t}\right],$$

so that

$$\boxed{\begin{aligned}\langle\mathbf{F}\rangle &= \frac{\alpha'}{2}\sum_i \mathrm{Re}\,[E_i^*\nabla E_i] \;+\; \frac{\alpha''}{2}\sum_i \mathrm{Im}\,[E_i^*\nabla E_i] \\ &= \langle\mathbf{F}_{\mathrm{grad}}\rangle \;+\; \langle\mathbf{F}_{\mathrm{scatt}}\rangle\end{aligned}} \tag{2.37}$$

with α' and α'' being the real and the imaginary part of the complex polarizability α, which only depends on the material. The denotation of the first part as gradient force origins from the fact it could also be written

$$\langle\mathbf{F}_{\mathrm{grad}}\rangle = \frac{\alpha'}{4}\nabla\,(\mathbf{E}^*\cdot\mathbf{E}) \tag{2.38}$$

Since any gradient force is rotation-free ($\nabla\times\langle\vec{F}_{\mathrm{grad}}\rangle = 0$), this force field is conservative.

$$\langle\mathbf{F}_{\mathrm{scatt}}\rangle = \frac{\sigma_{\mathrm{scatt}}}{c}\langle\mathbf{S}\rangle + c\sigma_{\mathrm{scatt}}\,[\nabla\times\langle\mathbf{L}\rangle] \tag{2.39}$$

Here, σ_{scatt} denotes the scattering cross-section, $\mathbf{S}$ stands for the Poynting vector, c is the speed of light and $\mathbf{L}$ the angular momentum. The large electric dipole polarizability

associated with plasmon excitation results in optical forces and torques that are enhanced to such extent that gold nanoparticles as small as 10 nm can be trapped [71]. The plasmon excitation also leads to strongly enhanced electromagnetic fields within the metal nanoparticle leading to photothermal heating that can be orders of magnitude stronger than for dielectric particles of similar size [39].

Generalized Lorenz-Mie theory (GLMT)

The two limiting cases for either particles much larger or much smaller than the incident wavelength demonstrate that approximations are helpful for a description of electromagnetic forces on particles. At the mesoscale, however, the wavelength is comparable to the particle diameter requiring full wave solutions for the light-matter interaction problem.

A description of the scattering of a linearly polarized plane wave by any object of arbitrary size, shape and refractive index is provided by *Lorenz-Mie theory* [72]. It is based on a solution of the Maxwell's equations and expresses the scattered field in terms of an infinite series of spherical multipole partial waves. Later, the approach was extended to incident waves of arbitrary beam shape coefficients so that GLMT could then be applied to focused Gaussian beams [73].

Photochemistry of azobenzene

So far, it was discussed that mechanical manipulation of matter can be achieved with optical forces. In Chapter 4, a photochemical approach is shown to reversibly manipulate vesicle mechanics. In the following the basic concept of the light-sensitive response of a photoswitchable molecules at the example of azobenzene will be introduced.

Since the discovery of *cis*-azobenzene by Hartley in 1937 [74], the photochemistry of *azo*-components such as azobenzene has been investigated in great detail using optical spectroscopy techniques [75]. Due to the geometry of the *azo*-group, azobenzene can exist in either *trans*- or *cis*-state (Fig. 2.5A). The *trans*-conformation of azobenzene is $10 - 12$ kcal/mol more stable than the *cis*-isomer [76], so that, in the dark at equilibrium, it is the dominant isomer ($> 99.99\%$) [75, 77]. A substantial amount of the *cis*-isomer can be produced by irradiation with UV-A (320 - 350 nm) light. A regeneration of the *trans*-isomer can be achieved either by dark-adapting the solution on a timescale of days at room temperature [78] or by irradiation with visible light in the blue wavelength region (400 nm - 450 nm).

A feature of all azo-components is the low-energetic (n, π^*) molecular electronic transition (Fig. 2.5B). It manifests as a weak absorption band at visible wavelengths near 440 nm in UV/vis-spectra of azobenzene [82]. The spectra of *trans*- and *cis*-azobenzenes are distinct but overlapping. Due to steric reasons in the molecule geometry [83], the (n, π^*) - transition is more pronounced for *cis*-azobenzene compared to *trans*-azobenzene. A distinct and stronger band near 320 nm for *trans*- and 280 nm for *cis*-azobenzene represents the allowed (π, π^*) - transition. Associated with even higher excitation energies, a third

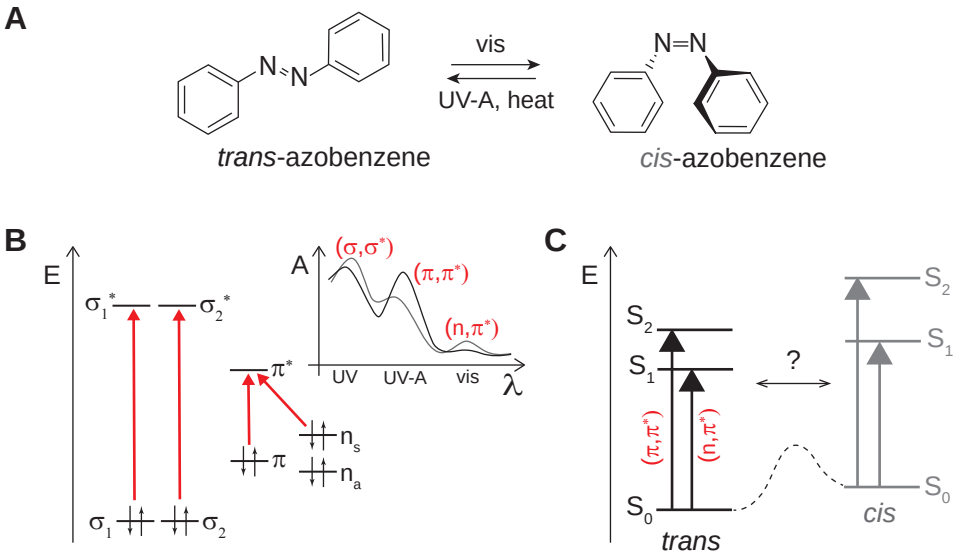

Figure 2.5 – Characteristics of the azobenzene group. (A) Chemical structure and *trans-cis*-isomery of azobenzene. (B) Rough energy levels of azobenzene in molecular orbital theory, see e.g. Ref. [79], and associated bands in typical UV/vis-spectra of both isomers, see e.g. Ref. [80]. (C) Energy scheme of ground state and excited levels of *trans*- and *cis*-azobenzene after Ref. [81]. The isomerization mechanism is not yet fully understood.

band appears at wavelengths around 230 - 240 nm, respresenting electronic excitations of the σ-electrons of the azo-group, unlikely to be involved in photochemical reactions of azobenzene [79]. The mechanism of the *trans-cis*-isomerization and the reverse process are still not very well established (see Fig. 2.5C and Refs. [84, 85]), even though the isomerization process has been assessed with single molecule precision [86, 87] by ultrafast time-resolved spectroscopic techniques [81, 88–90] and dynamic simulations [91, 92]. The sum of the quantum yields is different to unity, which indicates multiple pathways for isomerization [93]. In literature, at least four different mechanisms have been proposed (a summary is given in Ref. [84]), based on either the reversal of one of the N − C bonds involving the (n, π^*) - transition or by the rotation of the N = N double bond involving the (π, π^*) - transition, or combinations of both.

Interestingly, a modification of the aromatic rests at the azobenzene seems to have, except an eventual redshift in wavelength, only minor impact on the spectral properties of the azogroup [94]. Most optical properties remain preserved so that the results on azobenzene can be used as a basis to understand any azobenzene-containing species.

2.4 Theory of optical tweezers

In the low Reynolds number regime, optical forces can easily dominate thermal forces. In the 1970s, A. Ashkin and coworkers discovered that a gradient force can hold a single particle by means of radiation pressure [7, 70], which opened up the field of *Optical Tweezers*. Comprehensive reviews on optical trapping can be found in Refs. [95–100].

Principle of optical tweezers

Optical tweezing is the ability of a tighly focused laser beam to confine a small particle in the focus due to optical forces (Fig. 2.6A). There are two qualitative explanations for the working principle of optical tweezers, that are both based on the existence of a *gradient force* (see Section 2.3). The first explanation is that the electric field induces a dipole moment in the trapped particle, which is then attracted to the region of highest electrical field density (Fig. 2.6B). The second is based on momentum transfer of a converging or diverging beam. A typical particle with a refractive index that is higher than the one of the surrounding liquid can be considered as a weak positive lens. If the beam is converging, it will thus converge even further and be pushed towards the focus (see sketch in Fig. 2.6C). If the beam diverges, this divergence will as well be increased even more and the particle is pulled towards the focal spot. In both cases and for both explanations, a small particle reaches the position of minimal energy at the point of highest laser intensity.

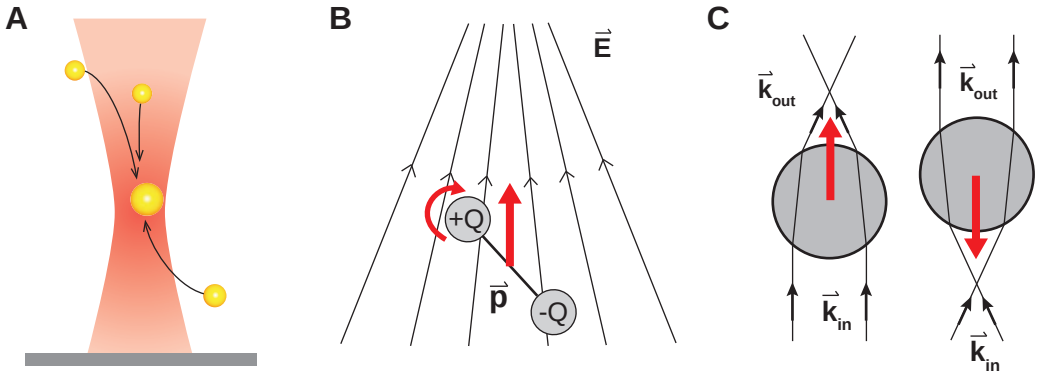

Figure 2.6 – Principle of optical tweezers based on the existence of a gradient force. (A) Sketch of an optical tweezer. (B) An electric field induces a dipole moment **p** in a polarizable particle, which is then attracted to the region of highest field strength. (C) Motivation of a gradient force by momentum change in ray optics.

Optical trapping is applicable in a very wide size regime and also for different shapes and materials [6]. Several examples for this are shown in Fig. 2.7, which divides the applications of optical trapping into *atom trapping*, *nanotweezers* and *optical tweezers*. For particles smaller than the wavelength of the light ($L \ll \lambda$), Rayleigh theory can be used to simplify the description, while simple geometrical optics suits for particles much

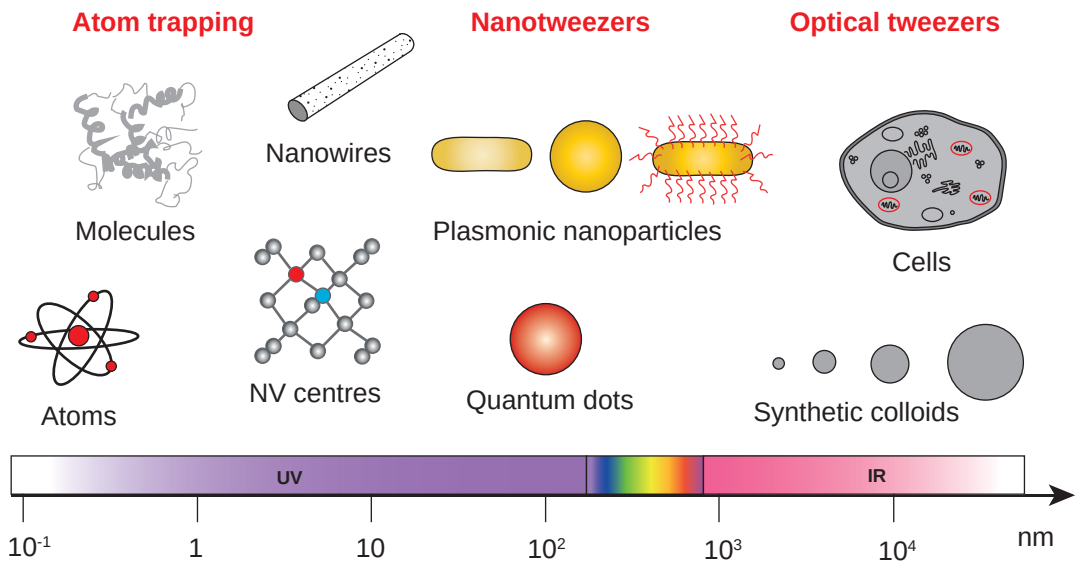

Figure 2.7 – The three size ranges of optical trapping. Objects of different sizes can be trapped within three main regimes: atom trapping (Å to nm), nanotweezers (nm to 100 nm) and optical tweezers (> 0.1µm). The horizontal scale bar shows the average object size and the corresponding light wavelength. After Ref. [6], Fig. 1.

larger than the wavelength ($L \gg \lambda$). The following paragraph introduces a practical way of calculating optical forces and an appropriate computation method.

Optical tweezers offer an ideal platform to study Brownian dynamics as the focused laser field introduces deterministic optical forces and torques [8, 101, 102]. Applications of optically trapped particles to probe environmental properties range from viscosity measurements [103, 104] to local temperature determination [105] to the control of biomolecules [4, 106]. For precise measurements, an accurate calibration is crucial. Please note that throughout this thesis, a one-dimensional description in the plane perpendicular to the trapping beam direction is used. Even though the existence of forces in three spatial direction affects the dynamics of particle trapping, in the simple picture of a harmonic trap as used here, an independent description is already sufficient [98]. The most important parameter characterizing an optical tweezer is then the *trap stiffness*, κ, or, more precisely, the *radial spring constant*, which will be treated equivalently throughout. The restoring force of an optical trap is thereby assumed as a Hookean spring,

$$F_{\mathrm{trap}}(t) = \kappa \cdot x(t)\,. \tag{2.40}$$

The rate of increase of the force F_{trap} is described by a change in position x. Together with the laser power, which is related to the *trap strength*, trapping of a spherical particle can be explained.

There are several passive and active characterization methods for a determination of the trap stiffness κ [96, 107], such as the *power spectral density method* [108, 109], the *equipartition method*, *velocity auto correlation* [110], the *drag force method* [107] or

the *mean squared displacement method* [111] to name a few. Those are either exclusively relying on thermal motion of the trapped particle or utilize an external manipulation [112]. In this work, mainly the equipartition theorem is chosen for the determination of κ as it is the most intuitive method.

The position distribution $W(x)$ of the particle derived from the overdamped Langevin equation, Eq. (2.17), including the harmonic potential $U(x)$, turns out to be a Gaussian distribution [113]:

$$W(x) = A \cdot \exp\left(-\frac{U(x)}{k_B T}\right) = A \cdot \exp\left(-\frac{\kappa x^2}{2 k_B T}\right) \tag{2.41}$$

In this expression, A defines the trap strength. Application of the definition of the standard deviation σ of a Gaussian distribution[1] provides the conversion

$$\kappa = \frac{k_B T}{\sigma^2}. \tag{2.42}$$

For a known temperature, the trap stiffness can then be derived by analysis of a video-recorded particle trace.

Calculation of optical forces

Probably the largest difficulty in the theoretical treatment of optical trapping is the fact that for most trapping applications, the size of the particle is comparable to the laser wavelength (cf. Fig. 2.7). The determination of local force fields for arbitrary objects is thus a highly nontrivial task. Both gradient and scattering forces result from the fact that the particle changes the direction of the beam. Hence, a description of optical trapping as a scattering problem provides a good starting point for theoretical modeling.

In the easiest case, optically trapped objects are homogeneous and isotropic spheres and the incoming light is monochromatic. The interaction of such objects with light still has an analytic solution applying electromagnetic theory. However, Generalized Lorenz-Mie theory must be applied (please see Section 2.3 for a short introduction). The difference to Lorenz-Mie theory and the major difficulty is the integration of the shape of the tightly focused laser beam into the solution of the scattering problem [114]. Though possible, still immense computational effort is required to obtain analytic solutions even in the simplest cases. Moreover, the mathematical complexity of Generalized Lorenz-Mie theory reasonably prevents most experimentators from solving the equations by hand. For this reason, theoreticians worked hand in hand with experimentators to develop convenient toolboxes for the computation of optical forces for practical applications. One of these is the toolbox by Nieminen *et al.* [115], which has been designed for deriving forces and torques both on spherical and nonspherical particles and for different beam shapes. The code relies on the *T-matrix method* [116, 117] which is closely allied to Lorenz-Mie theory.

[1] It is important to note the difference between the standard deviation σ and the line width at half macimum σ_{FWHM} of a Gaussian distribution. Both are related by the formula $\sigma_{\mathrm{FWHM}} = 2\sqrt{2\ln 2} \cdot \sigma = 2.3548\sigma$.

The T-matrix method is based on a description of calculating optical forces and torques as a pure scattering problem [98]. The method by Nieminen *et al.* uses a least squares fit to produce a Helmholtz beam with a far field that matches the one expected from the incident focused beam [115]. Mathematically, the foundation of the T-matrix method is given by

$$\mathbf{P} = \mathrm{T}\mathbf{A} \qquad \text{or} \qquad p_k = \sum_n^{\infty} T_{kn} a_n, \tag{2.43}$$

where T is a diagonal matrix for spherical scatterer. T relies only on the properties of the particle and the incident wavelength. This means that for a known particle, or a known T-matrix, the effort of computing different positions within the trap reduces significantly making the method fast. The elements p_k and a_n are determined, together with a set of vector spherical wavefunctions Ψ_n as a basis, by

$$U_{\mathrm{inc}} = \sum_n^{\infty} a_n \Psi_n^{(\mathrm{inc})} \tag{2.44}$$

and

$$U_{\mathrm{scatt}} = \sum_k^{\infty} p_k \Psi_k^{(\mathrm{scatt})} \tag{2.45}$$

Both Eqs. (2.44) and (2.45) solve the Helmholtz equation and describe incoming and scattered electromagnetic fields. Finally, the forces associated with incoming and outgoing fluxes of electromagnetic momentum can be calculated by integrating Maxwell's stress tensor $\mathbb{T}$ from Eq. (2.30), which reduces to an analytical problem for spherical particles.

Nieminen's toolbox was used to derive optical force fields for 1 µm (diameter) SiO_2 spheres and 80 nm gold particles and for different laser wavelengths (532 nm and 1064 nm) that were used in this thesis (see Section 3.1). The resulting force fields are plotted in Fig. 2.8. It is shown that for a metal sphere, in contrast to the dielectric sphere, both attractive and repulsive potential landscapes are possible. In the latter case, the laser wavelength is matching the particle plasmon resonance. Strong forces of tens of pN push the particle away from the focus. This property has found applications in optical printing and single particle lithography techniques [118, 119]. For a laser power that is off-resonant, attractive forces dominate repulsive forces on the considered particles (Fig. 2.8B–D). In this case, optical trapping is achieved. Comparing Fig. 2.8B with Fig. 2.8D, the optical gradient forces are two orders of magnitude higher for silica spheres compared to gold nanoparticles. This explains why optical trapping of plasmonic nanoparticles, that was first performed by K. Svoboda and S. Block in the 90s [120], is far less established compared to trapping of dielectric microspheres [99, 121].

It should be noted that the calculation of the optical force field does not describe the full problem of optically tweezing of a small particle. Fluidic and thermal forces, also including convection and diffusion phenomena, complicate the situation. It is therefore easier to derive characteristica of an optical trap from a measurement of the real particle displacement and fit a model to it rather than solving the full problem by means of theory.

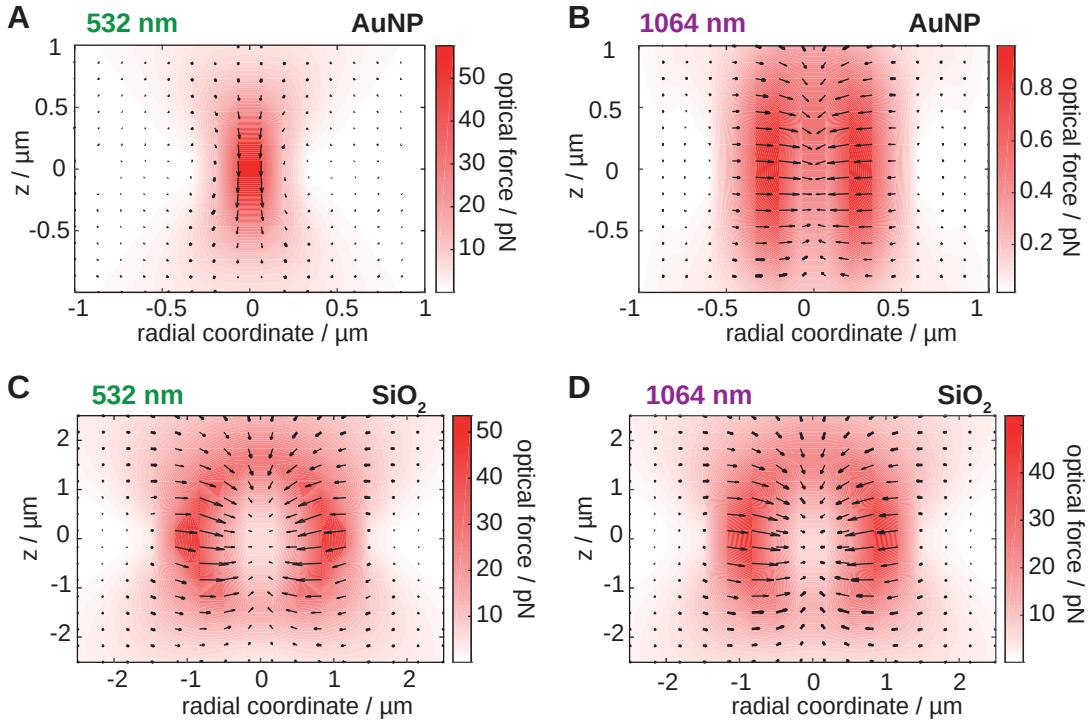

Figure 2.8 – Calculated optical forces. Calculated force fields in water for an 80 nm (diameter) gold nanoparticle (A,B) and a 1 µm fused silica sphere (C,D). Results are given for a focused Gaussian laser beam in negative z-direction with a wavelength of 532 nm (A,C) and 1064 nm (B,D). As a laser power, we deliberatley chose 50 mW. The numerical aperture of the objective was 1.0. For the silica sphere, a constant refractive index of fused silica, 1.458 [122], was assumed. For the gold nanoparticle, the dielectric function measured by Johnson and Christy [123] was employed.

Power spectral density analysis of particle dynamics

For the analysis of stochastic trajectories, it is advantageous to switch to Fourier space. Here, a brief motivation for this approach is given. An excellent rewiew on useful techniques and correction methods was written by Berg-Sørensen *et al.* [109]. In frequency domain, the *Power Spectral Density* (PSD) represents a normalized physical quantity that can be used to compare and analyze the tracked movement of a diffusing particle. The PSD is defined as

$$S\left(f\right) = \frac{\hat{x}\left(f\right) \cdot \hat{x}\left(f\right)^*}{t_\mathrm{m}}, \tag{2.46}$$

including the total measurement time t_m. Using the general solution of the Langevin equation in Fourier space, Eq. (2.22), the PSD reads for particles following the dynamics of the Langevin equation, Eq. (2.16):

$$S_x\left(f\right) = \frac{1}{t_\mathrm{m}\left(2\pi\gamma\right)^2} \frac{\hat{\xi}\left(f\right)^2 + \hat{F}\left(f\right)^2 + 2\hat{\xi}\left(f\right) \cdot \hat{F}_S\left(f\right)}{f^2 + f_c^2} \tag{2.47}$$

In order to deal with the stochastic variable, the expectation value of Eq. (2.47) can be considered. This requires to calculate the expectation values of all involved variables. Assuming $\xi(t)$ as an independent stochastic force this implies that

$$\left\langle \hat{\xi}(t) \right\rangle = 0 \qquad \text{and} \tag{2.48}$$

$$\left\langle \hat{\xi}(f_1) \cdot \hat{\xi}(f_2)^* \right\rangle = 2\gamma k_B T t_m \delta_{f_1 f_2} \tag{2.49}$$

Consequently, Eq.(2.47) can be rewritten

$$\langle S_x(f) \rangle = \frac{k_B T}{2\pi^2 \gamma \cdot (f^2 + f_c^2)} + \frac{\left\langle \hat{F}(f)^2 \right\rangle}{t_\mathrm{m} (2\pi\gamma)^2 \cdot (f^2 + f_c^2)} \tag{2.50}$$

Here, the first part of the equation denotes the undriven Langevin equation ($F = 0$) of the damped movement of a Brownian particle. For $F = 0$ and a vanishing corner frequency $f_c = 0$, the $1/f^2$ - behaviour of normal diffusion is recovered. At low frequencies ($f \ll f_c$) and without the scattering force the power spectrum is independent on frequency:

$$S_0 = \frac{2\pi\gamma k_B T}{\kappa^2} \tag{2.51}$$

Though, the plateau does depend on the force constant. It is thus possible to measure the trap stiffness even though the time resolution of the detection is below the corner frequency.

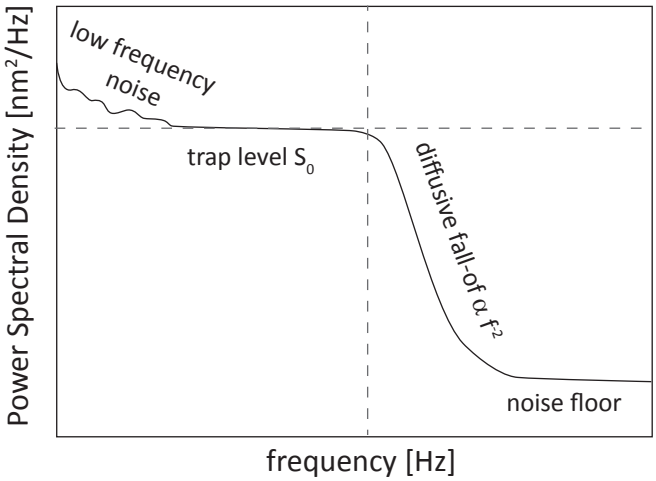

Figure 2.9 – Characteristic PSD plot. Sketch of an idealized power spectrum of an optically trapped particle. The axes are given in typical units.

A schematic of a typical PSD of an optically trapped particle is shown in Figure 2.9. It also follows the derived characteristics, see Eq. (2.50). Measured examples and an application of the equations derived above can be found in Section 6.2. Experimentally, the detection system often limits the data acquisition by noise in the low frequency regime and a noise floor in the high frequency regime [109, 113]. In between, a constant plateau represents the confinemnt of the particle in the optical trap. At the corner frequency, the PSD transforms to a diffusive fall-off.

Chapter 3

Experimentals: From Particle Trapping to Cell Tracking

3.1 Laser microscopy and optical spectroscopy

Optical trapping has become an increasingly important technique to control and probe the structure of matter covering all length scales from nanometers to millimeters [8]. In this section, technical details of the laser microscopy setups are given, while application-specific changes are introduced in the respective results sections. Sketches of the optical beamlines of the specific optical setups used are shown in Fig. 3.4.

Lasers and light sources

For optical trapping experiments, a near-infrared (NIR) laser is appropriate for a wide range of materials. As illustrated in Fig. 3.1A, this wavelength regime lies in the second biological window [124]. Here, scattering and absorption of biological tissue, cells and vesicles are lowest and thus offer a maximal penetration depth at minimal photodamage. For the dielectric and the metal nanoparticles used, no resonances are expected in the NIR region (Fig. 3.1B). In consequence, for sufficient laser power and focusing of the free NIR laser beam, gradient forces dominate the scattering forces (see Section 2.4). A 1064 nm diode pumped continuous wave (CW) laser (*Cobolt AB*, Cobolt Rumba^{TM}, 05-01 Series, 3W) was chosen for most trapping experiments and for the realization of holographic optical tweezers. In case of dielectric microparticles, a 532 nm CW laser trap (*Coherent*, Verdi 10) is applicable, as well. In contrast, for 80 nm gold nanoparticles, an incident wavelength of 532 nm is resonant with the particle plasmon, leading to plasmonic heating and strong scattering forces (see Fig. 3.1B).

Power modulation of the lasers was realized in different ways and depending on the application. In the simplest case, laser intensity was decreased by inserting a gray filter into the beam. A periodic modulation of the laser intensity can be achieved by rotating a glass cover slide that was half sputtered with a layer of gold palladium (AuPd) in the beam

path at frequencies of up to 60 Hz (for the experiments in Section 6.3). Alternatively, a spatial light modulator (SLM) was used to control the laser intensity. For the creation of a step-like intsity profile (see Chapter 6), a chopper wheel (*Newport*, New Focus Optical Chopper 3501) was employed.

Illumination with UV-A and blue light (see Chapter 4) was performed using fiber coupled light-emitting diodes (LEDs, *Prismatix*, $\lambda = 365\,\text{nm}$ and $\lambda = 465\,\text{nm}$) with a maximum total output power of 70 mW measured at the end of the fiber. Typical power densities varied between $0.1\,\text{kW cm}^{-2}$ and $5\,\text{kW cm}^{-2}$. For light microscopy, a 100 W halogen lamp coupled to the sample holder from below using an adjustable mirror served as a source of illumination.

Microscopes and spectrometers

Microscopy was performed with conventional upright microscopes (*ZEISS GmbH*, Axiotech 100 or Axiovert). Figure 3.2 shows a sketch of the setup and pictures of typical experimental configurations. The microscope was customized for laser microscopy applications by removing the original illumination path through the objective and guiding the illumination from below the sample using mirrors. For imaging, water immersion objectives (*ZEISS GmbH*) of different magnifications were applied. The use of a dark field oil condensor (*ZEISS* Ultra condenser, NA = 1.2/1.4) and white light illumination enabled detection of vesicle membranes and gold nanoparticles because of their large scattering cross-section in the visible wavelength regime (Fig. 3.1B) [125]. The position of the sample relative to the objective could be adjusted with a piezoelectric step motor (*LINOS*, PiezoController CU30) connected to a magnetic sample holder. The motor was controlled with a gamepad accessed by a custom-made *Labview* program.

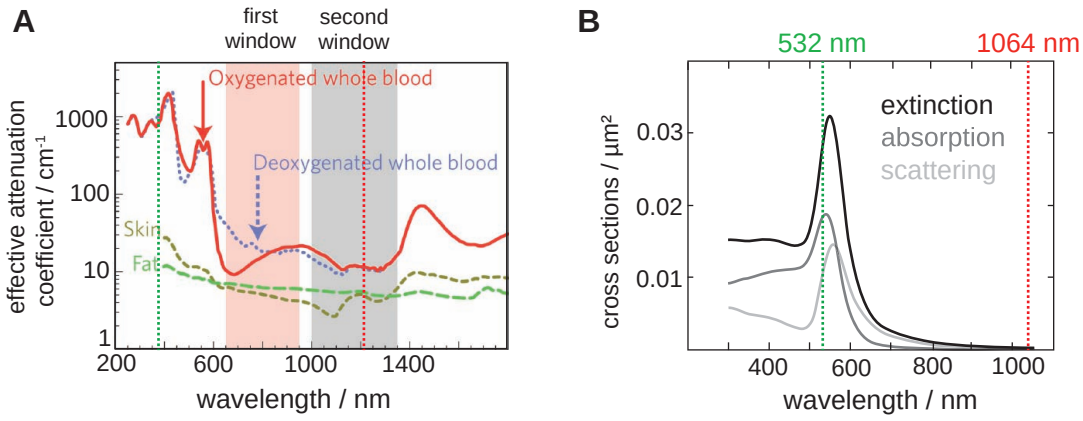

Figure 3.1 – Wavelength ranges relevant for laser microscopy. (A) Attenuation of irradiation for biological tissue and blood, taken from Ref. [124]. (B) Spectral properties of an 80 nm gold particle in water at room temperature calculated with Mie theory (software: *MQMie*). The two used laser wavelengths, 532 nm and 1064 nm, are indicated in both plots.

Video detection of the sample was performed by using either a digital camera (*Canon*, Canon EOS 6D) or a scientific high speed camera (*PCO AG*, pco.dimax HD). Alternatively, a grating spectrometer (*Princeton Instruments*, Acton Spectra Pro 300i) connected to a liquid nitrogen cooled CCD (*Princeton Instruments*, MicroMax) allowed to perform single particle scattering spectroscopy in dark-field mode.

For optical spectroscopy of bulk samples, the liquids were kept in quartz cuvettes. UV/vis spectra were recorded with a Cary 60 UV/vis spectrometer (*Agilent Technologies*). The dynamic light scattering (DLS) data was obtained by using a Zetasizer Nano Series "L" instrument (*Malvern*).

Optical tweezer setups

In the simplest case, an optical tweezer is generated by focusing a laser beam through a high numerical aperture (NA) objective lens (Fig. 3.2A). The setup is centered around the modified ZEISS Axiovert microscope. Removing the original illumination path allowed the insertion of a beamsplitter cube in the imaging path of the microscope. The cube can be mounted in two different configurations so that laser beams could be coupled into the objective either from the side or from the back of the microscope. A notch filter for both laser wavelengths (532 nm and 1064 nm) was positioned in the imaging path to avoid artifacts and damage caused by laser reflections.

For some experiments, two laser beams were necessary. For this purpose, the outcoming laser beam was split into two beams by cube-mounted beam splitter plates. The separation distance between the two optical beams could be adjusted on the micron-scale by two mirrors. If necessary, additional illumination of the sample was achieved by guiding light from a fiber on the sample perpendicularly to the trapping beam (see Fig. 3.2A for a scheme and Fig. 3.2B,C for two different experimental configurations). A beam expander (*Edmund Optics*/ *Thorlabs*, 1X–10X) was mounted in the laser beampath for two reasons:

- A better trap quality is achieved if the back aperture of the focusing objective is filled or overfilled.
- A slight defocusing of the trapped object due to scattering forces or the influence of gravity can be balanced by moving the trap focus with respect to the imaging plane with relay optics, such as a beam expander.

Similarly, a defocusing caused by chromatic aberration of the objective can be balanced. Alternatively, a 1000 mm lens was inserted to prefocus the NIR laser beam.

Optical tweezers can be combined with dark-field microscopy [126]. Here, unscattered (i.e. directly transmitted) light is excluded from the imaging process. In this way, the localization of diffraction-limited spots is achieved if trapped objects are either strong scatterers or possess luminescent properties. Dark-field microscopy, however, requires the numerical aperture (NA) of the condenser exceeding the NA of the light-collecting objetive,

$$\mathrm{NA\,(condenser)} > \mathrm{NA\,(objective)}\,. \tag{3.1}$$

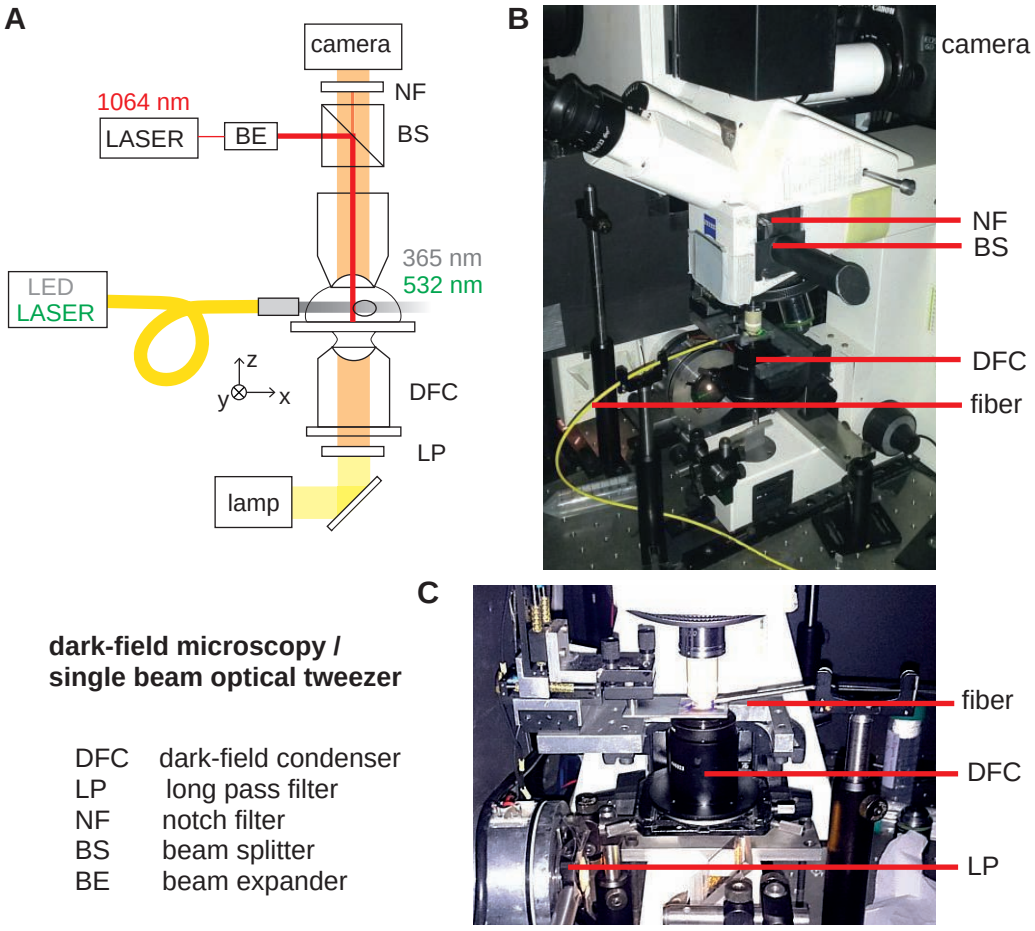

Figure 3.2 – Optical tweezer setup. (A) Schematic view of a 1064 nm laser guided through a water immersion objective used as an optical trap. Additional filters (NF, P) are inserted in the illumination paths depending on the application. (B) Picture of the setup for measuring the scattering force on an individual gold nanoparticle used (see Section 6.2). A 532 nm laser beam is coupled to the sample through an optical fiber. (C) Picture of the setup for switching vesicle mechanics (Chapter 4). A 365 nm LED is fiber-coupled to the sample.

Otherwise, directly transmitted light would be collected by the objective and thus disturb the observation. The condition of Eq. (3.1) imposes an additional challenge on the technical realization of a dark-field optical tweezer. Good trapping objectives would require a high NA while the NA of dark-field condensers is typically chosen to be rather small. In this work, for optical trapping of gold nanoparticles, a combination of a NA = 1.0 water immersion objective and a dark field oil condensor with a NA between 1.2 and 1.4 was used.

Holograhic optical tweezers (HOTs) use a computer-designed diffractive optical element to split a single collimated laser beam into several separate beams, each of which forms an optical tweezer when using a strongly focusing lens [127]. The principle of holographic imaging is illustrated in Fig. 3.3A. The first step is the calculation of a computer-generated hologram (CGH) from an 8-bit image. Several methods have been suggested for this to

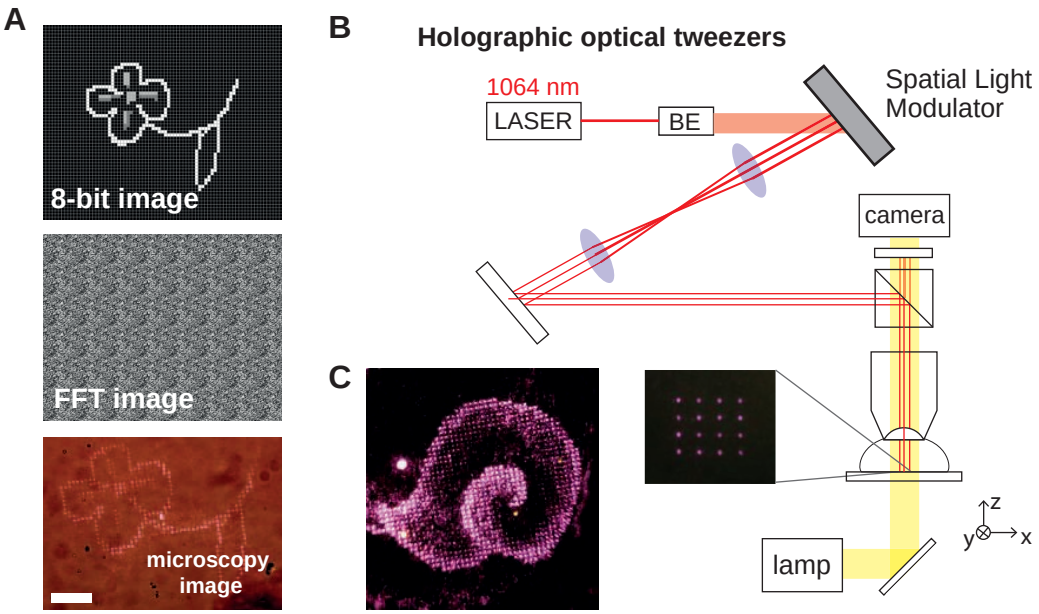

Figure 3.3 – Holographic Optical Tweezers. (A) Principle of holographic imaging. An 8-bit image is transformed to Fourier space computationally. The resulting computer generated hologram is used as an optical grating. After focusing the deflected beam through an objective lens, the image is retained in working distance from the objective. The microscopy image shows the reflection of the NIR laser beams detected by the Canon EOS camera. (B) Sketch of the optical setup. (C) Holographic images of an array of single beams and a snail shell recorded under the objective.

date [128, 129], however, the development of efficient algorithms for the computation of phase holograms has long prevented HOTs from tapping their full potential [127]. The CGH is sent via a digital visual interface (DVI) signal from the PC to a liquid crystal display, where a phase modulation of the wavefront of the incident laser light is performed pixel by pixel. A modulation of only the phase (but not the amplitude) is sufficient to form any desired intensity pattern in the focal volume of the objective and thus any pattern of traps [130]. Furthermore, spatial light modulators (SLMs) have also been used to implement light pattern carrying angular orbital momentum for stimulated emission depletion (STED) microscopy [131, 132] or for the generation of flat-top beams [133].

A HOT was implemented in an upright microscope with a 63x water objective (*ZEISS GmbH*), see Fig. 3.3B. Holographic laser patterns are created by sending a NIR beam from a 1064 nm Cobolt Rumba laser via a Liquid Crystal on Silicon Spatial Light Modulator (*Hamamatsu*, LCOS-SLM X10468-07) and coupling it through the objective. For the computation of holograms, an Iterative Fourier Transform Algorithm (IFTA) provided by the manufacturer is used [134]. The experimental configuration allows for the creation of arbitrary patterns of NIR beams either consisting of a defined image of separated traps (small image in Fig. 3.3B) or extended holographic images (Fig. 3.3C).

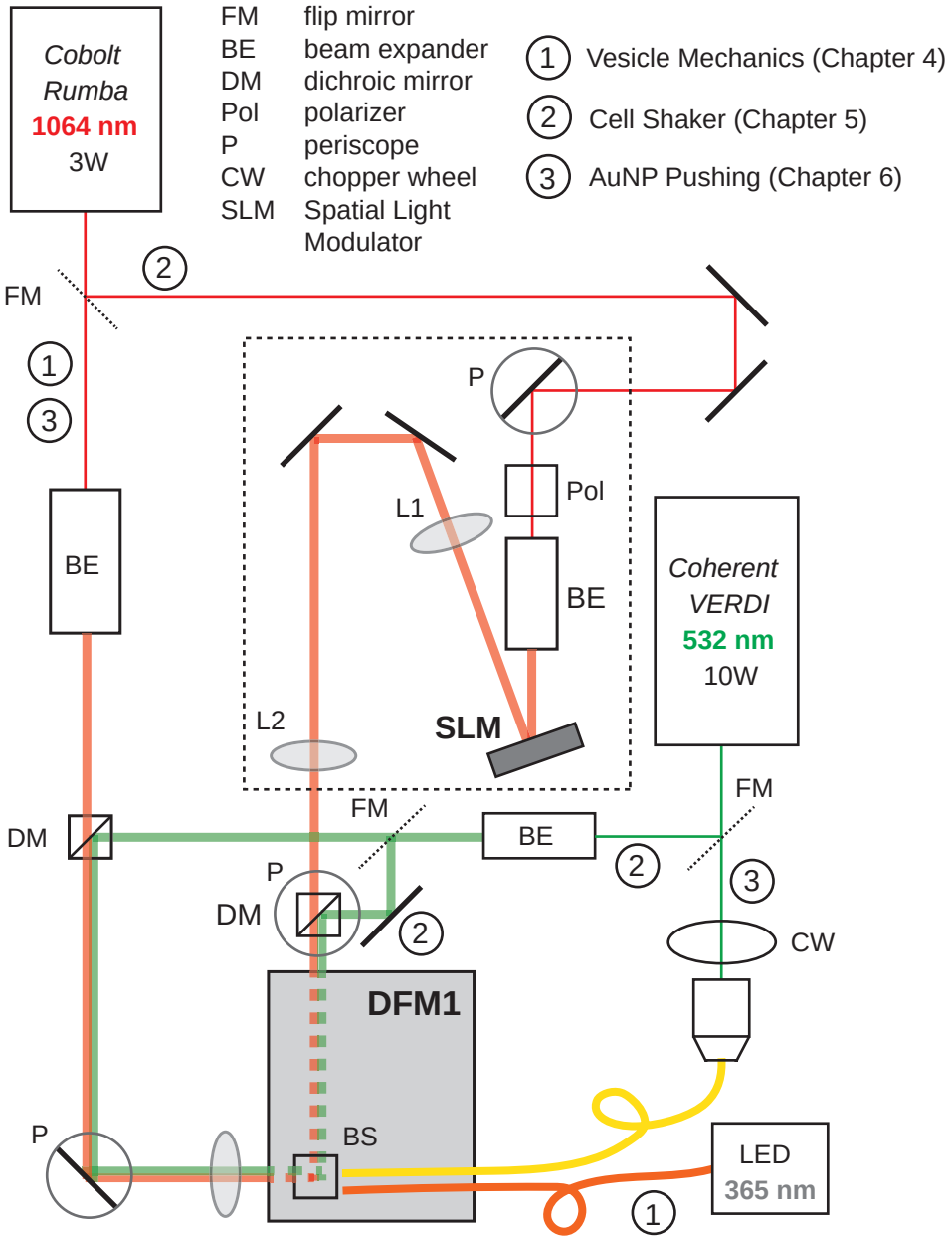

Figure 3.4 – Optical setups used in the present thesis. Sketch of the arrangement of the optical paths on the optical table at the DFM1 setup. Using flip mirrors, all experiments shown in this thesis could be integrated into the same setup. The SLM setup is arranged on a higher level compared to the optical table. L_1,L_2 denote lenses with focal lengths of 750 mm and 500 mm, respectively. The optical paths for the experiments in this thesis (denoted by 1,2,3 in circles) are simplified by omitting several alignment slopes, additional setups and additional components not relevant to the results presented here.

Setup overview and optical paths

Figure 3.4 summarizes the arrangement of the laser beams on the optical table as used in the experiments of this thesis. In Chapters 4 and 6, single beam optical tweezers with additional fiber-coupled illumination from the side were used (Fig. 3.2). For the setup shown in Fig. 3.4, a chopper wheel was positioned in the green laser beam and synchronized to the high speed camera via an *Arduino* microcontroller.

To achieve a dynamic change of the laser array, the HOT setup was used together with a single beam optical trap (532 nm). Please note that for setting up the holographic imaging path, the distances between SLM display, the lenses L_1, L_2 and the sample plane have to match the focal lengths f_1, f_2 of the lenses. These fulfil the optical image equation

$$\frac{f_1}{f_2} = \frac{D_1}{D_2}, \tag{3.2}$$

with D_1 being the diameter of the display of the SLM and D_2 the back aperture of the microscope objective. The lengths of the optical paths were chosen appropriately.

3.2 Data acquisition and processing

Accurate tracking of particles, vesicles or cells from recorded videos was either done with a digital camera or a scientific highspeed camera as detailed in the previous section. In the present section, the software and custom routines will be introduced. For the analysis of cell deformation and the determination of bending rigidities, an evaluation algorithm was developed.

Particle trapping experiments

To ensure single particle trapping, a several controls were applied. During the entire experimental procedure, the appearance of the trapped object was controlled by observing the measurement through the ocular. In general, a very low concentration of particles was used so that within the measurement time, on average, no or only a few additional particles would enter the trapping beam. If indeed a second particle entered the trap, this could not only be seen by observing the process, but also in the change of intensity of the trapped particle, the amplitude of the fluctuations or the focus of the diffraction-limited spot now consisting of two particles.

For metal nanoparticles, which can often not be distinguished by eye using the ocular, one could additionally make use of the fact that our microscopy setup comprises alternative detection pathways by a Rayleigh scattering spectrometer or by a camera. Using a Rayleigh scattering spectrometer, single particle scattering spectra can be compared to the spectrum of a trapped particle. With this information, the color of the particle seen in the ocular of the microscope or a sensitive digital camera can be associated with having indeed a single particle in the trap (and not, e.g., an aggregate) [135].

Tracking software and data analysis

In order to process data, customized scripts were written using *MATLAB*, *C++* and *Python* code. Different tracking routines were applied depending on application. In the following, the tracking software used for the experiments is listed and referenced:

1. The **Video Spot Tracker** program (National Institute for Biomedical Imaging and Bioengineering, University of North Carolina) can track either image stacks or videos of most common formats and offers different tracker types [136]. A *symmetric tracker* was applied for the tracking of micrometer sized silica beads (see Chapters 5 and 6). It operates by locating the minimum variance in concentric rings around the bead center. Using this routine provides the advantage that the tracker can follow the particle over large distances but comes with the drawback that it often fails if the particle exhibits jumps in its trajectory.

2. For tracking gold nanoparticles in an optical trap, the **Radial Symmetry Center** software published by Parthasarathy [137] was used. It is based on an analytic, non-iterative calculation of the best-fit of any radial symmetric intensity distribution, similarly to Gaussian fitting and provides sub-pixel resolution.

3. In order to track the center-of-mass of a cell (see Section 5.2), the open-source **'Cell-Evaluator'** software by Youssef *et. al.* [138] was used. The *ImageJ* plugin was originally developed for bacteria tracking and includes the possibility of considering not only shape changes but also division or annihilation events and multiple cell tracking.

4. For a more efficient center-of-mass tracking of cells (Sections 5.2 and 5.3), a versatile **2D Fourier Tracking** algorithm based on the publication by Kristensen *et al.* [139] was implemented in *MATLAB*. Here, the displacements of trapped objects are determined directly from the phase shift between the Fourier transform of subsequent images.

5. Fitting of the temporal evolution of **vesicle contours** recorded as image series or videos (see Sections 4.1 and 4.2) is based on a custom-made algorithm for ellipsoial fitting developed by Christian Roeske [140]. The combination of a *MATLAB* preprocessing ('vesikelmesser.m') and a subsequent fit of the raw data using a C++ routine ('hquick.exe') leads to an accurate ellipsoidal fitting even for a modest image quality.

To facilitate the evaluation process involving particle tracking and subsequent Fourier analysis, custom-designed graphical user interfaces (GUIs) were programmed in *MATLAB* (Fig. 3.5). A snapshot of the GUI of *SweepAnalysis* is shown in Fig. 3.5A. Two of the above mentioned tracking algorithms are implemented to work with different data formats, namely the Radial Symmetry Center *MATLAB* code and 2D Fourier Tracking. The tracking function provides a displacement time series that can subsequently processed. The

analysis function includes a power spectral density analysis, periodic averaging and a histogram evaluation. The latter is a tool to derive trap stiffnesses by using the equipartition theorem. *FTAnalysis* (Fig. 3.5B) covers a broad range of possibilities to mathematically process a time series, such as correlation analysis, Fourier and Hilbert analysis or averaging.

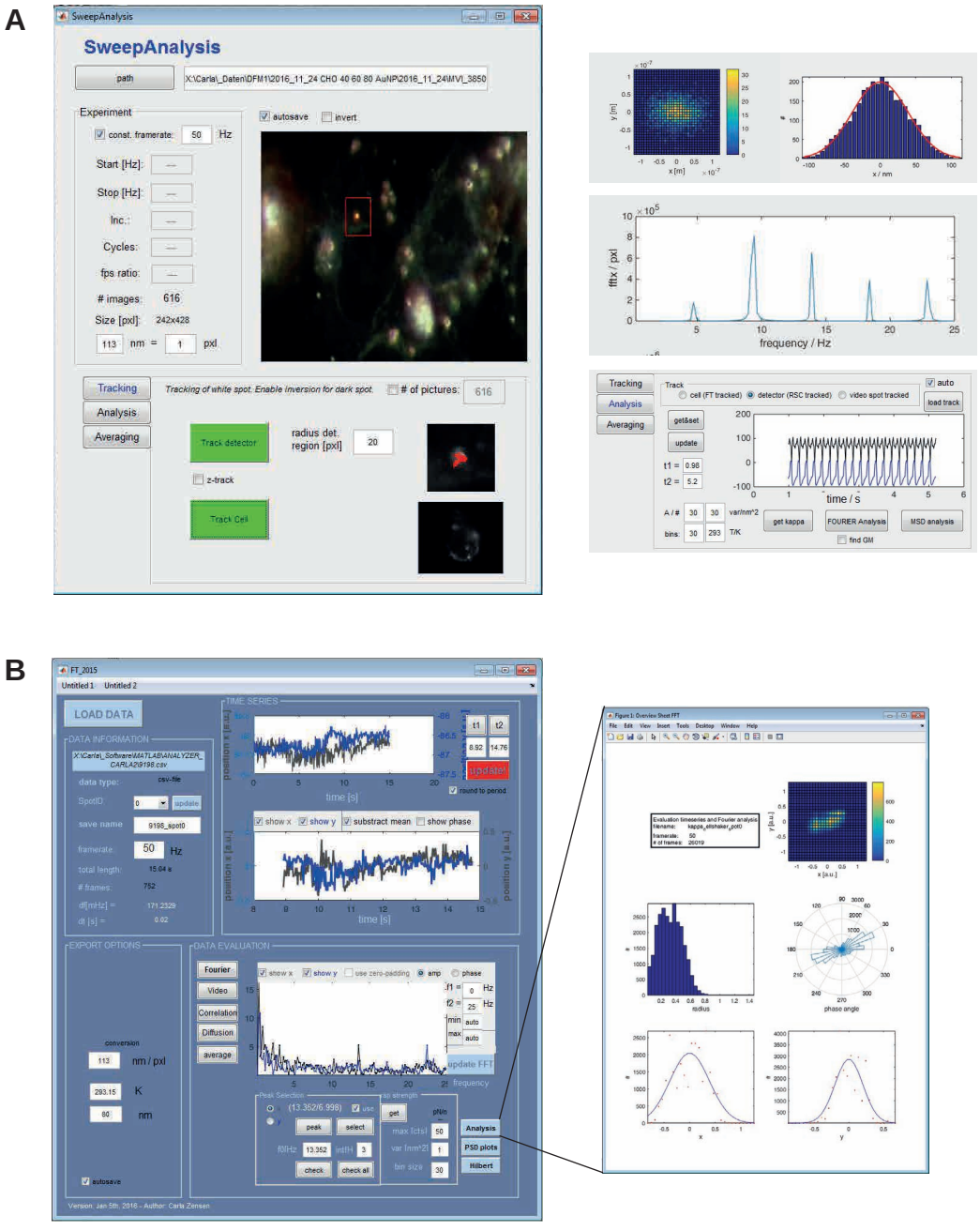

Figure 3.5 – Custom graphical user interfaces. (A) GUI for particle tracking following either the radial symmetry center algorithm [137] or the implementation of 2D Fourier tracking [139] and quick data analysis. The GUI provides a function for the determination of trap stiffness using the equipartition theorem. (B) GUI for complex data analysis of time series, including Fourier transforming, Hilbert transforming and correlation analyses.

Calculations of optical forces were done using a toolbox published by Nieminen *et al.* [115] based on the T-matrix method (see Section 2.4). For convenience, a GUI corresponding to the *MATLAB* source code was designed and implemented by Felix Winterer [141].

Optofluidic measurement of vesicle deformation

Cell deformability and bending rigidity of vesicle membranes was measured using a home-built routine based on measuring vesicle deformation in elongational counter-flow (see Fig. 3.2A for a setup sketch). Individual vesicles were fixed in the imaging plane several tens of micrometers away from the cover slide. Using a piezo stage, a microflow of up to $60\,\mu m\,s^{-1}$ was induced leading to a deformation of the trapped vesicle. While stepwise varying the stage speed, the increasing deformation of the vesicle was video-recorded at a framerate of 30 - 60 fps. Note that the length of these steps was chosen such that the vesicles evolved into their new equilibrium shapes. In order to verify that vesicle stretching did not take place, the circumference of each vesicle was measured. The resulting 2D projection of the vesicle was fitted with an ellipse [140].

The method was applied to measure maximum vesicle deformability, e.g. by a chemically induced change in vesicle membrane stiffness (see Section 4.1, Fig. 4.3). For each measured vesicle, the flow speed was increased until the deformation of the vesicle saturated at a maximum deformation value,

$$D_{\max} = \frac{|a-b|}{a+b}. \tag{3.3}$$

Here, a and b are the half-axes of the fitted ellipse. Only those vesicles were considered where a steady state elongation was confirmed. To ensure comparability, vesicles between 1 and 5 µm were considered.

A fundamental macroscopic property of lipid bilayers is the bending rigidity, κ, which is closely related to shape, stability, strength, and structural phases of the lipids [142]. In principle, a bending rigidity can be derived by measuring vesicle deformation caused by a constant flow speed. However, a better control and statistics is provided when a series of different flow speeds is measured. In order to determine a bending rigidity for the closed surface of a vesicle, the expression for curvature energy developed by Helfrich in 1973 was used [143]:

$$F = \frac{\kappa_B}{2}\int_S (c_1+c_2)^2\,dA + \kappa_G\int_S (c_1\cdot c_2)\,dA. \tag{3.4}$$

Here, the spontaneous curvature c_0 is neglected. In this equation, κ_B and κ_G are the bending moduli for mean and Gaussian curvatures, c_1 and c_2 the principal curvatures and dA a surface element. Without the application of an external force, any vesicle appears spherical with constant, size-independent curvature energy $F = 8\pi\kappa_B + 4\pi\bar{\kappa}_G$. The mechanical work W acting on the vesicle by the flow of a known speed is calculated in a numerical simulation (*COMSOL Multiphysics*) of a prolate spheroid defined by two half

axes a and b. The resulting flow profile is shown in Fig. 4.6A. With this, Eq. (3.4) can be simplified and rearranged to

$$\kappa_B = \frac{W}{1/2 \int_S (c_1 + c_2)^2 \, dA - 8\pi}, \tag{3.5}$$

which relates the mechanical work W acting on a spherical membrane causing it to bend. For intense illuminations and flow speeds, an increase of the vesicle's circumference was observed. For other cases no significant increase could be found and Eq. (3.5) was applicable. To determine the nominator, the total force acting on the vesicles (simplified as prolate spheroids) was simulated for a given flow speed and vesicle shape. The simulations were done by numerically solving the Navier-Stokes equations by the finite element method using the software *COMSOL Multiphysics*. Due to small lengths and velocities ($Re \ll 1$), a model of laminar flow could be applied (incompressible fluid, no turbulences, a fluid dynamic viscosity: 1.6 mPas, fluid density: $1055\,\mathrm{kg\,m^{-3}}$ for 0.3 M sucrose solution). The actual work done by the flow to bend the vesicle was estimated to be the simulated total force multiplied by the change in length of the vesicle with respect to its original spherical shape. An alternative, already established method of measuring mechanical parameters of vesicle membranes is the use of a micropipette aspiration setup [144].

3.3 Samples and materials

In the present thesis, different biological models and optofluidic detectors were used that are listed in the following. Many samples were provided by cooperating scientists. In the subsequent Results part (Chapters 4 to 6), footnotes provide their names and affiliations. If not indicated otherwise, the chemicals are purchased from *Sigma-Aldrich*.

Micro- and nanoparticles

In the experiments using optofluidic detection (Chapters 4 and 5), either silicon dioxide microparticles (SiO_2, *micro particles GmbH*, diameter $1 - 2\,\mu m$) or gold nanoparticles (*Nanopartz*, Accurate^{TM} Spherical Gold Nanoparticles, series A11, diameter $40 - 80\,nm$) were used, as shown in Fig. 3.6. In dark-field illumination, the size of gold nanoparticles can be distinguished by their scattering intensity and their single particle spectrum [126].

Colloidal micro-screws with a diameter of 530 nm and a length of 2.35 µm were fabricated from silicon dioxide (SiO_2) by glancing angle deposition by Dr. D. Walker in the research group of Prof. P. Fischer (MPI for Intelligent Systems, Stuttgart) as described elsewhere [145, 146]. The resulting structure consisted of a helical part and a 'head', formed by a silica bead with a diameter of 500 nm.

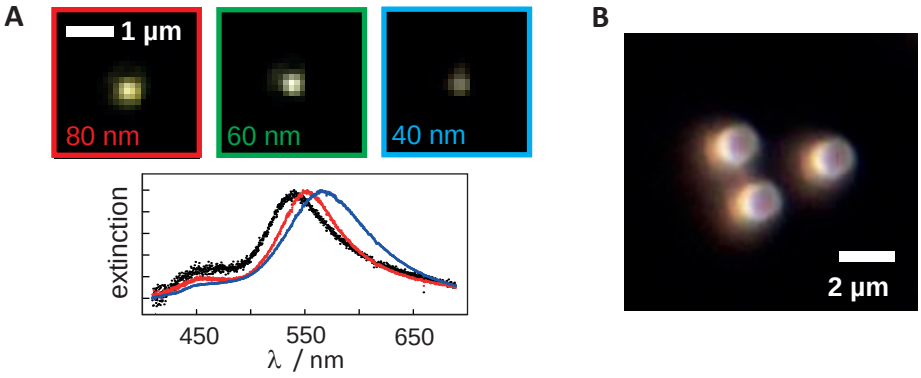

Figure 3.6 – Dark-field microscopy images of detector particles on a coverslide. (A) Gold nanoparticles with diameters of 40, 60 and 80 nm and their typical single particle scattering spectra. (B) Silicon dioxide particles with a diameter of 1.3 µm.

Preparation of vesicles

Artificial membranes made of phospholipid molecules are an established model system to emulate certain functionalities of cell membranes [147]. They can easily be doped with different surfactants and produced in different shapes, such as vesicles. In this work, small unilamellar vesicles (SUVs), giant unilamellar vesicles (GUVs), vesicles made from cell membranes and vesicles made from photoswitchable lipids were produced and used.

SUVs (10 - 100 nm) were prepared with a method based on tip sonification [148]. 100 µL of the azo-PC lipid solution was diluted with $CHCl_3$ to a final volume of 1 mL. The solvent was removed under reduced pressure, depositing layers of lipids on the wall of the round bottom flask. The flask was filled with 2 mL ddH_2O. The flask (*Elma Schmidbauer GmbH*) was sonicated briefly until the solution appeared milky and was then transferred to a centrifuge tube. Tip sonication (*BANDELIN electronic GmbH & Co. KG*) was performed for two times 30 s on ice. Finally, the sample was centrifuged for 10 min at 10.000 rpm. The supernatant was stored at 4 °C until further use.

GUVs are cell-sized vesicles that can be seen in the light microscope under dark-field or phase-contrast illumination. For the formation of *azo*-**PC** GUVs used in Chapter 4, the electroformation method [149, 150] was adapted using a homebuilt electroformation chamber. Two Pt wires, 3 mm apart, were run through nine reaction wells with a volume of 1.5 mL each. A few µL of the lipid solution was pipetted onto the wires. After evaporation of the $CHCl_3$, the wells were filled with 1.5 mL of a 300 mM sucrose solution or 1 mM of sorbitol solution. Before starting the electroformation protocol, the chamber was sealed and heated to 70 °C. Then, a voltage was applied to the wires with a function generator for 180 min. The solution containing GUVs was stored at 4 °C until further use.

A further step towards the simulation of a cell membrane is to use cell membrane vesicles that are made from cellular vesicles. All steps of the preparation of cellular vesicles were done by the group of Dr. Simone Braig and in cooperation with Prof. Angelika Vollmar (LMU Munich) [151]. SKBR3 cells were grown in 40 mm dishes and stimulated with

Soraphen A for 72 h. Culture medium was discarded and cells were washed twice with phosphate buffered saline (PBS). To induce vesiculation, 600 µL of buffer solution containing 150 mM NaCl, 10 mM 2-(4-(2-hydroxyethyl)-1-piperazinyl)-ethanesulfonic acid (HEPES, 2 mM $CaCl_2$, C5080), 8 mM di-thiothreitol (DTT, *Roth*, 6908) and 1 M paraformaldehyde (PFA) was added and the cells were incubated in a shaker (37 °C, 5 % CO_2 and 60 cycles/min) for 2 h. After shaking, the upper 3/4 of the solution was removed and used for analysis.

The photolipids were synthesized and provided by Dr. James Frank from the research group of Prof. Dirk Trauner (Department of Chemistry and Center for Integrated Protein Science, LMU Munich). *azo*–**PC** was synthesized from the photoswitchable diacylglycerol PhoDAG-1 [152] in high yield. Phosphoramidite chemistry was used to install the phosphocholine headgroup. A reaction scheme can be found in Appendix A.5 and more details are given in Ref. [153]. *azo*–**PC** could be isomerized between its *cis*- and *trans*-configurations on irradiation with UV-A and blue light, respectively. In Chapter 4, photophysical properties of photoswitchable *azo*-**PC** lipid molecules in a membrane were investigated.

Preparation of cells

For experiments with red blood cells (RBCs), a blood sample was taken from a healthy adult and diluted 20-fold in an isotonic medium based on PBS with 2 mM ethylenediaminetetraacetic acid (EDTA) and 10% fetal calf serum (FCS). Just before every experiment, the cell suspension was diluted and mixed with a suspension of 1.76 µm silica beads. Hypotonic media were prepared by replacing a known volume of PBS by deionized water (18.2 MΩcm) while keeping the concentrations of EDTA and FCS constant.

Cultured cancer cells were used in a proof-of-principle study in Chapter 5. Cell culture was done with Dr. I. Fernandez, in the group of Prof. O. Eickelberg (Comprehensive Pneumology Center, LMU Munich).

Bacillus subtilis were cultured with the help of Dr. A. Mader from the research group of Dr. M. Opitz (Chair for Biophysics, LMU Munich) as published in Ref. [11].

Chapter 4

Manipulation of Phospholipid Vesicle Mechanics with Light

Many cellular processes are closely linked to mechanical factors and force regulation [154]. While intrinsic forces mostly arise from the polymerization and contraction of cytoskeletal networks or intracellular pressure of osmotic origin, extrinsic forces are mainly due to adhesion to neighboring cells or the extracellular matrix [26]. GUVs are a versatile model system to emulate the fundamental properties and functions associated with the plasma membrane of living cells. Deformability and shape transitions of lipid vesicles are closely linked to the mechanical properties of the bilayer membrane itself and are typically difficult to control under physiological conditions. Here, a protocol was developed to form cell-sized vesicles from azobenzene-containing lipid molecules (*azo*–**PC**) that undergo photoisomerization on irradiation with UV-A and visible light. Photoswitching within the photolipid vesicles enabled a rapid and precise control of the mechanical properties of the membrane and with it, its shape.

The chapter starts with a short introduction onthe use of vesicles as biophysical model systems[1]. In the following, the response of photosensitive *azo*–**PC** GUVs on a light stimulus is analyzed. Changes in the vesicle mechanics and shape could be initiated and controlled by light with high temporal and spatial accuracy. In the third section, an example of light-controlled local storage of mechanical energy is realized. The chapter concludes with a discussion of biological situations where a light switch is of great value to further investigate the role of membrane forces.

[1] A corresponding article, entitled "Light-Controlled Membrane Mechanics and Shape Transitions of Photoswitchable Lipid Vesicles" by C. Pernpeintner, J.A. Frank, P. Urban, C.R. Röske, S.D. Pritzl, D. Trauner, and T. Lohmüller, was recently published in *Langmuir* (2017) [153].

4.1 Vesicles as a biomechanical model system

The tight regulation of cellular mechanical properties can lead to a controlled deformation of the cell membrane which is crucial for many cellular functions [155]. Examples for force-driven fundamental biological functions are cytokinesis [156], endo- or exocytosis [157], cell migration [158, 159], or formation of membrane protrusions such as lamellipodia or filopodia [160, 161]. Being the boundary between the cell's interior and exterior, the cell membrane takes part in any transition as it must adapt to the resulting cellular shape. Hence, cellular membranes undergo complex morphological changes such as budding [162], invagination [157], tube formation [163], pearling [164], or division [165].

The plasma membrane consists of a fluid bilayer of lipid molecules and membrane components that display a high level of lateral mobility [166]. From a biochemical perspective, altering the cell shape or triggering membrane deformations involves the reorganization of the lipid molecules and membrane proteins [167]. In the following, it will be investigated wether the mechanical properties of the plasma membrane alone could also drive cellular shape transitions.

Vesicle assembly

The assembly of artificial bilayers made of phospholipid molecules is a widely used method to mimic the shape and outer plasma membrane of living cells [147, 168]. Their formation is based on the attractive van der Waals interaction between the hydrophobic fatty acid tails and the hydrophilic headgroups, respectively (Fig. 4.1A) [169]. The shape and structure of a lipid bilayer depends on the lipid type, the water/lipid ratio and the temperature of the surrounding medium [170]. The bilayers can assume arbitrarily complicated lattice structures [171]. In the simplest case, the self-assembly of *micelles* is observed (Fig. 4.1B). Still at relatively low concentrations, lipid molecules assemble in *bilayers* whose thickness is of the order of 4 nm (Fig. 4.1C) [147]. Lipid bilayers may extend up to millimetres in the lateral direction. *Vesicles* or *liposomes* are membrane bubbles formed by bending and closing up a lipid bilayer (Fig. 4.1D).

Various experimental techniques have been developed for preparing liposomes of different size (from nanometers to tens of micrometers), for a review see Ref. [170]. *Small unilamellar vesicles* measure only a few tens of nanometres so that for their observation, indirect methods such as dynamic light scattering (DLS) could be applied. Vesicles in the intermediate size range (100 nm - 10 µm) have been termed *large* or *medium unilamellar vesicles* and the largest vesicles (1 - 100 µm) are called *giant unilamellar vesicles* [172]. As these have the size of cells, they are well visible under a light microscope (Fig. 4.1) and allow for direct manipulation.

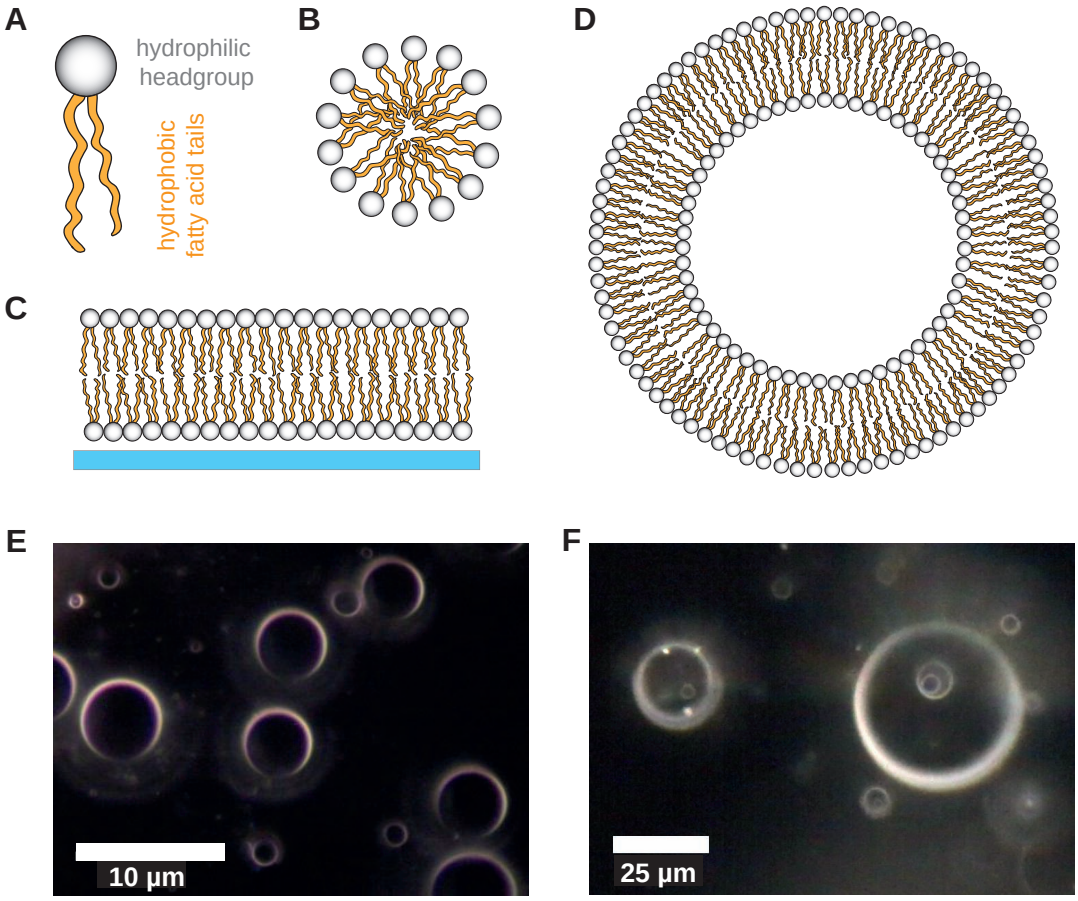

Figure 4.1 – Structures of artificial lipid layers. (A) Sketch of a phospholipid consisting of a hydrophilic headgroup and a hydrophobic fatty acid tail. (B) In case of micelle formation, the hydrophobic fatty acid tails aggregate. (C) Supported membranes are extended structures of lipid bilayers on a substrate. (D) Vesicles are lipid layers of spherical geometry that exist in various sizes. (E) LUVs and (F) GUVs made of 1,2-Dioleoyl-sn-glycero-3-phosphocholine (DOPC) lipids observed with dark-field microscopy.

Modelling vesicle shape

The basis of any theoretical shape calculation is the fact that a vesicle will always assume the shape of minimal surface energy with respect to the appropriate constraints, such as temperature or flow [173]. For a theoretical description, vesicles are seen as a two-dimensional fluid defining a thin membrane of a certain surface energy. Using variational approaches, it is then possible to calculate resulting liquid membrane shapes by summing up relevant energy contributions, that are e.g. *bending* and *stretching* energies. Interfacial terms would only become relevant for the surface energy of a solid membrane. As long as external force gradients remain small and the thermal fluctuations are relevant for shape transitions only, the approximations remain valid even for the application of external force fields. In 1973, Helfrich proposed the so-called *spontaneous curvature model* [143], which

is based on the curvature energy per unit area of a closed lipid bilayer, which can be given as:

$$f_c = \frac{\kappa_B}{2}(2H + c_0)^2 + \kappa_G \cdot K \tag{4.1}$$

Here, κ_B and κ_G are bending rigidities, c_0 is the spontaneous curvature and H and K are the mean and Gaussian curvature, respectively. Application of an osmotic pressure Δp and the introduction of a surface tension λ leads to an expression for the equilibrium shape of bilayers [174],

$$\Delta p - 2\lambda H + \kappa_B (2H + c_0)\left(2H^2 - c_0 H - 2K\right) + 2 \cdot \kappa_B \nabla^2 H = 0. \tag{4.2}$$

A parametrization of the solution of this expression results in experimentally confirmed shapes (Fig. 4.2). Equation (4.2) still forms the basis of theoretical work [173, 175]. Later, a number of alternative models including the *bilayer coupling model* [176] or the *area-difference elasticity model* [177] were proposed, predicting a large catalogue of vesicle shapes. A different approach are molecular dynamic simulations, where SUV shapes can be predicted with molecular accuracy [178].

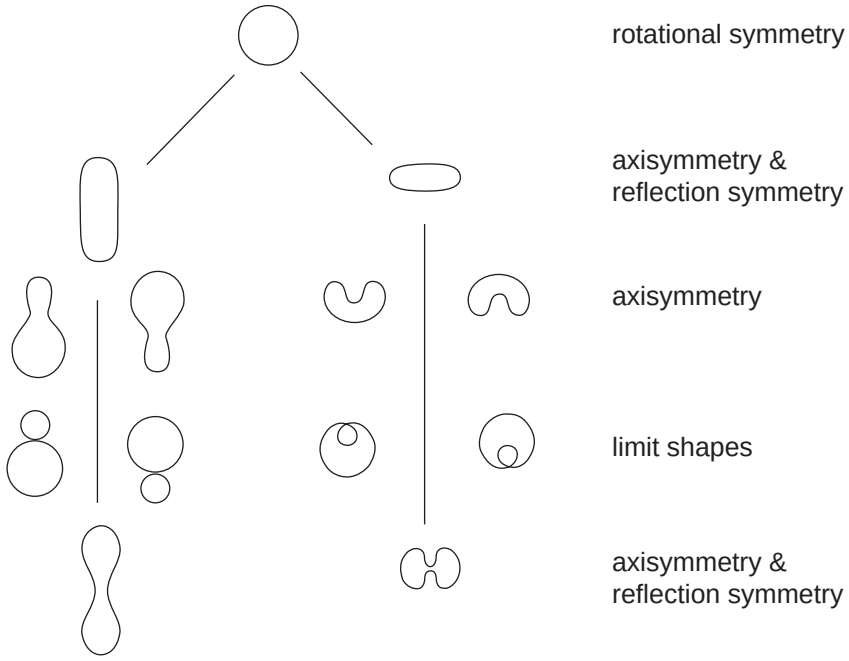

Figure 4.2 – Bifurcation scheme with stationary vesicle shapes and their symmetry [179], taken from the review by U. Seifert, Ref. [173], Fig. 11.

To test and validate theoretical models experimental parameter studies must be conducted. GUVs provide the possibility for systematic measurements of mechanical and rheological properties of bilayers as a function of membrane composition and temperature, as well as hydrodynamic and other external interactions.

Soraphen modulates stiffness of SKBR3 membrane vesicles

The identification of drugs that cause a rigidification of the cell membrane are of high interest for cancer treatment since cancer cells are assumed to be less stiff than their non-malignant analogues [180]. As an example that the composition of cellular membranes might affect mechanical cell properties like cell deformability, it was tested whether the drug *Soraphen A* modulates the mechanics of SKBR3 cells (Fig. 4.3).

Membrane vesicles gained from Soraphen A treated SKBR3 cells[2] were used, which are entirely made of biomembrane after a protocol described in Ref. [151]. To assess mechanical properties of the cell membrane vesicles, their deformability was measured as described in Section 3.2: The Vesicles were optically trapped and a constant counter-flow was applied (Fig. 4.3A,B). The maximum deformability of a vesicle was achieved by increasing the flow speed. After Soraphen A treatment the deformability of large vesicles (1 - 5 µm) was significantly reduced (Fig. 4.3C). Interestingly, as a general trend the maximal deformability of vesicles gained from SKBR3 vesicles was reduced with increasing vesicle size indicating that deformability of vesicles is dependent on the membrane curvature of the vesicles.

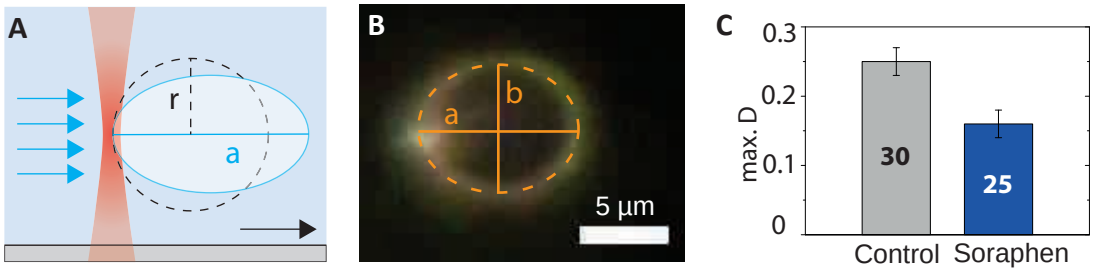

Figure 4.3 – Chemically-induced vesicle deformability. (A) Sketch of experimental setup for deformation measurements. (B) Dark-field microscopy image of an optically trapped vesicle in counter-flow. A dashed orange line indicates an elliptic fit of the vesicle cross-section with half axis a and b. (C) Maximal deformability D of vesicles with and without Soraphen A treatment for 72 h. The number of cells is given in the columns.

Regulation of vesicle shape using external stimuli

Apart from changing the chemical composition, physical stimuli such as force, temperature, and pressure can be used to tune mechanical properties of vesicles [17, 181, 182]. In response to these, GUVs display complex shape transitions that resemble the shape changes observed in living cells [183]. Experimentally, the regulation of temperature [16] or osmotic conditions [175] provides efficient control of vesicle shape. Also, nanoparticle adhesion [184] or the application of electromagnetic force fields [185–188] have been used. However, these methods lack reversibility, physiological compatibility or the possibility to control vesicle

[2] Cell culture was run and membrane vesicles were made by the group of Dr. Simone Braig (Department of Pharmacy, Center for Drug Research, LMU)

shape in a spatiotemporally defined manner. In addition, many experimental parameters can only be controlled indirectly and isolated from external parameters such as pH or temperature. To name an example, Yuan *et al.* [175] have suggested in a theoretical model that not only the intensity, but also the time dependent rate change of a stimulus could be a possible regulation factor for vesicle shape. The experimental confirmation would require a quick and homogeneous method for manipulating membranes under tightly controlled experimental conditions. Therefore, sights were set on developing an *optical* switch for the control of mechanical vesicle properties.

4.2 Controlling vesicle shape and mechanics with light

Light provides the possibility of applying reversible parametric changes to vesicle membranes with a high spatiotemporal precision [4, 8]. For optical stimulation, the studied system must first be made photosensitive. To this aim, a large catalogue of synthetic photoswitchable molecules with highly tunable properties is available that can be incorporated using (bio-)chemistry. The new field of synthetic photobiology involving applications of photoswitchable surfactants on biological systems, usually cells, is known as *photopharmacology* [189, 190]. Among the class of *photoswitches*, which are chemical compounds that undergo reversible photochemistry, the most widely used and best characterized are amphiphilic azobenzene derivatives [94]. In Section 2.3, a revision of the photochemistry of azobenzene can be found, providing the fundamentals for optical manipulation of photoswitchable systems introduced in this chapter.

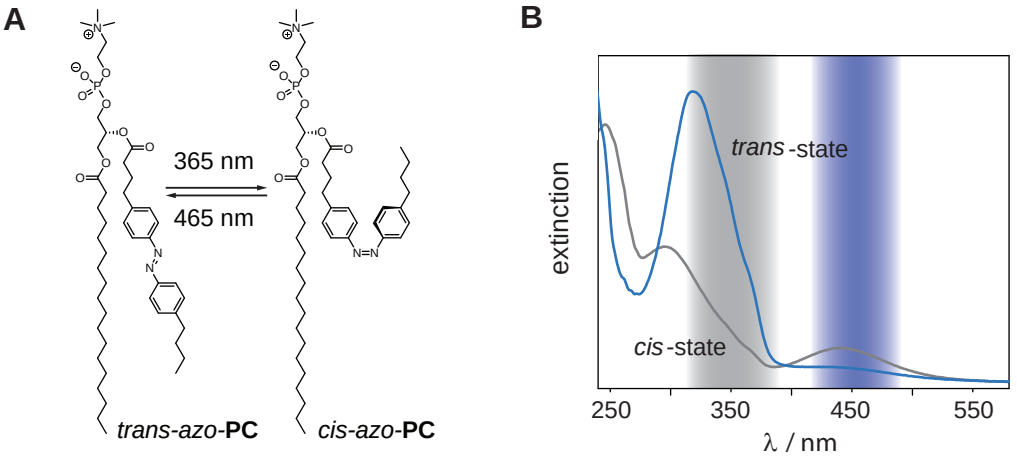

Figure 4.4 – Photoisomerization of *azo*–PC. Switching between its *cis*- and *trans*-configurations is achieved with UV-A and blue light, respectively. (A) *azo*–**PC** was synthesized from the photoswitchable diacylglycerol **PhoDAG-1** in high yield [152]. (B) UV/vis-spectra of SUVs for both photolipid isomers.

Preparation of photoswitchable vesicles

In this work, synthetic phospholipid molecules modified with an incorporated azobenzene switch (*photolipids*) were synthesized and their behavior in a membrane was studied. Azobenzene-containing compounds have been used to control the permeability of synthetic bilayer membranes [191, 192], but only a few proof-of-principle studies have investigated the possibility of observing shape transformations of vesicles that were doped with custom-designed photoswitchable amphiphiles [193–195]. Importantly, for these studies, the photosensitive part of the molecules was often located at the hydrophilic end of the bilayer membrane and not embedded within the hydrophobic center. In addition, phospholipid molecules, in which one or both of the acyl chains were functionalized with an azobenzene group, have been synthesized, and their optical properties and photoreactivity have been studied [196]. The formation of lipid bilayer membranes and vesicles from pure photoswitchable lipids has not been reported.

Photoswitchable lipid molecules can undergo a fast and reversible change in their molecular configuration upon spectrally defined illumination and prepared GUVs from 100% photolipids. A new synthetic route was developed[3] to obtain the photoswitchable phosphatidylcholine derivative (*azo*–**PC**, Fig. 4.4A). It is based on attaching the phosphocholine headgroup to the photoswitchable diacylglycerol, **PhoDAG-1**, as described earlier by Frank *et al.* [152]. Similar to azobenzene, *azo*–**PC** could be isomerized between its *cis*- and *trans*-configuration on irradiation with UV-A (365 nm) and blue (465 nm) light, respectively. The illumination periods were chosen to be at least 30 s to guarantee that the photostationary state of the sample was reached. The absorption spectra for both the UV-adapted and blue-adapted states in chloroform are displayed in Fig. 4.4B. Photoswitching could be repeated without any sign of decomposition or photobleaching, so that the blue- or UV-adapted UV/vis-spectra could be reproduced over multiple switching cycles. However, in both the molecular and membrane configuration of the lipids, an unknown portion of the molecules will remain in the alternative isomerization state[4]. An investigation of this portion could in principle be done by NMR studies and will be addressed in future research.

To observe the effects of photoisomerization in a lipid environment, a solution of SUVs was prepared from pure *azo*–**PC**. The sample was analyzed by DLS and sequentially illuminated with UV-A and blue light. As shown in Fig. 4.5, the SUV diameter changed by 3% when the sample was switched between the two photostationary states. This size increase could be attributed to an increased footprint in the bilayer membrane of *cis*-*azo*–**PC** when compared to *trans*-*azo*–**PC**. As such, the sudden change in molecular configuration

[3] All work related to the synthesis of *azo*–**PC** work was done by Dr. James Frank in the group of Prof. Dirk Trauner (Chemistry Department, LMU Munich) and is therefore described elsewhere [153].

[4] The ratio of *trans*- to *cis*-isomers is actually given by a chemical equilibrium that can be adjusted by the parameters temperature and illumination intensity and duration. For simplicity, it will be referred to the *cis*- and the *trans*-state instead of UV-adapted or visible light-adapted state throughout this chapter.

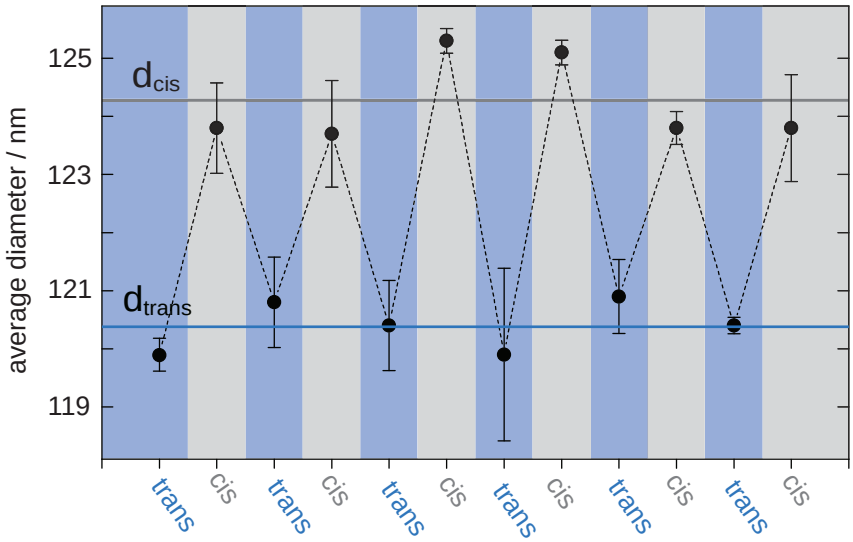

Figure 4.5 – Dynamic light scattering of SUVs. Study of the average diameter increase of small unilamellar vesicles (SUVs) on UV-A illumination by DLS.

resulted in a change of the area-to-volume ratio of the entire vesicle, which is known to be a sufficient condition for inducing macroscopic shape changes [16].

Photoswitchable vesicle mechanics

Next, the effects of lipid photoswitching on membrane properties was investigated. Therefore, a sample of GUVs was prepared from pure *azo*–**PC** via electroformation [149]. The GUVs were observed using dark-field microscopy, which does not require fluorescent labeling of the membrane. As the membrane is subject to intense white illumination by the halogen lamp of the microscope, the majority of *azo*–**PC** lipids within the vesicle membrane can thus be assumed to be in the *trans*-state. A fiber-coupled light-emitting UV-A-diode ($\lambda = 365\,\mathrm{nm}$) is used as a source of illumination for photoisomerization. To make photoswitching from *trans* to *cis* more effective and to simultaneously observe the vesicles using the dark-field, a long-pass (LP) filter ($\lambda < 505\,\mathrm{nm}$) was added to the microscope illumination path and permitted to regulate the efficiency of the switching process. In general, photoswitching from *cis* to *trans* above 505 nm was observed to be significantly slower and less efficient compared to the fast photoisomerization observed for white light illumination which includes wavelengths around $\lambda \approx 440\,\mathrm{nm}$, where the absorption of the (n, π^*) - transition has a maximum (cf. Fig. 2.5B). A NIR optical tweezer was employed to trap indivial vesicles and allow for their further investigation.

Similar to the experiment shown in Fig. 4.3, a weak counter-flow was applied to a trapped vesicle by moving the microscope piezo stage in the horizontal direction (Fig. 4.6A). Importantly, the flow speed for each experiment was kept at low values to avoid significant membrane stretching, which was verified by measuring the vesicle circumference. Application of UV-A light led to instantaneous visible fluctuations of the GUV membrane

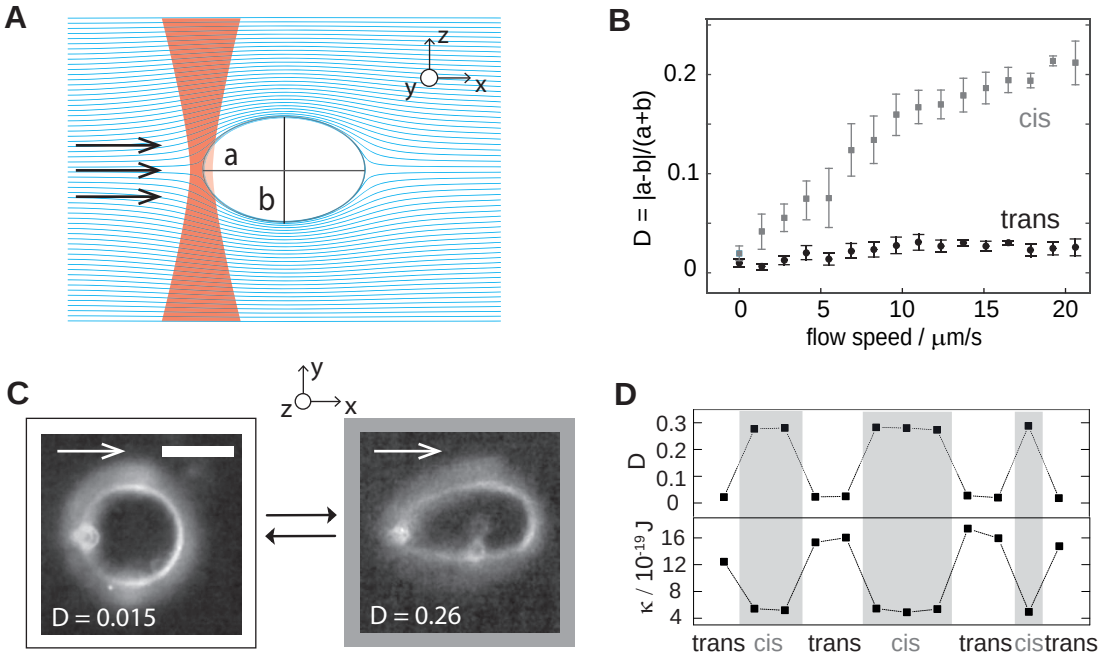

Figure 4.6 – Deformation and bending rigidity of photolipid vesicles. (A) Sketch of the experimental setup. (B) Deformation in dependence of applied flow speed for *cis*- and *trans*-state of the photolipids. (C) An optically trapped vesicle (scale bar: 10 µm) shows visible deformation under UV-A-illumination. (D) Reversible changes in deformation and bending rigidity on illumination with UV-A and visible light.

and a further deformation of the vesicle shape (Fig. 4.6C). This observation suggests that changes in the mechanical properties of the membrane can be quantified by the bending rigidity κ_B [142]. To estimate the change of κ_B on photoisomerization, the bending rigidity was measured as described in Section 3.2. The flow speed-dependent deformation

$$D = |a - b| / (a + b) \tag{4.3}$$

of the GUV with half axes a and b for both the *trans*- and *cis*-configurations of the photolipids was measured and plotted for comparison (Fig. 4.6B). Almost no deformation was observed for vesicles under the dark-field illumination, whereas vesicles that were exposed to low intensity UV-A light ($\leq 0.5\,\mathrm{kW/cm^2}$) displayed a strong elongation in the flow direction. For this case, energy conservation relates the bending energy to the fluidic deformation (Eq. (3.4)). As detailed in Section 3.2, this results in an expression for the bending rigidity of vesicles reading

$$\kappa_B = \frac{W}{1/2 \int_S (c_1 + c_2)^2 \, dA - 8\pi} \tag{4.4}$$

Applying Eq. (4.4) to the data shown in Fig. 4.6B, a strong decrease of the bending rigidity by almost two orders of magnitude was found from $\kappa_{trans} = (1.0 \pm 0.6) \times 10^{-17}$ J to $\kappa_{cis} = (5.4 \pm 1.8) \times 10^{-19}$ J before and after UV-A illumination. Similar results were found for GUVs of different sizes, and for different flow speeds (see Appendix A.6). Furthermore,

the values for the bending rigidities in the cis-state were found to match literature values measured for vesicles in the fluid phase [172]. The large change in the bending rigidity induced by photoswitching is in the same regime as a structural phase transition within the bilayer [172, 197]. Importantly, the vesicle deformation, along with the bending rigidity, was found to be fully reversible and switching back and forth was possible over multiple cycles (Fig. 4.6D).

Light-induced shape transformations

In both theory and experiments, the bending rigidity has been identified to be an important factor to trigger shape transformations of GUVs [183]. Based on the findings in the last section, the possibility of controlling vesicle shape transformations merely with light were investigated. For these experiments, the GUVs were not trapped by a laser beam and no additional flow was applied to control vesicle deformation. For illumination with high intensity UV-A light ($>1\,\mathrm{mW\,cm^{-2}}$), the emergence of vesicle shape fluctuations was observed upon photoswitching (Figure 4.7). These eventually led to strong deformation or shape transformations such as budding, protrusion formation or pearling.

Several examples for budding and invagination phenomena of GUVs before and after photoswitching are shown in Fig. 4.8. The transitions usually happen on a time scale of only a few seconds (Fig. 4.8A). Once the UV-A light was switched on, membrane fluctuations increased, probably being caused by the emergence of local bending moments, and the GUV eventually separated into two vesicles conjoined by a thin membrane thread. When white light was switched on, these vesicles often split into two separate smaller vesicles. Budding or invagination can take place on several sites (Fig. 4.8B,C). Figure 4.8D shows how UV-A light can trigger the 'exocytosis' of a smaller vesicle from a GUV.

Fine-tuning the illumination intensity and duration allowed to control a single budding or vesicle-splitting event with a high degree of spatiotemporal control. The temporal evolution of this process is shown in a kymograph in Fig. 4.9. As mentioned earlier, an LP filter was used to allow for viewing of the vesicles in the dark-field during UV-A illumination. For the incomplete budding event shown in Fig. 4.9, the LP filter was not removed when switching UV-A illumination off (orange frames). If, in contrast, the LP filter was removed entirely from the illumination path, the sample was irradiated with white light also containing the wavelength range below 505 nm. This renders *cis*-to-*trans*-isomerization of the photolipids so efficient that the stronger external stimulus caused a faster transition to the photostationary state and sequential rupture of the membrane thread. Remarkably, this observation also supports previous theoretical models which suggested that the stimulus rate might contribute to shape regulation [175].

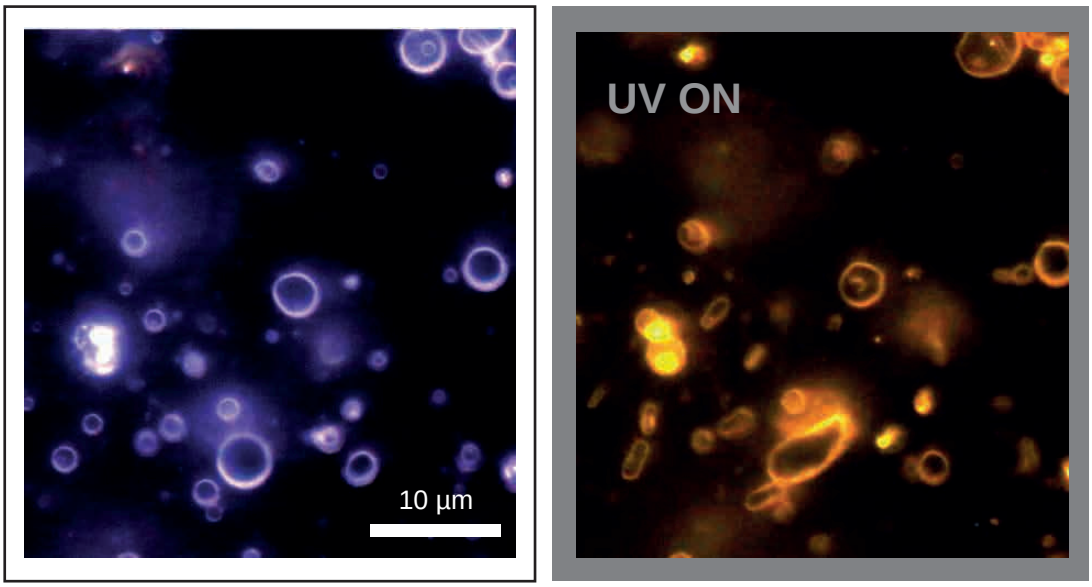

Figure 4.7 – Shape changes of *azo*–PC vesicles. The observation was done with dark-field microscopy and perpendicular illumination first with white light followed by illumination with UV-A light and $\lambda > 505\,\text{nm}$.

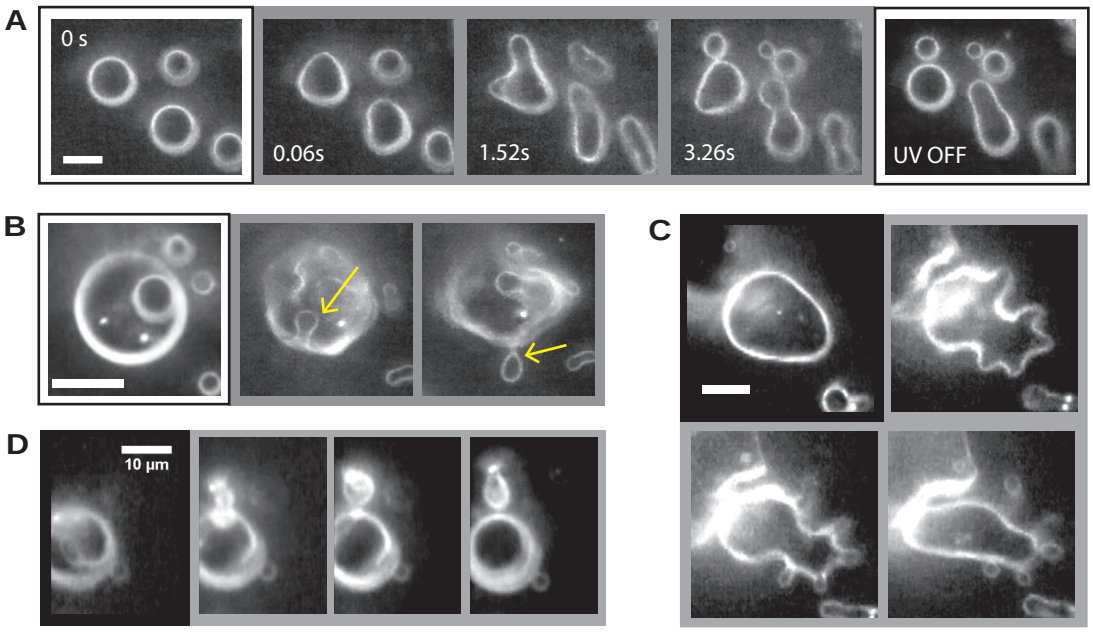

Figure 4.8 – UV-A light-induced budding of photoswitchable vesicles. White frames: white light illumination; gray frames: UV-A illumination and $\lambda > 505\,\text{nm}$. Scale bars: 10 µm. (A) Budding of several vesicles within a few seconds. White light illumination can cause an irreversible rupture of vesicles. (B) Budding and invagination events. (C) Budding at several sites. (D) On irradiation with UV-A light, a vesicle exits a larger vesicle.

Furthermore, the membrane protrusions could undergo further elongation and membrane tube formation. This was observed to happen within seconds for low-intensity UV-A illumination ($< 1\,\mathrm{mW\,cm^{-2}}$) of already deformed vesicles. The emergence and dynamics of pearling transitions (Fig. 4.9) could be reversibly controlled. UV-A illumination of a tube-shaped vesicle caused its compartmentalization into several connected daughter vesicles arranged like a pearl chain. Again, this process was completely reversible. Also, complete membrane fission and rupture of the vesicle chain was observed if the membrane was switched rapidly from *cis* to *trans* (Fig. 4.9B).

In conclusion, the introduction of membrane bending moments through photoswitching alone can result in rapid membrane compartmentalization and fission. This makes photoswitchable vesicles a valuable tool for either the controlled formation of different chemical reaction spaces or as a minimal model system to mimic biological cell fission.

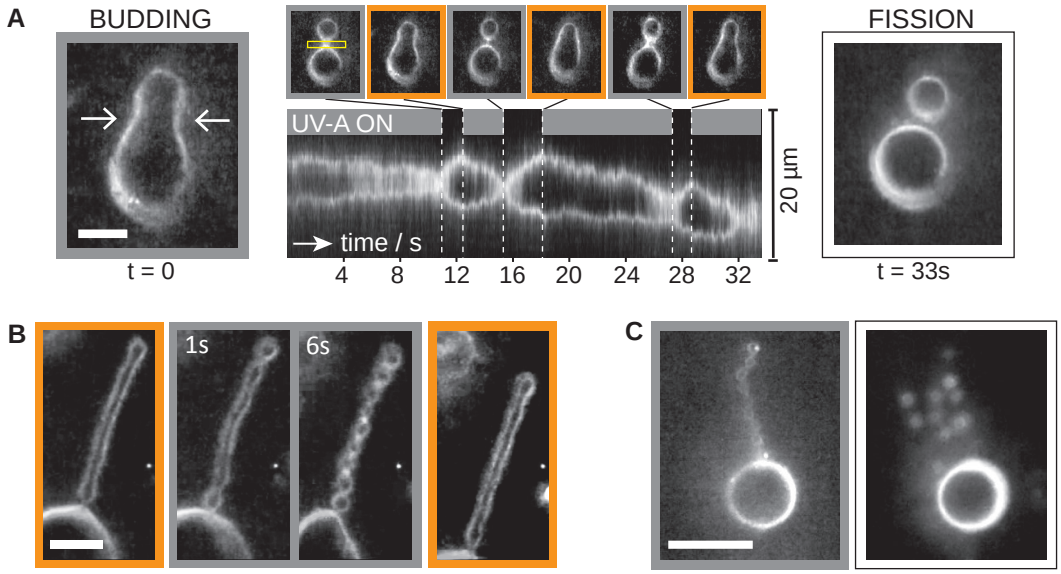

Figure 4.9 – Spatiotemporal control of budding and pearling. White and gray frames as in Fig. 4.8; orange frames: illumination with $\lambda > 505\,\mathrm{nm}$. Scale bars: 10 µm. (A) The kymograph shows the temporal evolution of the cross-section indicated by the two white arrows. In a final step, the vesicle is split by intense white light illumination. (B) On a timescale of seconds, an elongated tube undergoes a pearling transition induced by UV-A illumination. (C) Intense white light illumination causes rupture of a pearl chain.

4.3 Local storage of mechanical energy

Finally, the relationship between UV-A illumination density and *azo*–**PC** membrane mechanics was investigated in more detail to devise a strategy for transferring controlled membrane deformations into mechanical work. This was achieved by optically trapping *azo*–**PC** vesicles for different UV-A illumination intensities at a constant flow speed. The experimental configuration was identical with the one used for the deformation measurements (see Fig. 4.6A).

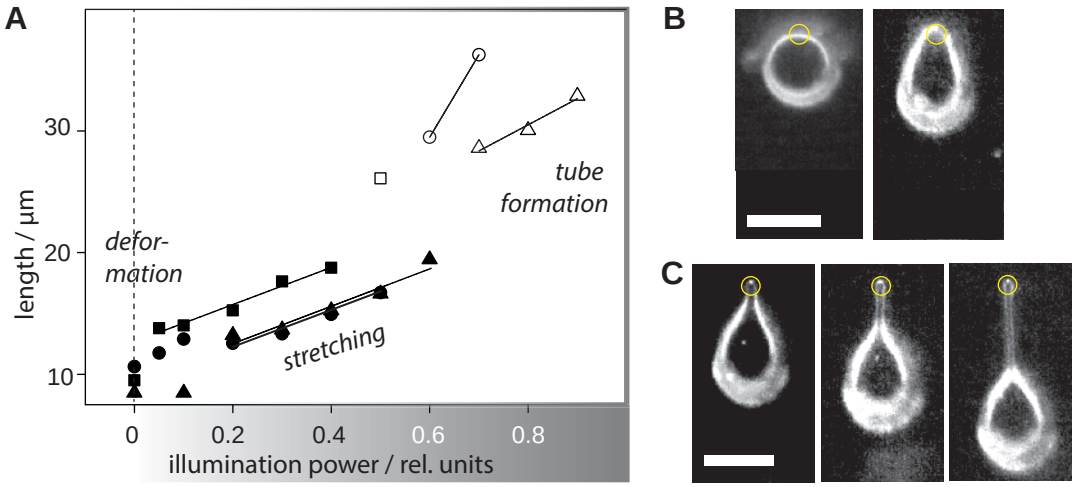

Figure 4.10 – Tuning mechanical membrane properties light. (A) Dependence of trapped vesicle shape on UV-A illumination intensity for three vesicles. Full laser illumination intensity is 70 mW. Filled symbols indicate deformed vesicles, empty symbols stand for the formation of a tube. The flow speed was $20\,\mu m\,s^{-1}$. Vesicle length is measured from the position of the optical tweezer to the most distant visible membrane piece. (B) Dark-field microscopy snapshots of a deformed vesicle (first row) and an example of tube formation for increasing illumination intensities (second row). The yellow circles indicate the position of the optical trap. The scale bar measures 10 µm.

Figure 4.10 shows the illumination-dependent increase of the length of three representative vesicles of similar size in case of a constant applied flow. Here, vesicle length is defined as the distance between the optical tweezer and the most distant part of the vesicle in radial direction. In the regime of low intensity UV-A light (cf. Fig. 4.6), an abrupt onset of vesicle deformation was observed. At increasing illumination strengths, the elongation of the vesicle displayed a linear dependence with the illumination intensity, reminding of a Hookean spring. As mentioned earlier, vesicle elongation remained stable and the process was reversible if both the flow speed and illumination intensity were kept constant. Eventually, at intense irradiation powers ($\geq 1\,mW/cm^2$), a membrane tube of tens of micrometers in length could be pulled from the vesicle. For a further increase of UV-A illumination strength, also here, a Hookean regime was observed. If the UV-A light was switched off, the tube retracted back into the vesicle while undergoing a fast pearling transition (Fig. 4.11).

It was observed that, for intermediate and high UV-A intensities and the presence of counter-flow, the membrane tubes could be repeatedly pulled out from a single vesicle with a high success rate and at arbitrary positions around the vesicle. While laser-induced tube pulling has been shown before [185], the possibility of switching it on and off for a constant trapping laser power offers a new mode of control.

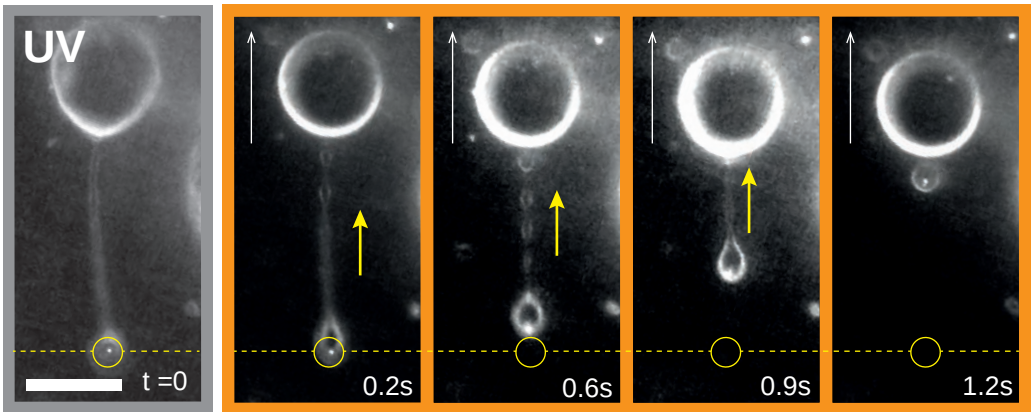

Figure 4.11 – Local energy release of a membrane tube. Pulled from a vesicle with an optical tweezer in presence of a counter-flow of $20\,\mu m\,s^{-1}$. The yellow circles mark the position of the optical tweezer in the dark-field microscopy snapshots. If the UV-A light is switched off (with LP filter inserted and thus, illumination with $\lambda > 505\,nm$), the membrane tube retracts from the optical tweezer while undergoing a pearling transition.

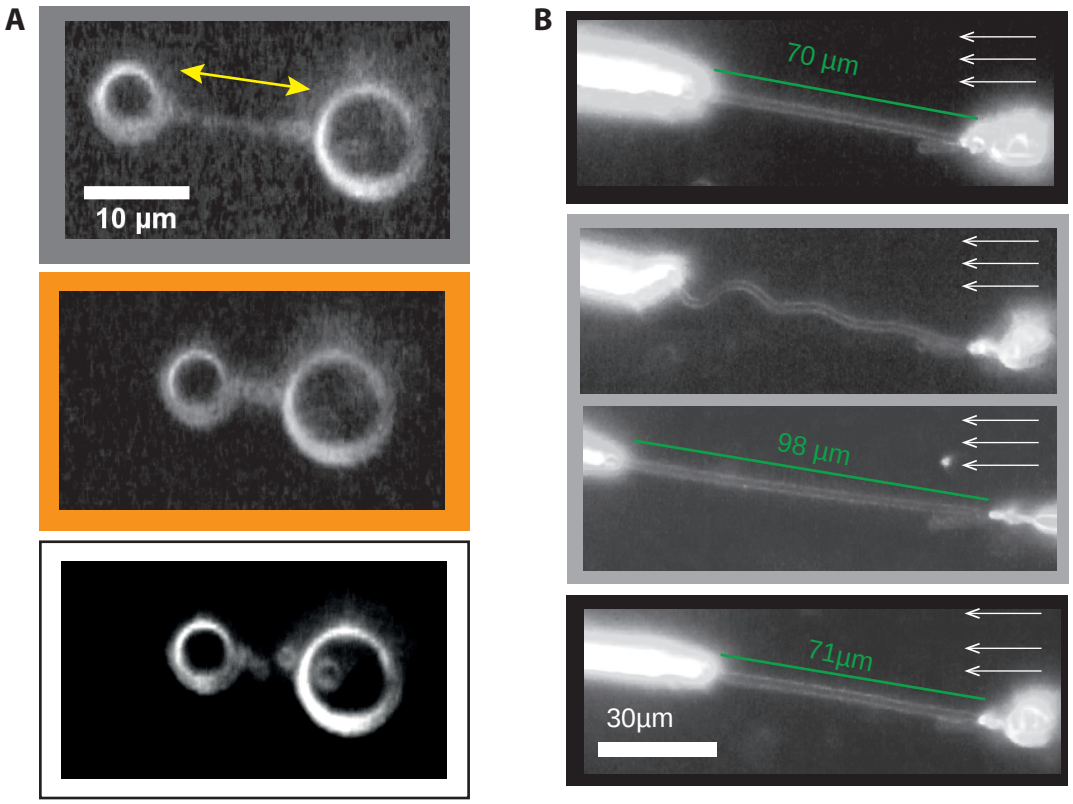

Figure 4.12 – Excerting local forces using photoswitchable membrane tubes. (A) The distance between two vesicles connected by a membrane tube can be decreased when switching off the UV-A illumination. The tube undergoes a pearling transition. (B) The length of a membrane tube is controlled reversibly by UV-A light.

First, at constant laser power, the evolution of a tube is accomplished at constant temperature and for unchanged chemical composition by only changing membrane mechanical properties. Second, the local release of stored stretching energy is enabled by a light switch in an arbitrary point in time. Pulling the tube out of the optical trap requires retraction forces in the order of pN to overcome the trapping force of the optical tweezer [198]. Forces of this magnitude are observed in the context of filopodia retraction in living cells [199]. Here, it was observed that a bilayer tube alone can exert forces caused by conformational changes of the membrane lipids. Considering a tube length of 10 µm, this force corresponds to an estimated stretching energy according to

$$E_{\text{stretch}} = 1\,\text{pN} \cdot 10\,\mu\text{m} = 1 \times 10^{-17}\,\text{J}, \tag{4.5}$$

which is orders of magnitude higher than thermal energy at this length scale [14]. Also, without the use of an optical tweezer, thin membrane tubes could be used to excert local forces in reaction on UV-A illumination. In Fig. 4.12, two examples are shown where an optically switched membrane tube regulates the distance between attached larger membrane objects. Membrane tubes were always observed to be longer when UV-A-illuminated and could retain their original length when restoring the initial illumination conditions (Fig. 4.12B).

In summary, it could be shown that mechanical energy in an order of magnitude that is relevant for cellular processes can be stored in a prestressed photoswitchable membrane tube. Using a light switch, distances on the microscale can be adjusted and bilayer thickness can be tuned with molecular precision.

4.4 *Discussion:* Switching membrane mechanics with light

It was shown that photoisomerization of membranes made entirely of photolipids allows for unprecedented control of membrane mechanics and vesicle shape transformations on a timescale of only milliseconds to seconds. By varying intensity and dynamics of the optical stimulus, controlled vesicle shape changes such as budding transitions, invagination, pearling, or the formation of membrane tubes were achieved.

The immediate effect of photoswitching on membrane mechanics was characterized using optical tweezers and flow measurements. Membrane bending rigidity changes up to 1.5 orders of magnitude on UV-A illumination. Furthermore, an increase in vesicle diameter was measured and thus an increase of membrane area could be predicted. On a molecular level, both is usually related to a change in molecular fingerprint [169]. For azobenzene molecules, in addition to shape and dipole moment changes, the end-to-end distance of the *trans*- and *cis*-isomers is known to change by 3.5 Å [200]. A calculation of the geometric change of *azo*–**PC** molecules is however not possible without the knowledge of the ratio of the two isomers in the membrane for a certain illumination.

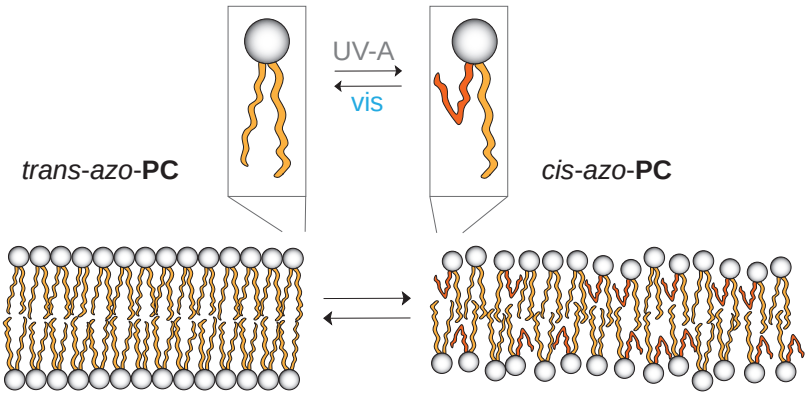

Figure 4.13 – Switching membrane configurations with light. Sketch of the structural changes of individual *azo*–**PC** molecules and membranes with and without UV-A illumination. Illuminated *azo*–**PC**-membranes show a lateral size increase and become thinner.

With an increasing amount of *cis-azo*–**PC** in a UV-A illuminated membrane of 100% *azo*–**PC**, the membrane occupies more space in lateral direction (Fig. 4.13). This could likely change the diffusion coefficient. At the same time, on average the membrane becomes thinner, which could affect permeability. Both area expansion and thinning can contribute to the observed decrease in bending rigidity. In the simplest model, illustrated in Fig. 4.13, *trans-* and *cis-azo*–**PC**-isomers are randomly distributed in 2 dimensions. However, in reality the aggregation of isomers is more likely leading to the formation of nano- or microdomains and has been reported before for azobenzene-containing membranes [191, 201]. In contrast to previous experiments, the present photolipid system allows for the investigation of pure phospholipid bilayer effects without any additional surfactants.

Using photoswitchable GUVs, it was possible to mimic the morphology changes similar to those seen in cells. Dividing and organizing lipid membrane vesicles into artificial reactions sites that enclose (bio)chemical reagents renders it possible to emulate function and behavior of protocells. For example, budding and subsequent fission of vesicles remind of cell division. *In vivo*, this process is usually connected to a cascade of complex biochemical reactions involving many reagents [202]. However, it has also been shown that certain bacterial cells (L-forms) are able to divide without the existence of a protein cell division machinery [203]. Instead, these bacteria utilize a mechanism that involves the formation of membrane protrusions and a subsequent resolution of the cell body into smaller daughter cells. These events involve membrane budding and self-reproduction of cellular vesicles seemingly without the requirement of active force generation. Figure 4.14 shows a comparison between protrusion-resolution events of L-form *Bacillus subtilis* cells (Fig. 4.14A,C) and pearling transitions of *azo*–**PC** vesicle tubes (Fig. 4.14B,D). Their striking similarity illustrates that the presented photoswitchable vesicles could serve as a valuable model system to further study the dynamics of cell fission events and, in general, processes that involve membrane budding such as endo- and exocytosis.

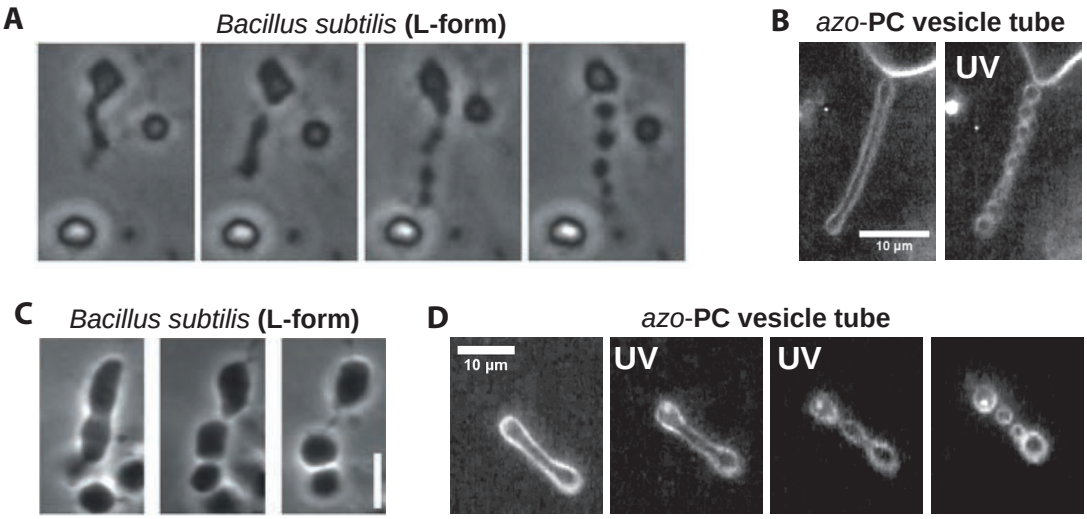

Figure 4.14 – Mimicking bacterial reproduction. Comparison between bacterial reproduction events by protrusion resolution mechanism (taken from Leaver *et al.* [203]) and pearling transitions of *azo*–**PC**-vesicles [153]. The illumination with UV-A light is indicated in the pictures. (A) and (C): still images of reproducing bacteria. (B) and (D): UV-A light-induced pearling transitions of *azo*–**PC** membrane tubes. While the reproduction of bacteria takes minutes, pearling transitions of vesicle tubes can be induced within only a few seconds.

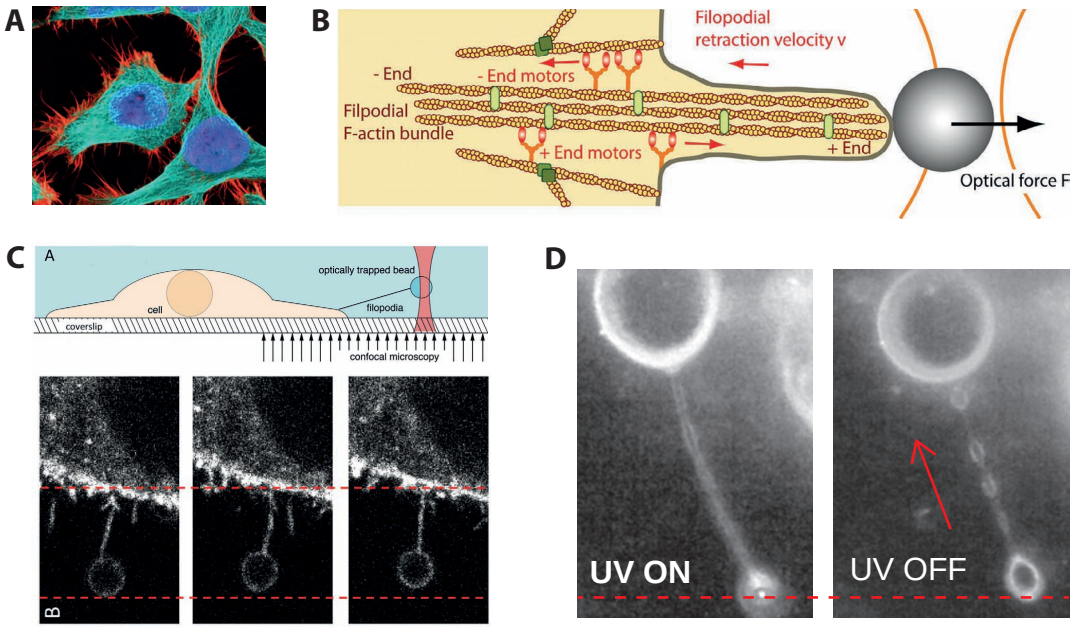

Figure 4.15 – Cell filopodia dynamics. (A) Filopodia (red dye) are cellular membrane protrusions involved in migration (image by T. Deerinck, NCMIR). (B) Sketch of filopodia structure and mechanics when pulled with an optical tweezer [204]. (C) Measurement of filopodia retraction dynamics by Romero *et al.* [205]. (D) Measurement of retraction of a membrane tube pulled from an *azo*–**PC** vesicle. The dashed red line indicates the vertical position of the optical tweezer.

Secondly, it was observed that membrane tubes could be repeatedly pulled out from a single vesicle with a high success rate and at arbitrary positions around the vesicle. These protrusions remind a lot of cell filopodia (Fig. 4.15A), which are cellular protrusions that are involved in cell motility and migration. Their mechanics and dynamics is still not entirely understood, especially concerning the interplay of cytoskeleton, cell membrane and membrane proteins under conditions of tensile stress [199, 204, 205] (Fig. 4.15B). The possibility of light-triggered storage and release of stretching energy from filopodia-like membrane protrusions on demand might allow for a *bottom-up approach* [206] modelling of the fundamental aspects of filopodia mechanics.

In light of these findings, the question arises how cellular shape transformations such as budding, invagination, division or fusion could be initiated and regulated in response to a mechanical stimulus of the plasma membrane alone [207]. The obtained results demonstrate that even in the absence of any active intracellular force-generating system such as the cytoskeleton, the introduction of membrane bending moments through photoswitches can result in rapid membrane compartmentalization and fission. In this context, photoswitchable vesicles represent a minimal model system to disentangle effects originating from the membrane mechanics and effects due to the active network of the cytoskeleton under accurately controlled conditions.

Chapter 5

Cell-Fluid Coupling Spectroscopy

In the previous chapter, light was used to tune mechanical properties of custom-designed vesicles, which can help to understand the mechanistic role of the cell membrane. The present chapter focusses on entire cells that are in the following seen as individual objects possessing a number of distinct mechanical properties. Mechanical changes of cells are often closely linked to the pathophysiology of human diseases such as malaria [208], sickle cell anemia [209], asthma [210], and cancer [154, 211]. In cancer research, for example, malignant cells have been found to be softer compared to healthy ones, which is assumed to facilitate leaving of a tumor site and shedding into the bloodstream [212, 213]. While the role of intracellular forces has been recognized for many cellular processes, the impact of the cell's mechanical properties on its fluidic environment is usually overlooked. Consequently, the question if fluidic interactions between eukaryotic cells may play a role in mediating cell-cell or cell-substrate interactions through the fluid has not been thoroughly investigated to date. However, it stands to reason that the cell's mechanical properties might also affect the microflow around themselves.

In this chapter, an optical method, *Cell-Fluid Coupling Spectroscopy* (CFCS), is presented that allows for distinguishing one cell from another by the fluidic interactions of the cells with their environment[1]. Applying holographic optical tweezers (HOTs) allows for controlled 'shaking' of a single cell. Then the apparent vibration spectrum, which is characteristic for each cell, is recorded using an optically trapped detector bead. In the first section of the chapter, the principle of cell shaking will be introduced, including an instruction of how to interpret the so-called fluidic spectra and a suggestion for a mathematical model. In the following, different applications will be demonstrated: a proof-of-principle study shows that CFCS can be applied to distinguish single cells each other. In a more advanced study, the technique is extended to a mechanical dynamical analysis, which is a promising approach towards a mechanical characterization of cancer cells.

[1] Related work was published in *Advanced Science* (2016) under the title "Detecting Swelling States of Red Blood Cells by Cell-Fluid Coupling Spectroscopy" by C. Zensen, I.E. Fernandez, O. Eickelberg, J. Feldmann, and T. Lohmüller [214].

5.1 The cell as a mechanical filter

CFCS is a new diagnostic method to distinguish and discriminate single cells due to their mechanical properties from other cells in a sample. In the following, its mode of operation will be introduced, including the experimental strategy (*cell shaking*), data interpretation (*fluidic spectra*) and a mathematical model. The latter relies on seeing the cell as a mechanical filter in terms of a *signal processing* approach. As a model system, red blood cells are used, however the generalization of the method to other cell types will be demonstrated in a later section.

Experimental setup for cell shaking

In CFCS, a single cell, e.g. from a blood sample (Fig. 5.1A), is moved in a known, periodic fashion resulting in *cell shaking* (Fig. 5.1B). The emerging microflow in the vicinity is recorded by a trapped detector bead. To experimentally realize CFCS, a multiple beam optical tweezer setup based on a spatial light modulator was built around an upright light microscope (see Section 3.1 for details). The setup allows to create arbitrary arrays of 1064 nm laser spots for trapping the cell of interest. Depending on the geometrical, mechanical and optical properties of the cell, the configuration can be customized in order to confine the cell in a very controlled manner in three dimensions. The use of NIR laser traps with a wavelength within in the second biological window reduces the danger of photodamage to a minimum [124, 215].

Examples of cells trapped in typical measurement configurations with a line of three identical focused NIR laser beams are shown in Fig. 5.1B–F. In Fig. 5.1C and D, the laser traps were periodically rotated around the axis of the first beam with a maximal angular displacement of 50° and a repetition rate of 2.14 Hz. As soon as the laser beam pattern changed, the cell reoriented in order to follow the force gradient [7]. In this way, the cell can be forced to move in an arbitrary rhythmic pattern by periodically moving the laser beam array making use of the adjustable picture rate of the spatial light modulator (see Fig. 5.1C). Figures 5.1E and F present overlays of two horizontal and vertical shaking steps of RBCs, respectively. Figure 5.1G, in contrast, shows cell shaking of a lung cancer cell in vertical direction. In this case, five laser beams were used for optical trapping. We usually chose oscillation frequencies in the low Hz regime. The application of higher frequencies would in principle enable a faster measurement and with this, a better resolution of the detected properties. However, as the maximal displacement of the cell movement decreases dramatically and the detection is limited by the data acquisition sampling (here by a framerate of 50 fps of the digital camera), shaking frequencies are chosen to be less than 10 Hz in this proof-of-principle study. Examples for CFCS measurements using frequencies about an order of magnitude higher can be found in Section 5.3.

The movement of the cell in the surrounding medium resulted in the emergence of a flow field in the vicinity of the cell. To measure the microflow dynamics, an individual silica bead, typically $1 - 2\,\mu m$ in diameter, was optically trapped with an independent optical tweezer ($\lambda = 532\,nm$) located a few micrometers away from the cell during a cell shaking experiment. Videos of sufficient length (tens of oscillation cycles) were recorded with a digital camera approriate to the cell shaking frequency. By realigning the laser, the detector position can be varied arbitrarily. A tracking of the particle movement allows for detecting small disturbances in its Brownian movement, such as the water wave stemming from the shaken cell. In this way, the detector particle works like a microphone recording any vibration in the vicinity of the investigated cell. Due to the frequent repetition of the rhythmic cell shaking, the otherwise too weak signal can be detected as a peak in the Fourier spectrum of the detector particle.

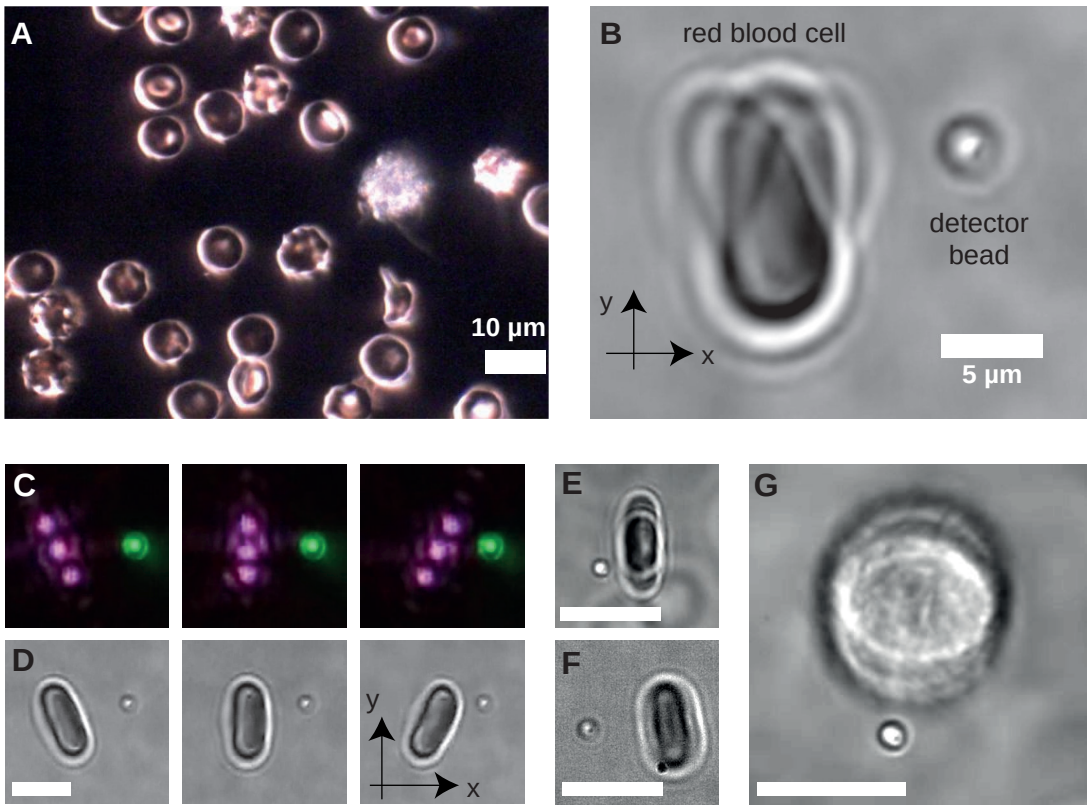

Figure 5.1 – Experimental configuration for cell shaking. (A) Dark-field microscopy image of a diluted blood sample (10.000 fold). While the majority of cells are RBCs, also a white blood cell can be seen. (B) A single, shaking red blood cell. A detector bead is trapped next to the cell and serves as a read-out of the microflow. (C) Three consecutive steps of a laser pattern of a line of NIR laser beams and an independent green laser beam ($\lambda = 532\,nm$). (D) Corresponding alignment of a trapped RBC and a $1.3\,\mu m$ detector bead as used for the cell shaking setup. Vertical (E) and horizontal (F) cell shaking of RBCs trapped with a line of three laser beams. (G) Vertical cell shaking experiment with a lung cancer cell.

Fluidic force spectra and flow field mapping

In accordance with the chosen shaking pattern as shown in Fig. 5.1, the cell displacement is in the order of µm and can easily be observed by eye through a microscope (Fig. 5.2A,B). Center-of-mass tracking routines [138, 216] allow for a measurement of the response of the cell on the spatiotemporal force field. To determine the force transmission through the fluid, in other words, cell-fluid coupling, the emerging microflow at the detector bead in a few µm distance is recorded. The measured quantity of a cell shaking experiment is thus the track of an optically trapped detector particle whose Brownian motion is affected by cell-fluid coupling.

Typically, the flow causes shifts of the detector particle of only a few tens of nm and cannot be distinguished from the thermal motion in the time trace of the flow detector (Fig. 5.2C). Due to the periodicity of the input signal, however, the magnitude of the Fast Fourier-transformed (FFT) detector time series reveals several characteristic sharp peaks that can be assigned to the external driving and allows for a very sensitive detection of the periodic fluidic forcing due to inherent noise elimination (Fig. 5.2D). For this reason, a discussion of the tracked data in frequency space is equal to band-pass filtering of the noisy time series. The obtained *fluidic force spectra* provide a characteristic fingerprint of the flow field dynamics at a certain detector position. Examples for FFT-transformed detector signals are shown in Fig. 5.2D–F[2]. Since any dynamics is usually overdamped in biological systems, the Fourier transformed input signal possesses peaks at the same frequencies as the measured fluidic spectrum S_{det}. The first peak (denoted as S_1 in the inset in Fig. 5.2D) in all frequency plots is associated with the shaking frequency. All further peaks are overtones that appear at integer multiples of the base frequency and characterize the shape of the local fluidic field during cell shaking in the frequency domain.

For a dipolar and thus, symmetric movement pattern (Fig. 5.2F), the odd Fourier modes 1, 3 and 5 are strongly pronounced independent of the detector position. The height of the first overtone indicates the relative flow field strength in the respective spatial direction (here: y-direction) [13]. The direction is thereby chosen with respect to the expected maximum signal strength, which is usually equivalent to the direction of the shaking pattern. For a more complex shaking pattern as presented in Fig. 5.2D and F, a strong variation of the measured Fourier peaks is observed, corresponding to the non-uniform flow field during optical shaking at different detector positions. Via a scan of the detector bead at different locations, the fluidic field around a shaken cell can be mapped, which demonstrates the potential and flexibility of the presented approach.

[2]Throughout the present chapter, the FFT signal will be given in arbitrary units as *FFT displacement*. In principle, for a known geometry of the moving object, a conversion to a force is possible for the Fourier-transformed time traces (see Section 2.4). Chapter 6 will be dedicated to force measurements using power spectral density analysis applied on spherical detectors.

In the following, the focus however lies on the description and measurement of the microflow for a fixed detector position in order to analyze the coupling between cell and surrounding fluid. It is clear that the fluidic spectrum measured in this case will depend on the input pattern, which has an effect on the emergence of Fourier modes or overtones. On the other hand, the observed spectrum will also change with respect to properties of the object which is shaken. Examples for such detectable physical quantities are the geometry of the cell, but also its mechanical stiffness. Both cause an alteration of the fluidic force spectra.

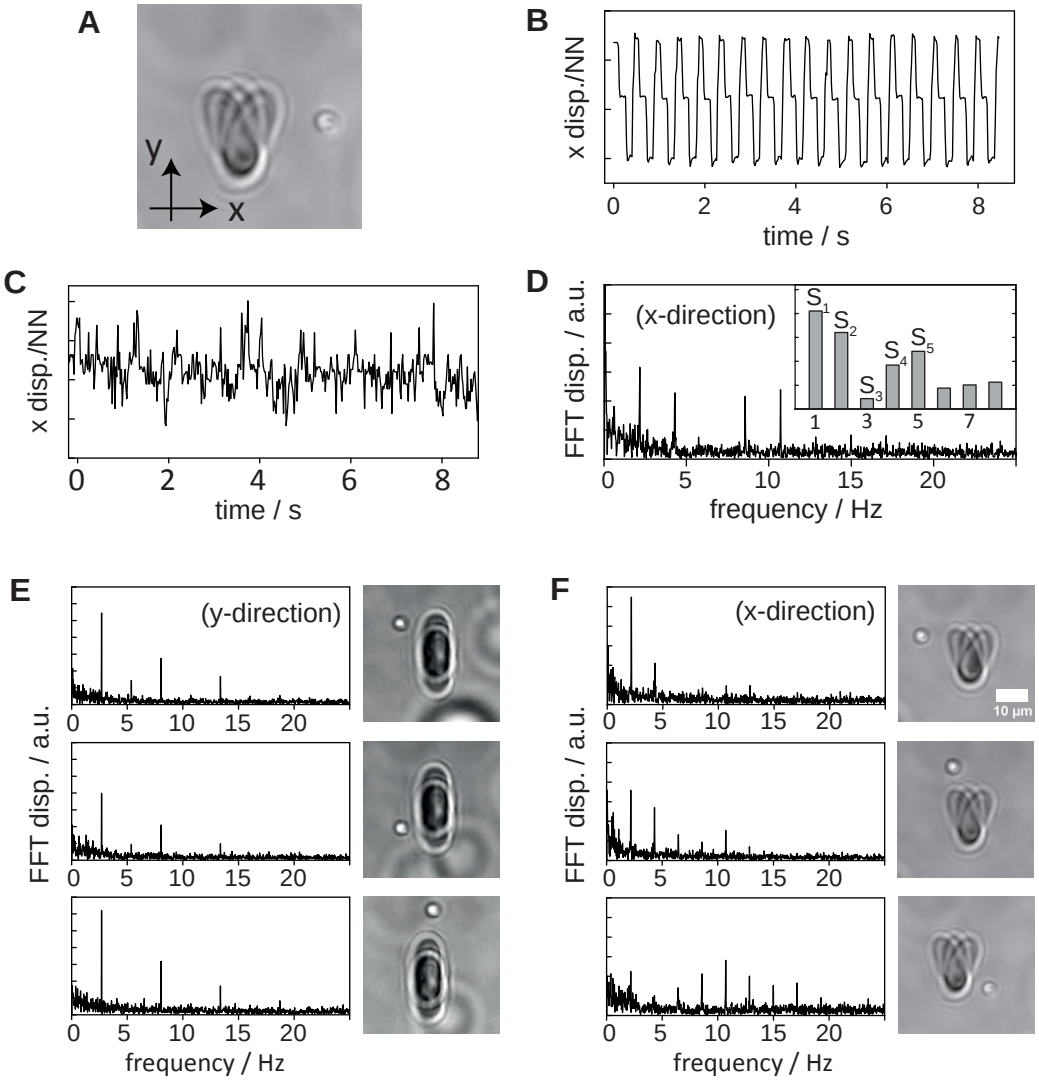

Figure 5.2 – Fluidic force spectra for different RBC shaking experiments. (A) Overlay of microscopy images of the cell movement. The three cell positions are defined by an array of optical traps as shown in Fig. 5.1C. Tracked time series of (B) the RBC movement and (C) the detector bead. (D) FFT displacement of the time series shown in C. The inset shows the signal heights S_i with respect to the first 8 Fourier modes. (E) and (F): Flow field mapping in the vicinity of a shaking RBC for two different shaking patterns. The experiments were done in a slightly hypotonic medium ($\eta_m = 0.15$) and the same cell was used throughout all measurements with the detector bead in different positions.

Signal processing model

From a *signal-processing* perspective, cell-fluid coupling spectroscopy can be described by the conversion of an input signal, defined as the temporal dynamics of the laser beam array, to an output signal, here the fluidic spectrum measured at the detector. During an experiment, the signal is converted from an optical to a mechanical signal and back, according to a signal *transduction*, then *filtered*, and finally *transmitted* through the fluidic environment. In this picture, the cell is seen as a mechanical filter applied for signal processing. Please note that the cell is an *analog filter*, while input and output are *digital* signals. This requires first a digital-analog conversion (DAC) from the programmed laser pattern to a physical signal whch can be done with an SLM, as well as an analog-digital conversion (ADC) of the cell movement accomplished by video recording the detector movement. Figure 5.3 summarizes the signal processing model of cell shaking.

For a mathematical description of the fluidic coupling process, the information contained in a fluidic spectrum as shown in Fig. 5.2D is summarized in a vector of the discrete absolute values S_n of the Fourier peaks of the order $n = 1, 2, 3, \ldots$ according to:

$$\mathbf{S}_{\text{det}} = (S_1, S_2, S_3, \ldots) \tag{5.1}$$

Above, the transition from a fluidic force spectrum (Fig. 5.2D) to a peak signal vector (inset) was already illustrated. The transition to a signal vector is equivalent to a removal of thermal noise from the Fourier modes describing the signal shape. Since the peaks $\mathbf{S}_{\text{det}}$ represent a fingerprint for each investigated cell, the Fourier spectra stand for the filter properties of a cell shaken with a known input sequence. Within this model, any cell property can be seen as an analog filter $\mathbf{f}_{\text{cell}}$ summing up to a collective filter by applying successive convolutions:

$$\mathbf{f}_{\text{cell}} = \mathbf{f}_{\text{cell}}^{(1)} * \mathbf{f}_{\text{cell}}^{(2)} * \mathbf{f}_{\text{cell}}^{(3)} * \ldots \tag{5.2}$$

The collective filter $\mathbf{f}_{\text{cell}}$ acts on the laser input signal $\mathbf{I}(t, x_0)$ given by the spatiotemporal variation of the optical field. The resulting signal is transmitted through the fluid which can be described by a spatial, and thus time-independent, filtering with $\mathbf{f}_{\text{trans}}$. If the position of the detector bead is not varied, the spatial dependency can be dropped ($x = x_0$). The entire process then reads

$$\mathbf{f}_{\text{trans}}(x_0) * \mathbf{f}_{\text{cell}}(t) * \mathbf{I}(t, x_0) = \mathbf{S}_{\text{det}}(t, x_0) \quad \text{and} \tag{5.3}$$

$$\mathbf{f}_{\text{trans}}(x_0) \cdot \hat{\mathbf{f}}_{\text{cell}}(\nu) \cdot \mathbf{I}(\nu) = \hat{\mathbf{S}}_{\text{det}}(\nu), \tag{5.4}$$

in time (t) and frequency (ν) domains, respectively. Equations (5.3) and (5.4) illustrate that for a known input signal, the filter properties $\mathbf{f}_{\text{cell}}$ can be derived by measuring the local, time- and space-dependent response $\mathbf{S}(t, x_0)$. From a signal processing point-of-view (see Fig. 5.3), the evaluation of Eq. (5.4) for the shaking frequency ν_1 and its overtones ν_i for $i > 1$ represents an ADC that provides the vector $\mathbf{S}_{\text{det}}(n)$ to the input signal by the application of several filter steps.

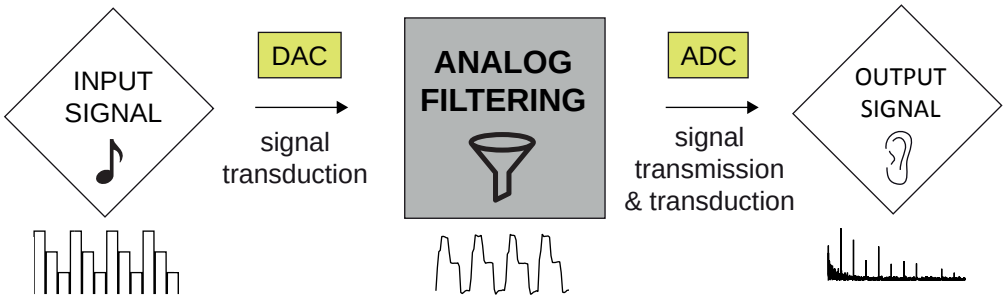

Figure 5.3 – Signal processing model of CFCS. In a signal processing model of fluid-coupling spectroscopy, the digital input signal is digital-analog converted (DAC), transduced and filtered by the cell, and finally transmitted through the fluid before it is digitized (ADC) by video recording the signal. The cell is seen as an analog filter.

Knowing this, one can make use of the fact that any difference in filtering will also have an impact on the detector signal $\hat{\mathbf{S}}_{\mathrm{det}}(\nu)$. Thus, not only the filter functions $\mathbf{f}_{\mathrm{cell}}(\nu)$ are characteristic for a certain set of parameters in a cell shaking experiment, but also the signals detected at a detector bead in the vicinity. In the next section, the recorded fluidic spectra will be used in order to distinguish cells by their mechanical (filter) properties. The general procedure is to compare the components S_i of $\hat{\mathbf{S}}_{\mathrm{det}}(\nu)$ for different cells with each other. This is equivalent to a comparison of the peaks in the Fourier spectra associated with the higher modes of the shaking frequency.

It is therefore important to understand the role of Fourier modes with respect to a periodic input pattern: While the first Fourier mode, S_1, represents the shaking frequency and its intensity reflects the detected strength, the higher Fourier modes $S_2, S_3, S_4, ...$ characterize the shape of the detected fluidic wave. This shape depends on the nature of the filters applied to the input function, and thus, on the mechanics of the shaken cells. If a mode is more pronounced, the respective superharmonic frequency appears stronger in the shape of the wave. As an example, the input function introduced in Fig. 5.1C is expected to show a strong 3$^{\mathrm{rd}}$ Fourier mode (and multiples of it), since every period possesses three identical steps. We will use this input function in the following section for cell shaking experiments (see Fig. 5.1D).

To further illustrate the principle, Fig. 5.4 shows how the shape of a signal, and thus the relative Fourier peak height, is influenced by the application of different filters. For simplicity, only consider two subsequent filter steps are considered that are a Gaussian filter and a sawtooth-shaped filter. Both filters are defined by their lengths σ and ρ at full width half maximum, respectively. Applying the Gaussian convolution kernel $\mathbf{f}_{\mathrm{smooth}}$ with widths σ on the input signal leads to a different degree of smoothing:

$$\mathbf{f}_{\mathrm{smooth}} * \mathbf{I}(t, \sigma) = \mathbf{S}(t, \sigma) \tag{5.5}$$

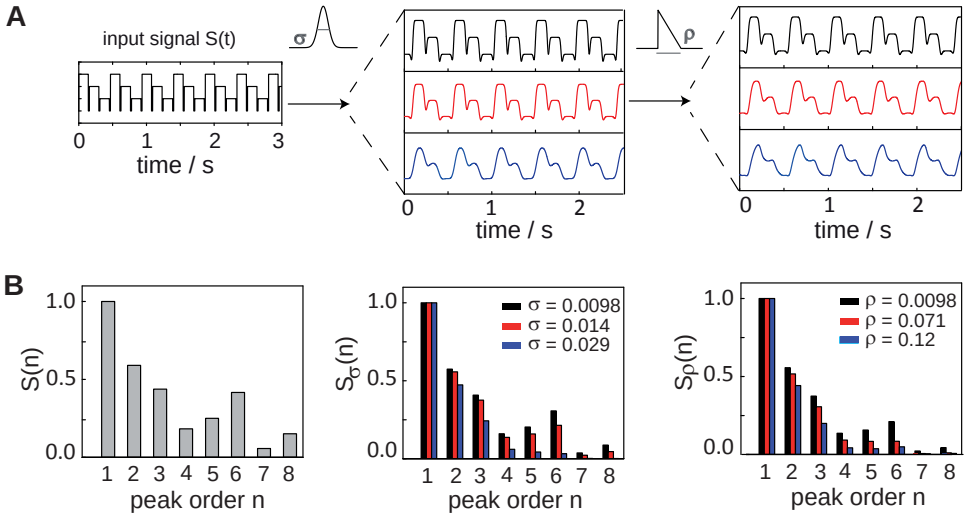

Figure 5.4 – Effect of digital filtering. Illustration of different filter kernels applied on an input function consisting of three steps. The filter strength varies with the width of the filter in time domain given by the parameters σ and ρ. (A) Resulting time domain plots after successive application of a Gaussian filter and a sawtooth filter on the input function. (B) Peak signal vector components corresponding to the filtering steps shown in A.

In the second step, asymmetric sawtooth filters $\mathbf{f}_{\text{saw}}$ of different widths ρ are applied on the signal smoothed with a Gaussian filter width of $\sigma_0 = 0.014$:

$$\mathbf{f}_{\text{saw}}(t, \rho) * \mathbf{f}_{\text{smooth}}(t, \sigma_0) * \mathbf{I}(t) = \mathbf{S}(t, \sigma_0, \rho) \tag{5.6}$$

Figure 5.4A clearly illustrates that filtering with different kernels has an effect on the signal shape depending on the filter strength. Each filter shows a characteristic response also on the Fourier spectra (Fig. 5.4B).

A quantification of such trends in the framework of filter theory would require remodeling of the filters needed to transform the input function to the measured shape by deconvolution operations. The individual peak trends for a given mode show a similar decreasing behavior for a change of the filter parameters, but follow different trends that stand for distinct aspects of the signal shape.

5.2 Distinguishing swelling states of RBCs

In the last section, the technique of cell-fluid coupling spectroscopy was established. We motivated that a fluidic force spectrum obtained from a single point detector is already sufficient to discriminate between individual cells. The microflow around single cells can be mapped on the dependency of different Fourier peaks. The method will now be applied to detect small differences between single cells. We choose human RBCs as a reliable and reproducible model system [216]. RBCs provide the advantages of relatively simple structure, a very narrow size distribution and well-investigated mechanical parameters [217–219].

RBC shaking experiment

RBCs were exposed to solutions of different tonicity to induce cell swelling and therefore a controllable and reproducible difference between the cells in each blood sample [220, 221]. Changing the salinity induces a change in tonicity and hence in cell stiffness and shape without the need of drug treatment or biochemical modification [220, 222]. Here, hypotonic media are compared by a hypotonic dilution parameter η_m, which stands for the relative ratio of water with respect to cell medium (PBS):

$$\eta_\mathrm{m} = \frac{V\,(\mathrm{H_2O})}{V\,(\mathrm{PBS})}.$$

Figure 5.5A shows dark field pictures of five representative cells in media with increasing η_m. Individual cells were trapped with a line of three laser traps as described before. To avoid photodamage, the power of the trapping laser was limited to 20 mW per beam and kept constant for all measurements. Due to the optical forces, the cell is slightly stretched and aligned to the laser array so that a reproducible configuration for all measured cells is achieved (Fig. 5.5B). Geometrical differences between increasingly hypotonic states of the RBCs could then easily be determined by measuring the aspect-ratio and revealed a swelling with increasing η_m (Fig. 5.5C).
To investigate cell-fluid coupling, the shaking pattern from Fig. 5.1C was chosen at a repetition rate of 2.14 Hz and cell shaking experiments were performed more than 10 times for each medium. During a cell shaking cycle (Fig. 5.5D), it was found that the cell shape was slightly altered. The part of the cell experiencing the largest displacement was seen to bend from the length symmetry axis with respect to the rest of the cell. To further investigate this observation, a *bending angle* was measured, as illustrated in Fig. 5.5E, for different hypotonic media and thus swelling states of the RBCs. As expected, swollen cells could be seen to bend less than the cells in isotonic medium (Fig. 5.5F). The measurement revealed a maximum bending angle for $\eta_\mathrm{m} = 0.15$ which does not coincide with the maximum aspect ratio of the same cells shown in Fig. 5.5C. This illustrates that mechanical properties may significantly differ from geometric properties.

In a rough approximation, RBC bending can be described by the *flexural rigidity* which is defined as the resistance offered by a non-rigid structure while undergoing bending. The flexural rigidity D_flex of a plate reads [223]

$$D_\mathrm{flex} = \frac{E h_e^3}{12\left(1-\nu_p^2\right)} \tag{5.7}$$

and depends on Young's modulus E, the Poisson ratio ν_p and the elastic thickness of the plate h_e. The dependencies of D_flex are both nonlinear and depend on each other. A change in aspect-ratio (Fig. 5.5), e.g., would strongly affect E and h_e, which explains the possibility of a non-monotonous dependence of the bending angle on an isolated parameter change as illustrated in Fig. 5.5E. The presence of the optical tweezer stretching the RBC in axial direction complicates the situation even further since it will vary with different cell

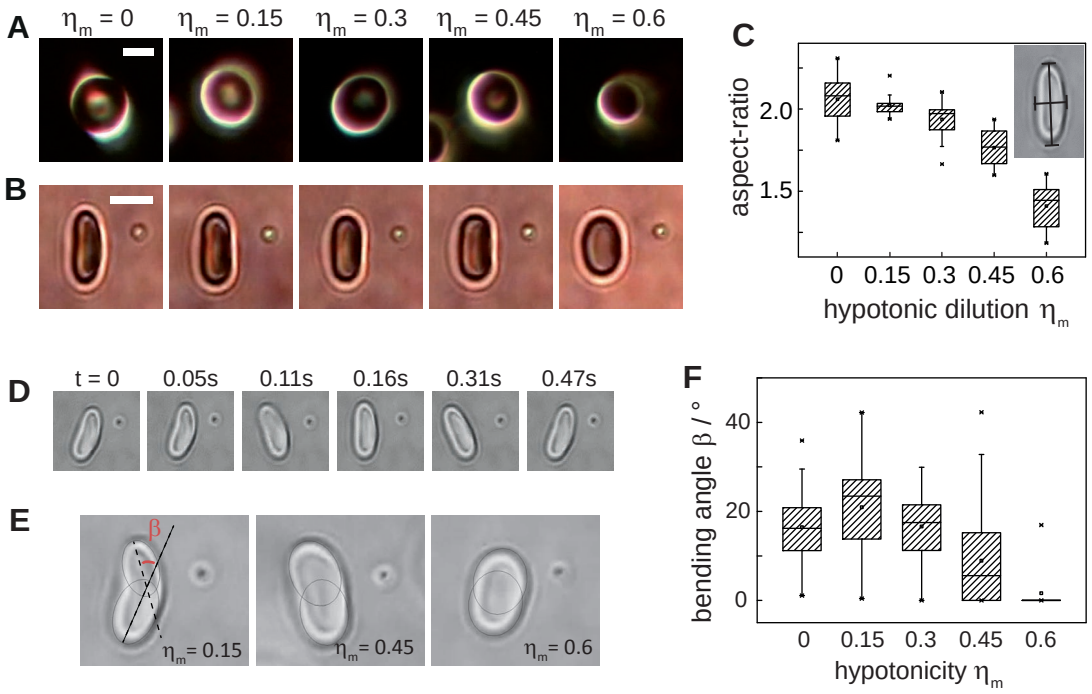

Figure 5.5 – Swelling and bending of RBC. η_m denotes the ratio of water to PBS. (A) Increasing η_m causes swelling of RBCs visible in dark-field microscopy. (B) Representative bright field images of RBCs for the same η_m in the experimental configuration. (C) Box plot of the aspect-ratio of RBCs in the configuration shown in B. (D) Snapshots over one period of shaking. (E) Maximum bending angles for representative RBCs of different hypotonicities η_m. A definition of the bending angle β is illustrated in red color. (F) Dependance of the bending angle β as defined in B on the hypotonic dilution η_m. The plots in (C) and (F) are based on a statistic of more than 200 cells, error bars denote the error of the mean.

geometry and stiffness and hence affect ν_p, which is the ratio of transverse to axial strain as experienced by the force field. Even though for an accurate modelling of the elastic cell properties these assumptions might well serve as a framework, for the moment, it is only important to realize that a set of different but entangled mechanical properties exist. These result in nonlinear and characteristic response curves as shown in Figs. 5.5C and 5.5F.

Cell-fluid coupling of RBCs

We applied CFCS to investigate whether differences in mechanical properties also have an effect on the microflow around the RBCs. To get a first idea, the center-of-mass of three individual cells were tracked in different hypotonic media (Fig. 5.6A) during the cell shaking experiment illustrated in Fig. 5.1C. For simplicity, only one spatial direction, here the x-direction, is considered. It is evident that the periodic signal appears rounder for the recorded center-of-mass movement of the more isotonic, and thus softer, cell. This trend is reproducible when repeated with cells in the same medium.

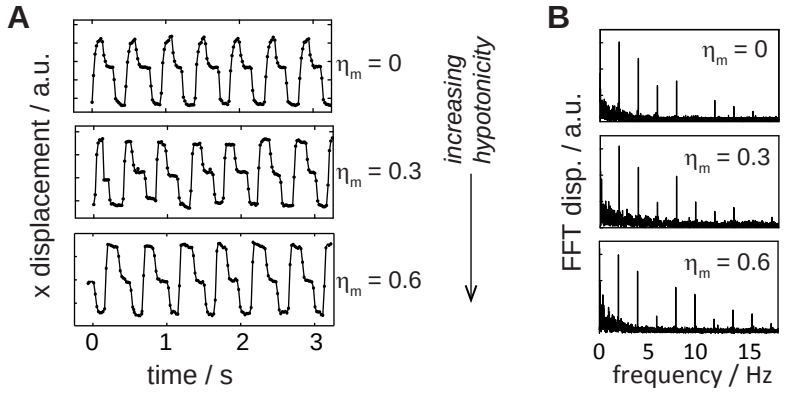

Figure 5.6 – **Cell-fluid coupling**. Comparison of (A) center-of-mass tracks of shaking RBCs and (B) recorded fluidic force spectra for RBC media of different hypotonicity for the cell shaking experiment illustrated in Fig. 5.1D.

The flow field measured at the position of the detector bead was then compared to the respective center-of-mass track (Fig. 5.6). In the spectra, it is already possible to recognize trends such as a decrease of the 3$^{\text{rd}}$ order Fourier peak or an increase of the 6$^{\text{th}}$ mode, each with respect to the 1$^{\text{st}}$ Fourier peak, as discussed in the last part of the previous section. The idea of the normalization to the ground mode is to exclude the strength of the force field for a characterization of the cells. Instead, the relative height of the Fourier peaks will be compared that are related to the signal shape of the spatiotemporal flow. The flow pattern is supposed to be sensitive to changes in cell stiffness.

To further confirm the trends in Fig. 5.6B, CFCS measurements were repeated with a larger statistics of five different hypotonic media and more than ten cells per medium. We found that the fluidic spectra were highly reproducible and characteristic for each medium since the data was distributed in a very narrow range. Figure 5.7A shows the average Fourier peak values $\overline{\mathbf{S}_{\eta_\mathrm{m}}}(n)$ vs. the corresponding Fourier peak order n for different η_m:

$$\overline{\mathbf{S}_{\eta_\mathrm{m}}}(n) = \frac{1}{\mathbf{S}_0(1)} \cdot \sum_N \mathrm{S}_{\eta_\mathrm{m}}(n) \tag{5.8}$$

The average Fourier peaks are derived from single detector spectra from a large statistics of N cells exposed to an increasing dilution parameter. They are normalized to the average value of the first order Fourier peak in isotonic medium $\mathbf{S}_0(1)$. By comparing the detector bead data for each Fourier peak order separately, it was found that in general, the amplitude trends $\mathbf{S}_{\eta_\mathrm{m}}(n)$ decrease for higher values of η_m. The significance of these trends already allows distinguishing different hypotonic states of erythrocytes by fluidic readout. This observation demonstrates that variances in cell shape or deformability as induced by cell swelling here lead to a measurable change of the hydrodynamic environment.

We now consider the ratio of specific Fourier peaks for a signal strength-independent evaluation. Figure 5.7B and C shows two examples of Fourier peak ratio dependencies $\mathbf{S}_{\eta_\mathrm{m}}(n)/\mathbf{S}_{\eta_\mathrm{m}}(m)$ on the hypotonic dilution η_m. To illustrate possible trends, the ratio of the 3$^{\text{rd}}$ ($m = 3$) and the 6$^{\text{th}}$ ($m = 6$) order to the first three possible Fourier orders

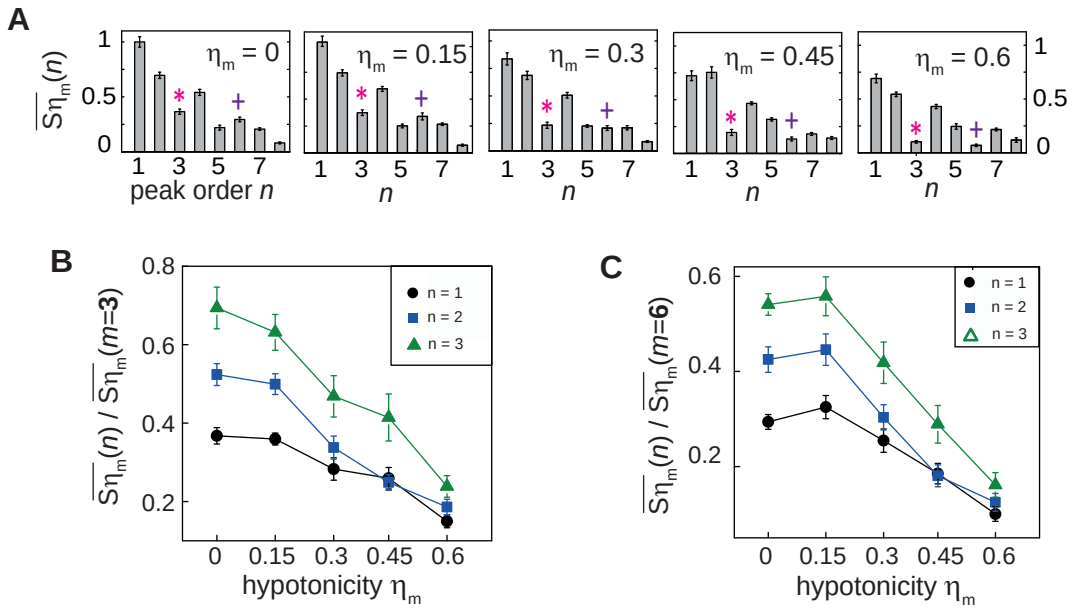

Figure 5.7 – Trends of average fluidic spectra. (A) Average fluidic spectra for different hypotonic dilution values η_m as defined in Eq. (5.8). For each average spectrum, more than ten measurements of single cells in the respective media were considered. The 3$^{\mathrm{rd}}$ and the 6$^{\mathrm{th}}$ Fourier peak are marked with symbols (*,+). The ratio of the 3$^{\mathrm{rd}}$ (B) and the 6$^{\mathrm{th}}$ (C) Fourier peak to a choice of other Fourier peak modes of the respective spectrum are shown as a function of the hypotonicity of the medium η_m.

($m = 1, 2, 4$) were chosen. As discussed before, these modes were chosen due to the specific shape of the shaking sequence: since there are three 'substeps' within one oscillation period, the superharmonic modes divisible by three are affected in a similar way. The ratio of $S_{\eta_\mathrm{m}}(3)$ and $S_{\eta_\mathrm{m}}(6)$ to the ground mode $S_{\eta_\mathrm{m}}(1)$ reflects how pronounced one substep is relative to the overall oscillation. As can be seen in Fig. 5.7, both peaks show a similar trend and are decaying for larger η_m, with the exception of the 6$^{\mathrm{th}}$ order peak that shows a maximum for $S_{\eta_\mathrm{m}}(6)/S_{\eta_\mathrm{m}}(1)$ for $\eta_\mathrm{m} = 0.15$. Interestingly, these trends appear as well in the ratios to higher Fourier modes $n = 2$ and $n = 4$, confirming the importance of Fourier modes 3 and 6.

Comparing the discussed trends in Fig. 5.7B and C to the aspect-ratio and bending angle plots of RBCs (Figs. 5.5C and F), a strong similarity becomes obvious. The fact that the trends match each other indicates that Fourier peaks can indeed be used as a measure for mechanical cell properties such as size or stiffness. As mentioned before, an actual modelling would however require a very detailled description of all parameters and a better understanding of the roles of the respective Fourier modes.

In summary, CFCS is capable of distinguishing RBCs in suspension based on their distinct fluidic spectrum measured at an arbitrary point in the vicinity. The results illustrate that a variation of cell shape or stiffness results in a characteristic difference in the flow around these cells, which can be detected by CFCS.

5.3 Dynamical mechanical analysis of single cells

While RBCs represent a very reproducible model system, variations in size or shape can no longer be neglected for more complex objects such as most eucaryotic cells. Consequently, an extension of the experimental strategy becomes necessary. In the last section, see e.g. Fig. 5.6, it was motivated that in a cell shaking experiment both cell movement and fluidic response measured at the detector bead can serve as a means to distinguish mechanical parameters of the shaken cell. So far, these experiments were restricted to a single frequency. This frequency was chosen somewhat arbitrary, only matching the technical constraints such as image acquisition frequency and time. A mechanical *response curve* has the potential to provide a more detailed picture of cell mechanics and can be obtained by sweeping the frequency in a defined range. This approach is similar to a *mechanical dynamical analysis* [224], which is a technique for the characterization of soft materials in terms of dynamic moduli. Here, I suggest an experimental strategy of how the cell shaking experiment introduced in the previous section could be extended to a setup for dynamical mechanical analysis on a single cell level. To demonstrate the feasability of the strategy, two different applications are presented. First, the focus lies on the role of the medium and how a change in viscosity alters the results. Second, the response of cancer cells is investigated.

Detection of changes in viscosity

In cell-fluid coupling, obviously, the properties of the fluid environment play a significant role. To illustrate this, the viscosity of the standard RBC medium was increased by adding 26 mg/mL Polyethylenglycol (PEG, 20 000 g/mol). The CFCS experiments described in Section 5.1 were performed on single RBCs with increasing frequencies and the same number of oscillations, each. For these experiments, a scientific camera was synchronized to the input oscillation and an automatized frequency sweep was designed (see Section 3.1). A sketch of the procedure and an illustration of the input function applied on a single RBC are shown in Fig. 5.8A.

With a statistics of only four individual RBCs, frequency sweeps were performed in both media (RBC medium and PEG medium). Figure 5.8B shows the average fluidic force spectra of the track of the cell movement that reveal significant differences in the amplitude trends. While the 1$^{\text{st}}$ Fourier mode, which is roughly proportional to the cell displacement for the simple input function used, is similar for both viscosities, higher Fourier modes are clearly suppressed in PEG medium. This finding suggests that for a higher viscosity, the cell movement is more sinusoidal and thus follows the input function more closely. The *overdamped* Langevin equation (2.16) with Eq. (2.3) reveals for the velocity $\dot{x}$ of the RBC that

$$\dot{x}\,(t) \;\propto\; \frac{F_{\text{ext}}\,(t)}{d \cdot \eta}, \tag{5.9}$$

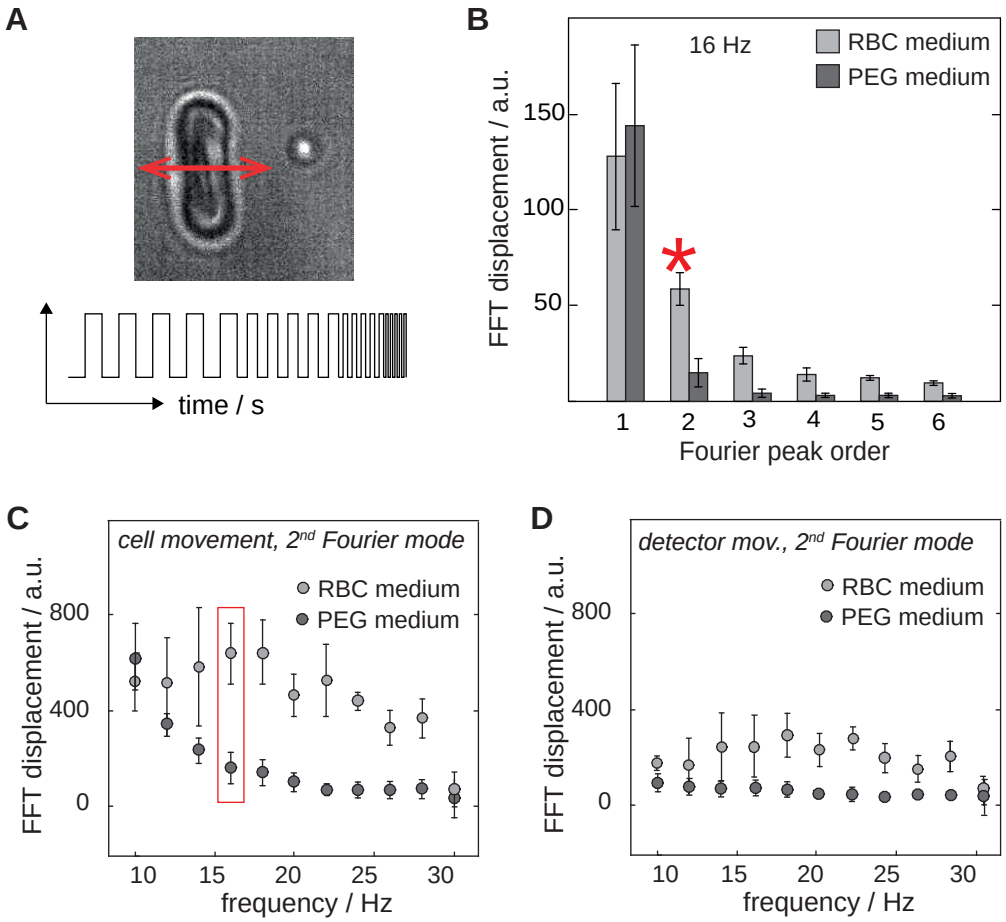

Figure 5.8 – Local viscosimetry using RBC shaking. (A) RBCs are shaken using a simple two-step pattern moving in horizontal direction (see red arrow) at increasing frequencies. (B) Averaged Fourier peaks in media with different viscosity (RBC and PEG medium) for a statistics of 4 RBCs at a shaking frequency of 16 Hz. (C) Trends of the 2$^{\text{nd}}$ Fourier mode (marked by * in B) of the cellular displacement pattern for different frequencies. The box indicates the data set plotted in B. (D) Corresponding measurement at the SiO_2 detector bead.

where $F_{\text{ext}}(t)$ includes all external forces dominated by the input force field and d denotes the diameter of the red blood cell. Consequently, a higher viscosity causes a smaller change rate in the movement $\dot{x}$, which explains the stronger decrease of higher Fourier modes for the PEG medium (see Fig. 5.8). In this way, Eq. (5.9) already allows the use of single cell shaking experiments to compare local viscosities for a fixed frequency. For a quantitative measurement, however, the external force as well as the expression for the drag force, γ, would have to be further refined.[3]

A higher statistics and thus higher accuracy of the results can be obtained by frequency sweeping. In Fig. 5.8C, the frequency sweep corresponding to the 2$^{\text{nd}}$ Fourier mode is shown as an example. We pick this mode as it is the first overtone above the ground mode

[3] In Section 6.2, such a quantification will be made for a spherical gold nanoparticle pushed by a simple step-force. In this case, the Langevin equation can be solved analytically.

and thus related to the shape of the tracked signal rather than to the signal strength. The movement in PEG medium shows less statistical variation and a smaller displacement and thus a smoother curve progression. This fits the expectations since PEG has a higher vicosity and with it, a higher drag coefficient η, compared to RBC medium. With this, Eq. 5.9 hence clearly predicts a smaller position change rate (or velocity) of the shaken RBC.

We recognize that in our setup, all shaking frequencies between 16 Hz and 28 Hz could be used for a distinction of differently viscous media. The same is true for measurements at the detector bead (CFCS measurements, Fig. 5.8D). Since the detector bead is spherical with a radius r, its velocity follows Stokes' law:

$$\dot{x}(t) = \frac{F_{\text{ext}}(t)}{6\pi r \cdot \eta} \tag{5.10}$$

Still, the exact form of the cell's response on the input function should be known for a quantitative determination of local viscosities. The use of a detector bead ensures a spatial resolution in the order of the detector radius (here: µm), which could be further decreased by using appropriate detectors such as gold nanoparticles (see Chapter 6).

Frequency sweeps of cancer cells

CFCS can also be applied to larger cells, such as eucaryotic cancer cells. We have already motivated that frequency sweeps provide a higher statistics and thus a better accuracy of the results, which becomes especially important if the shape reproducibility of the shaken cells cannot be guaranteed. In the following, the two widely used lung cancer cell lines A549 and H2030[4] are compared. A549 possesses a higher metastatic activity and thus, a higher degree of malignancy [225]. Since the latter is believed to have an impact on the mechanical properties of cells [213, 226], a mechanical frequency sweep might be able to distinguish between cancer cells of different malignancy.

We used the same experimental setup and procedure as for the described frequency sweeps of RBCs and increased the number of focused laser beams to 5 for a more stable confinement of the position of the larger cells. The cancer cells were shaken at different frequencies applying a simple up-down movement of the laser array (cf. Fig. 5.1G). Figure 5.9 shows the resulting average fluidic spectra for the measurement of two different cancer cell lines at a shaking frequency of 2.14 Hz. The average spectra are clearly distinct, especially regarding the first two even (2^{nd} and 4^{th}) Fourier modes. For an interpretation of these results, one could argue in the following way: The input function consists of symmetric force steps and thus possesses odd Fourier contributions only. The response in cell movement will however be smoother and also slightly delayed, depending on the viscous environment but also on the rigidity of the cell. This causes the emergence of even Fourier modes and represents a filtering of the input function by the cell seen in the framework of signal processing (cf. Section 5.1). In this way, as the even Fourier modes are stronger in

[4] Cell culture was done in cooperation with I. Fernandez in the group of Prof. Eickelberg (LMU Munich).

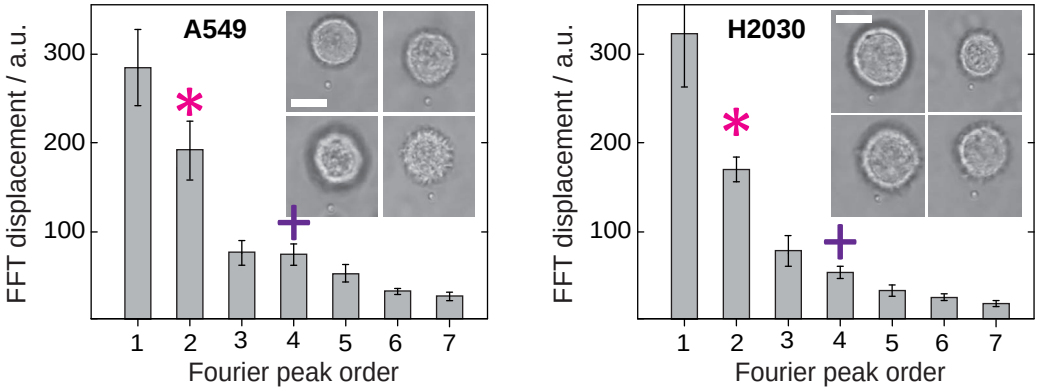

Figure 5.9 – Fluidic spectra of lung cancer cells. CFCS measurements were performed on two different lung cancer cell lines (A549 and H2030). The cell shaking frequency was 2.14 Hz and the input function was a simple dipolar up-and-down movement of the laser array. The latter consisted of five NIR beams to provide a stable experimental configuration. The 2^{nd} (*) and 4^{th} (+) Fourier modes are indicated.

case of A549, these cells can be assumed to be softer than H2030 cells. A correlation of cell stiffness and metastatic potential can nowadays be seen as established [212, 227–229]. The results shown here demonstrate that mechanical properties might result in changes of shear flow around cancer cells which may influence cell-cell interactions and processes as metastasis (see following section). However, more experiments would be required for a confirmation of these findings.

Next, a frequency sweep of the up-down movement of the two cancer cell lines was performed to gain insight into cell-fluid coupling. For comparison and to monitor how the input signal is transferred from its original state to the final reception at the detector bead, both cell movement (Fig. 5.10A) and silica bead displacement (Figure 5.10B) are tracked for all applied frequencies. In Fig. 5.10A and B, examples for an input frequency of 18 Hz are given. In this case, periodic averaging with respect to the input period length reveals an average cell displacement of 0.5 µm resulting in a perturbation of the detector bead of only 40 nm after a transmission of the mechanical signal through the fluid. With increasing frequencies, the cell displacement decreases and becomes more sinusoidal (Fig. 5.10C). For the detector bead displacement, potential changes in strength or shape of the detected signal could not be resolved (Fig. 5.10D).

A plot of the signal strength for both cell and detector displacements versus the frequency of the oscillation for both cell lines is shown in Fig. 5.10E, F. Again, the average displacement of the cell is proportional to the 1^{st} Fourier mode of its tracked movement. For both cell lines, cell displacement decreases for increasing frequencies. No significant difference can be detected between A549 and H2030. Interestingly, comparing the frequency dependent detector bead displacements (Figure 5.10F), the data associated with the A549 cell line shows clearly higher values compared to the H2030 measurement. Certainly, a higher statistics, control measurements and frequent repetition would be necessary

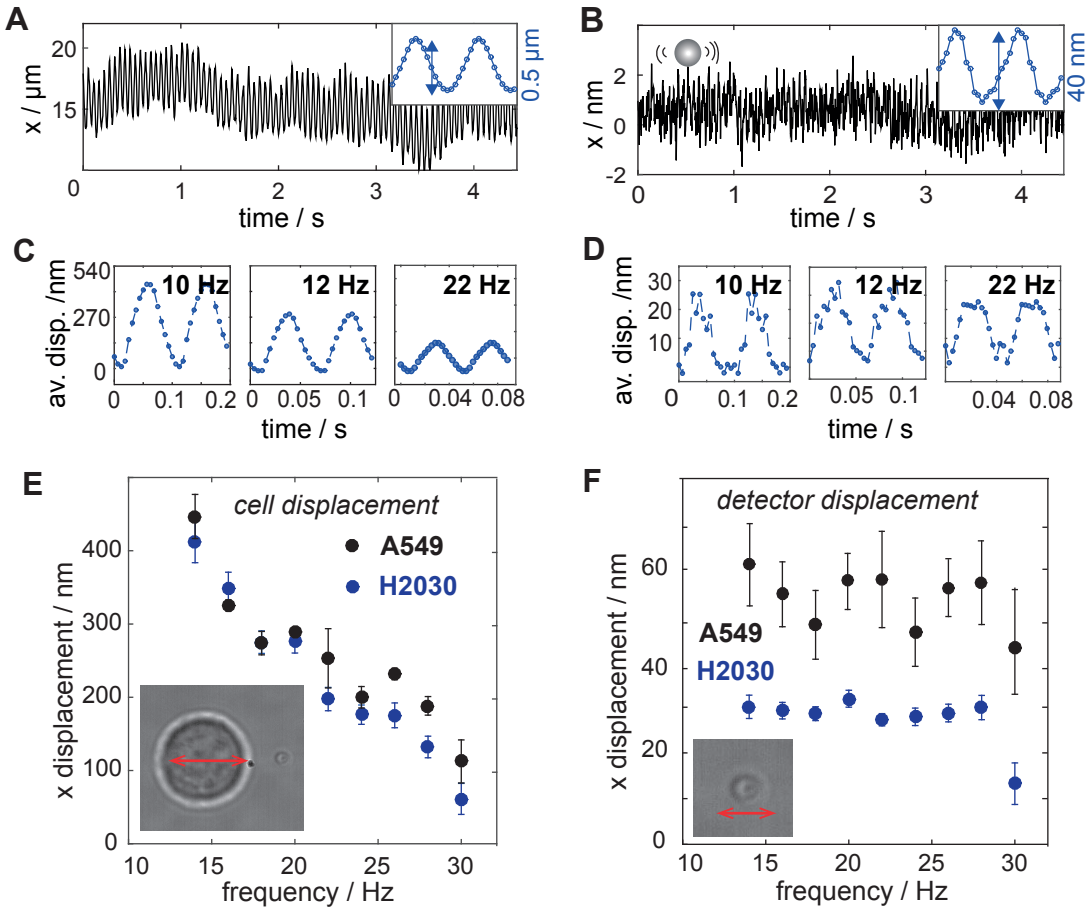

Figure 5.10 – Frequency sweeps of cancer cells. Tracks of cancer cell movement (A) and detector bead displacement (B) in x-direction. The insets show a periodic average of the tracks revealing an average displacement of 0.5 µm and 40 nm, respectively. (C) Periodic averages of cell movement for three different frequencies. (D) Periodic averages of detector bead movement for three different frequencies. (E) Frequency sweep of the 1st order Fourier mode does not reveal significant differences. (F) Frequency dependence of the detector bead displacement.

to prove the statistical relevance of the observation [230, 231]. However, the differences in the signal detected at the trapped microbead could be interpreted in a way that small differences in cell mechanics or geometry might indeed be picked up by an appropriately positioned detector bead. This would enable a reliable classification of cell stiffness on a single cell level.

5.4 *Discussion:* Cell-fluid coupling in biomechanics

We used an optically trapped particle to measure the microflow around a shaking cell. Analyzing both the trace of the cell and the detector bead in Fourier space provides information about the cell's reaction on optomechanical stimulation and the transduction of the cell's motion through the fluid. Measurements of red blood cells exposed to different hypotonic media showed that different cellular edematous states result in a specific fluidic pattern around these cells. We motivated that this principle can be used to disentangle different mechano-biological features in the Fourier space by seeing them as independent analog filters. In a variation of the cell shaking technique, a frequency sweep was applied to lung cancer cells and for viscosity detection. These proof-of-principle experiments are the first step towards a noninvasive dynamical mechanical analysis on the single cell level with a fluidic readout.

The growing interest in the field of mechanobiology [154] has given rise to the development of a large number of measurement techniques at the single cell level [106, 232]. As illustrated in Fig. 5.11, existing approaches can in general be divided into *local* approaches (Fig. 5.11A), and *global* approaches (Fig. 5.11B) [232]. Many techniques still lack sensitivity and feasability in practical applications [4]. Most techniques require mechanical contact to probe the cell. In this context, CFCS is a novel, all-optical *remote sensing* technique for force sensing around single cells. It allows for both, a global read-out by tracking the movement of the entire cell and a local force measurement in the vicinity of the cell, using a detector bead (cf. Section 5.2, Fig. 5.6).

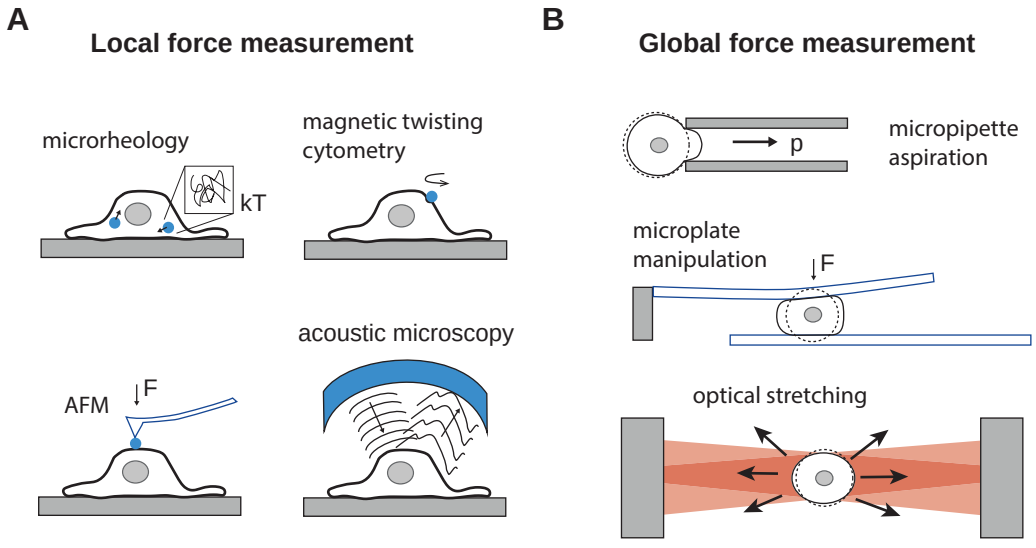

Figure 5.11 – Global and local force measurement techniques, modified from Ref. [232]. Techniques to measure local (A) and global (B) mechanical properties of individual cells.

The quick and reliable classification of cells in suspension is an important issue for diagnostics and medical care [233, 234]. Strategies to distinguish healthy from malignant cells, for example, range from biochemical fluorescent labeling [235], Raman spectroscopy [236], coherent diffraction imaging [237], optical tweezer techniques [226] and photoacoustic flow cytometry [238] to microfluidic approaches [239]. Optical techniques mostly provide information about biochemical differences between cells, such as the molecular composition of the cell membrane [240] or protein expression levels [241]. In recent years, however, many examples in the literature have shown that cells can also be reliably distinguished based on their physical properties such as stiffness and shape [232, 242–244].

CFCS is a both contactless and label-free technique. Hence, it holds the potential to complement existing strategies in cell diagnostics as it is based on the detection of mechanical parameters. In Section 5.2, I demonstrated that even small differences in mechanical properties can be resolved as a mechanical fingerprint based on a very low number of cells (cf. e.g. Section 5.3, Fig. 5.9). In future research, a closer investigation of parameter trends with appropriate filters could account for a detailed model linking viscoelastic properties of a cell to the fluidic response at the location of a detector bead.

In difference to the other techniques (cf. Fig. 5.11), **CFCS provides the means to analyze the impact on the fluidic coupling caused by shear flow.** The notion that cells sense, interact with and respond to the stiffness of substrates has been reported by several groups [18, 19, 246]. A similar role of cell-fluid interaction is less investigated, but cannot be neglected. These interactions might be highly important for biological functions that involve either more than one cell, such as wound healing, or communication of single cells through the fluid, in general. The latter is relevant for the metastasic process

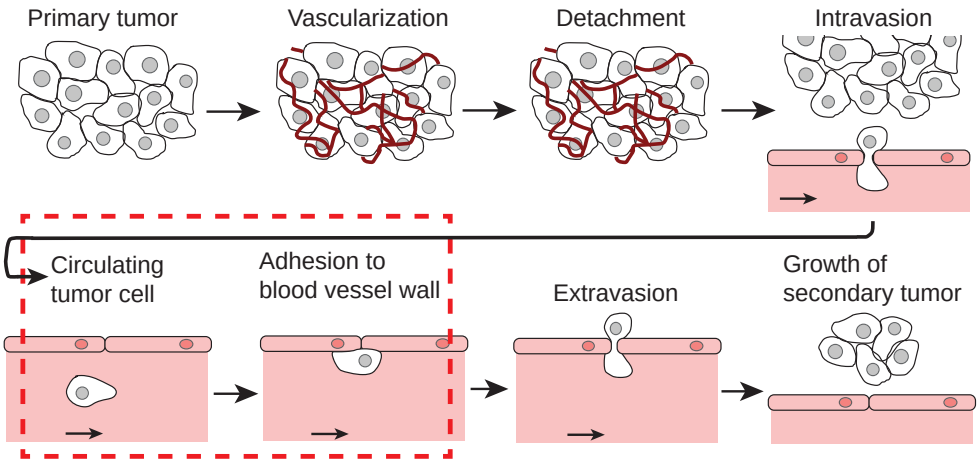

Figure 5.12 – Metastatic process. Cells detach from a primary vascularized tumor, penetrate the surrounding tissue, enter nearby blood vessels and circulate in the vascular system. Some of these cells eventually adhere to blood vessel walls and are able to migrate into the local tissue, where they can form a secondary tumor. The step which is assumed to be most relevant in cell-fluid coupling is indicated by a dashed red frame (image adapted from Wirtz *et al.* [245]).

(Fig. 5.12, [245]). Yet, it remains an unanswered question what the interplay of chemical and mechanical signaling during metastasis might look like. Presumably, for the settlement of circulating tumor cells to a vessel, shear flow plays an important role. By means of different biophysical assays it has already been shown that cells behave differently under flow depending on their mechanical properties [154, 247]. If the exact process were known, one could aim for the alteration of certain mechanical properties such as the membrane stiffness with special drugs to prevent cancer progression.

It may sound trivial that differences in cell shape, stiffness or deformability are likely to have an effect on the hydrodynamic coupling between cells and their environment. On a single cell level, however, only little is known about the impact of such a forcing. On the other hand, for bacteria, fluid-mediated coupling was already shown to be an important factor for guiding swarm behavior and biofilm formation [247–249]. Eucaryotic cells *in vivo* are constantly exposed to a periodic stimulation in the low Hz to mHz regime such as breathing or heart beat [13, 250, 251]. However, for fluidic coupling experiments, the challenge must be faced that relevant forces are often much smaller than thermal forces. An approach to address this challenge is introduced in the next chapter.

Chapter 6

Optofluidic Force Measurement with Optically Trapped Particles

The smallest ever measured force, $24\,\mathrm{yN} = 24 \times 10^{-24}\,\mathrm{N}$, was applied on a cloud of ultracold rubidium atoms in an optical cavity under ultracold and vacuum conditions [252]. The resulting force sensitivity is only four times worse than the theoretical limit given by Heisenberg uncertainty principle. However, at the mesoscale (see Introduction), where objects are diffraction-limited and forces are hidden by thermal noise, it is impossible to achieve such a low resolution. Motivated by the emerging field of *photonic force microscopy* [6], sophisticated vehicles [253–255] were fabricated to guarantee the highest possible sensitivity of nanotips. Using these for force detection enabled a resolution of a few hundreds of fN in resolution.

In this chapter, a different approach is proposed that relies on the post-elimination of thermal noise [108, 256] by periodic averaging of the recorded time series rather than improving the sensitivity of the instrument [257, 258]. The first section introduces the basic working principle: Sub-Brownian forces are measured by using an optically trapped detector particle that is pushed in a periodic fashion[1]. To demonstrate the applicability of the method, it was applied for deriving quantitative values in different systems that are presented in the second and the third section[2]. For a measurement of the scattering force on gold nanoparticles, a resolution of less than 3 fN is obtained. This is an order of magnitude smaller than any measurement of switchable forces performed on nanoparticles in solution with single beam optical tweezers to date. Next, a spatially extended microflow was considered around both an artificial microswimmer and a flagellated bacterium. To conclude, the application of fN-sensitive force measurements in biological systems is discussed.

[1] A corresponding article entitled "Pushing nanoparticles with light — A femtonewton resolved measurement of optical scattering forces" by C. Zensen, N. Villadsen, F. Winterer, S.R. Keiding, and T. Lohmüller, was published in *Advanced Science* in 2016 [259].

[2] For a comparison of micro-screws to bacteria, previously published data recorded by Kirchner *et al.* [11] were revisited to obtain a measured force.

6.1 Principle of fN-resolved force measurements

Ultrasensitive force measurements in a fluidic environment are based on a thorough analysis of the fluctuating movement of a point-like detector. The latter is represented by a small spherical bead trapped with an optical tweezer in a defined position. In this way, it is able to pick up even small vibrations and hence acts as a microphone at subpixel-resolution. For using metal nanoparticles as optofluidic detectors, the technique was previously named *nanoear* [10].

An optically trapped particle in a liquid environment exposed to an additional external force can be described by the Langevin equation, Eq. (2.16), extended with an external driving term $F_{\mathrm{ext}}(t)$,

$$m\ddot{x}(t) + \kappa x(t) + \gamma\dot{x}(t) = \xi(t) + F_{\mathrm{ext}}(t), \tag{6.1}$$

where $\xi(t)$ stands for thermal forces and m, κ, γ represent particle mass, trap stiffness and drag coefficient, respectively. For reasons of simplicity, a one-dimensional description is considered. A sketch of the forces acting on the particle is given in Fig. 6.1A, illustrating that the presence of a force results in a displacement of the particle. Equation (6.1) is in principle valid for all magnitudes of external forces. Here, investigations focus on the resolution of external force fields whose temporal average on the time scale of the measurement is smaller than the thermal forces:

$$\langle F_{\mathrm{ext}}(t)\rangle \ll \langle \xi(t)\rangle \tag{6.2}$$

In detail, the particle's position standard deviation due to Brownian motion is considered to be much larger than the displacement due to a single push by $F_{\mathrm{ext}}(t)$. Hence, the effects of $F_{\mathrm{ext}}(t)$ cannot directly be seen in the time trace as it will be overwhelmed by thermal fluctuations. A strategy to resolve forces fulfilling Eq. (6.2) is the application of a periodic repetition of the force stimulus. Therefore, $F_{\mathrm{ext}}(t)$ has to be switchable. In terms of a *lock-in approach*, Brownian noise can then be bypassed.

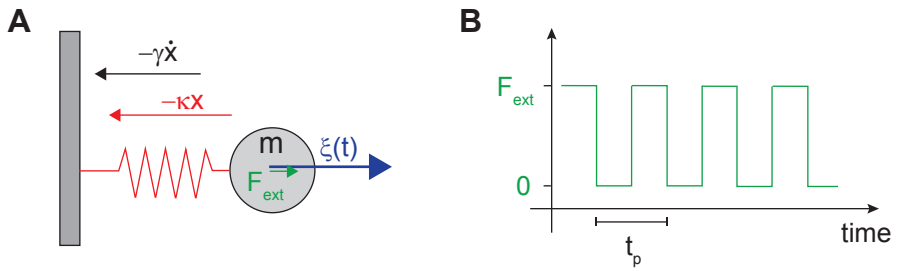

Figure 6.1 – One-dimensional model of particle movement described by the Langevin equation. (A) Sketch of the forces acting on a spherical particle of mass m following the Langevin equation (6.1) in presence of a harmonic potential of strength κ and viscous drag η. The thermal forces $\xi(t)$ are significantly larger than a single push of $F_{\mathrm{ext}}(t)$. (B) Temporal force profile of $F_{\mathrm{ext}}(t)$ according to Eq. (6.3).

In principle, any arbitrary periodic force profile could be used. However, for the present proof-of-principle study and to allow for an analytical study, a force profile of step-like shape $F_{\mathrm{ext}}(t)$ is considered that is switched between a force plateau F_{ext} and zero force in a periodic fashion (Fig. 6.1B). Its time series can be modelled using the Heaviside step function, H,

$$F_{\mathrm{ext}}(t) = F_{\mathrm{ext}} \cdot \sum_{0}^{k=N-1} \left[H\left(t - kt_{\mathrm{p}}\right) - H\left(t - kt_{\mathrm{p}} - \frac{t_{\mathrm{p}}}{2}\right) \right] \tag{6.3}$$

with $N = \frac{t_{\mathrm{m}}}{t_{\mathrm{p}}}$ being the number of repetitions of force steps, t_{m} the total measurement time, and t_{p} the period of the force step. An analytic solution of Eq. (6.1) with Eq. (6.3) can be given either in real space or in the Fourier domain.

Periodic averaging

To obtain a force from the displacement of a particle in a harmonic potential with a Gaussian position distribution, the displacement must be multiplied with a 'spring' constant, κ. The force resolution is then a result of the trap stiffness and the imaging resolution, here given by the standard deviation of the position distribution,

$$\Delta F = \kappa \cdot \sigma, \tag{6.4}$$

when neglecting the uncertainty in the trapping constant $\Delta\kappa$. If a mechanical stimulus is repeated periodically, its resolution is no longer limited by the standard deviation of the position distribution. It is rather limited by the *averaged* standard deviation, $\sigma_{\mathrm{avg}} = \frac{\sigma}{\sqrt{N}}$, with N, the number of repetitions. The averaged standard deviation corresponds to averaged position data and provides a minimal force sensitivity of

$$\Delta F = \sigma_{\mathrm{avg}}\kappa = \sqrt{\frac{k_B T \kappa}{N}}. \tag{6.5}$$

In the last step, the conversion of κ and σ via Eq. (4.4) was used. Hence, sub-Brownian forces can be resolved by increasing the number of repetitions of a single force pulse. Following the same line of argumentation, by averaging a tracked time series with respect to the repetition period of the external force profile $F_{\mathrm{ext}}(t)$, the spatial displacement is revealed with subpixel resolution.

Power spectral force measurement

Periodic averaging is a simple and intuitive method to reveal periodic patterns in a noisy time series. One drawback is, however, that it relies on seeing the movement of the particle as a mass-on-a-spring problem. It is hence not suitable for more complex or nonlinear dynamics. As an alternative, Eq. (6.1) with the external force given by Eq. (6.3) can be solved analytically in the Fourier space. In Section 2.2, the Langevin equation was solved for appropriate conditions in the Fourier space resulting in Eq. (2.50). The corresponding

expression for the power spectral density (PSD) in one spatial direction, $\langle S(f)\rangle$, was given by Eq. (2.22):

$$\langle S(f)\rangle = \frac{k_B T}{2\pi^2\gamma\cdot(f^2+f_c^2)} + \frac{\left\langle \hat{F}_{\mathrm{ext}}(f)^2\right\rangle}{t_{\mathrm{m}}(2\pi\gamma)^2\cdot(f^2+f_c^2)} \tag{6.6}$$

Here, $f_c = \frac{\kappa}{2\pi\gamma}$ is the corner frequency corresponding to the trap constant κ. Importantly, this equation holds for external forces of arbitrary shape. In the next step, the square of the expectation value of the Fourier transform of the step-function, Eq. 6.3, is calculated:

$$\left\langle \hat{F}_{\mathrm{ext}}(f)^2\right\rangle = \frac{F_{\mathrm{ext}}}{4\pi^2 f^2}\cdot\left(\frac{\sin\pi f t_{\mathrm{m}}}{\cos\frac{\pi}{2}f t_{\mathrm{p}}}\right)^2. \tag{6.7}$$

A derivation of this expression requires multiple application of trigonometric relations and integration rules and can be found in Appendix A.2. With this, the expression for the expectation value of the PSD of a fluid-immersed particle exposed a series of periodic force steps reads:

$$\langle S(f)\rangle = \frac{1}{2\pi\gamma^2}\frac{1}{f_c^2+f^2}\left(2\gamma k_B T + \frac{F_{\mathrm{ext}}^2}{8\pi^2 f^2\cdot t_{\mathrm{m}}}\cdot\left(\frac{\sin\pi f t_{\mathrm{m}}}{\cos\frac{\pi}{2}f t_{\mathrm{p}}}\right)^2\right) \tag{6.8}$$

The first term of the sum can be recognized as the diffusive part whereas the second summand is the result of the periodically pushing force $F_{\mathrm{ext}}(t)$. A plot of Eq. (6.8) is shown in Fig. 6.2 (blue line). The periodic step force F_{ext} only influences the power spectral density at the repetition frequency $f_0 = t_{\mathrm{p}}^{-1}$ and uneven higher harmonics. Otherwise, the plot represents the typical curve for an optically trapped particle. The issue of motion blurring and aliasing due to the finite recording exposure time and frame rate is addressed using the corrections and fitting methods described in the papers by Wong *et al.* [113] and Berg-Sørensen *et al.* [109]. Their impact for parameters typical for the experimental configuration used in the following is demonstrated in the yellow and red curves in Fig. 6.2. For low frequencies ($f \ll f_c$) and without the scattering force, the trap stiffness can be derived from the average, frequency-independent height of the power spectrum S_0:

$$\kappa = \sqrt{\frac{2\pi\gamma k_B T}{S_0}} \tag{6.9}$$

Thus, the trap stiffness $\kappa = 2\pi\gamma f_c$ can be estimated even though the time resolution of the detection is well below the corner frequency f_c.

The ultimate goal of this section is to determine the force excerted on an optically trapped particle from the measured displacement spectrum. Applying a measurement time of $t_{\mathrm{m}} = 2^k t_{\mathrm{p}}$, where k is an integer, and using Eq. (6.8) without the diffusional contribution, the peak power at the repetition frequency $f_0 = t_{\mathrm{p}}^{-1}$ is:

$$\langle S(f_0)\rangle = \frac{t_{\mathrm{m}}}{8\pi^4\gamma^2}\cdot\frac{F_{\mathrm{ext}}^2}{\left(f_c^2+t_{\mathrm{p}}^{-2}\right)} \tag{6.10}$$

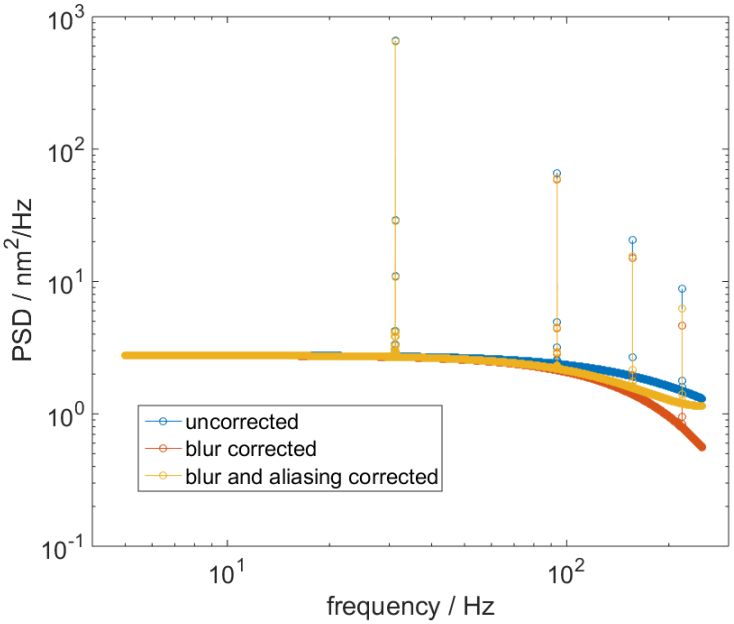

Figure 6.2 – Frequency dependence of the PSD. Sketch of an idealized power spectrum of a particle in a trap exposed to a series of periodic force steps according to Eq. (6.8). The used parameters are: $f_0 = t_\mathrm{p}^{-1} = 31.25\,\mathrm{Hz}$, $t_\mathrm{m} = 65.54\,\mathrm{s}$, $T = 308\,\mathrm{K}$, $\gamma = 108.45 \times 10^{-11}\,\mathrm{kg\,s^{-1}}$, $f_c = 603Hz$, $F_\mathrm{ext} = 20\,\mathrm{fN}$. For higher harmonics of the repetition frequency f_0, which corresponds tothe first peak, an alteration of the peak heights due to the corrections becomes visible.

If the parameters of the surrounding fluid are known, this expression contains only measurable quantities and can finally be solved for the force F_ext:

$$\boxed{F_\mathrm{ext} = \frac{4\pi^2}{\sqrt{t_\mathrm{m}}} \cdot \sqrt{2\pi^2\gamma^4\kappa^2 + \frac{1}{2}\gamma^2 t_\mathrm{p}^{-2}} \cdot \sqrt{\langle S\left(f_0\right)\rangle}} \tag{6.11}$$

Note, that besides the trap stiffness κ, the parameters particle radius, temperature and viscosity are included through the drag coefficient $\gamma = 6\pi\eta r$, considering that $\eta = \eta\left(T\right)$. Consequently, they influence the uncertainty of the force determination. In the following, an example for the applicability of Eq. (6.11) will be given, including an estimation of the experimental error due to these parameters.

6.2 Measuring the scattering force on plasmonic particles

The plasmonic nature of metal nanoparticles results in a significantly enhanced and strongly wavelength-dependent mechanical response on incident light in the visible regime [71, 120, 121]. Consequently, gold nanoparticles have been shown to be a good choice for sensitive force detection [10]. Here, the resolution of sub-Brownian scattering forces on a gold nanoparticles of a diameter of 80 nm is demonstrated. To derive a value for the optical scattering force, the analysis strategy outlined in the previous section will be applied.

While scattering forces have been considered theoretically for decades [114] and the emergent field of photonic force microscopy builds on measuring net forces on nanoparticles in solution [6], to our knowledge isolated scattering forces on a single gold nanoparticle have never been determined experimentally. The optical force on a plasmonic nanoparticle can be decomposed into two contributions [260]: the scattering force, and the gradient force (see Section 2.3 for a general introduction to optical forces). The scattering force represents the momentum transfer from the external radiation field to the nanoparticle by scattering and absorption [99, 261] and points along the axis of the energy flux of the light beam. In contrast, the gradient force is directed along the intensity gradient of the beam. If the gradient force exceeds the scattering force, particles can be trapped by light [70].

However, measuring scattering forces is challenging due to the inherent thermal fluctuations caused by the surrounding liquid. The application of strong laser light close to the plasmon resonance resulting in strong scattering forces goes along with substantial heating, also known as *plasmonic heating* [262–264]. Low scattering forces, on the other hand, are hidden by the inherent thermal fluctuations of the particle. Hence, a possible strategy to overcome both the challenge of the force sensitivity and the low scattering force is to apply a periodic scattering force to a trapped gold nanoparticle (Eq. (6.8)).

Experimental setup

A switchable optical scattering force is introduced to the system by coupling a resonant laser through a single-mode fiber perpendicular to the trapping beam. The switching process (on/off) is controlled by blocking the laser output periodically with a chopper wheel. The resonant fN scattering forces on single gold nanoparticles (diameter: 80 nm) were measured in a non-resonant single beam optical tweezer with dark field detection [125].

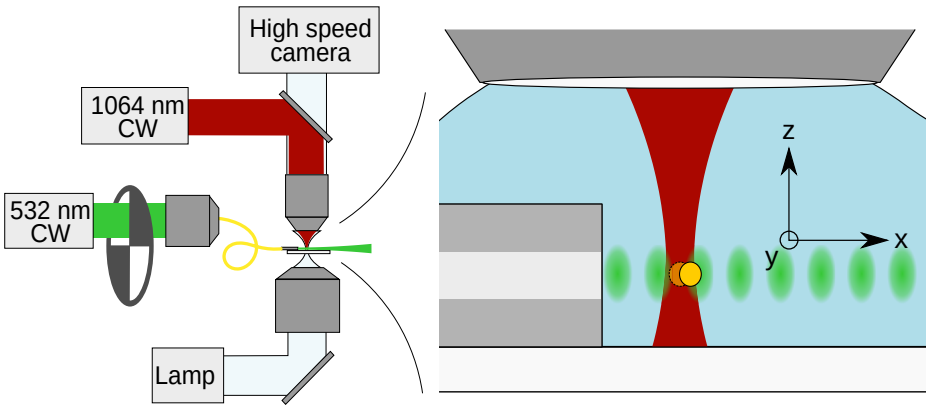

Figure 6.3 – Laser microscopy setup. Sketch of the microscopy setup for fN precise measurement of scattering forces. A gold nanoparticle is trapped in water with a focused NIR laser, while chopped green laser light from a fiber pushes the particle orthogonal to the trapping beam (Ref. [259], Fig. 1). Further details can be found in Section 3.1.

Fig. 6.3 shows a sketch of the laser microscopy setup. A nonresonant 1064 nm CW laser was coupled into an upright microscope and focused through a water immersion objective. The laser power of 50 mW (measured after the objective) resulted in a trap stiffness of 2.6 fN/nm, allowing for stable optical trapping of a single gold nanoparticle over tens of minutes. Trapping took place in water with a temperature of 24 °C, however, laser irradiation would lead to an increase of the particle temperature to 50 °C. Inside an optical trap, fluctuations of the heated particle or *Hot Brownian Motion* [40] needs to be taken into account via Eq. (2.8), resulting in an effective particle temperature of only 35 °C (please see Appendix A.4 or Ref. [259] for a detailed derivation of the temperature in the vicinity of the particle surface).

The 532 nm laser was coupled through an optical single-mode fiber. The output end of the fiber was stripped down to the 125 µm cladding diameter and placed on the microscope cover slide, with the fiber output propagating along the x-axis (see Fig. 6.3). With this, the 532 nm laser beam is perpendicular to the trapping laser beam, which propagates along the $-z$-axis. The relative position of the trapped nanoparticle and the fiber was controlled using a piezoelectric stage. The fiber end was positioned 75 µm away from the trapped particle in the x-axis. The beam diverges slightly at the fiber output. Therefore a CCD camera was used for beam profiling, and determined the beam width at the particle to be 6 ± 2 µm corrected for the refractive index of water. Since the diameter of the gold nanoparticle (80 nm) was much smaller than this beam width, a spatial intensity gradient can be neglected. Irradiation with laser light at the plasmon resonance frequency therefore results only in a forward-directed scattering force. The power density of the resonant laser was chosen to be so low that heating effects do not play a role here. This was confirmed by control measurements for the particle position distribution with the green laser on and off showing that this difference in temperature cannot be resolved.

It is also important that the possibility of thermophoresis that would push the particle along a temperature gradient due to plasmonic heating [264] can be neglected for the present experimental conditions. A gold nanoparticle is in thermal equilibrium within picoseconds after the irradiation with a laser beam due to the high thermal conductivity of gold [265]. Throughout the measurements, the exposure time of the optically trapped gold particles was in the range of several milliseconds. Although the particles are only irradiated from one side, the particle temperature is therefore completely uniform [266]. Videos were recorded with a high speed camera at an image acquisition rate of 500 Hz and an exposure time of 1.9 ms. The rotational frequency of the chopper wheel was synchronized with the image acquisition frequency using a home built frequency splitter. In a typical experiment, 2^{11} chopper cycles with a frequency of 31.25 Hz, i.e. one sixteenth of the image acquisition frequency, were considered. In order to determine the scattering force on a single gold nanoparticle, two different calibration and analysis methods corresponding to the strategies in Section 6.1 will be presented. The first is a rough approximation of the

particle in a trap as a Hookean spring, while the second represents an analytic solution of the full problem.

Data evaluation in real and Fourier space

Figure 6.4A shows a typical displacement time series of a gold nanoparticle, including both pushing with maximal laser intensity and the thermal fluctuations. The position distribution shown in Fig. 6.4B is Gaussian, justifying that the potential can be assumed as harmonic. Additionally, the width of the position distribution could be used to determine the force constant of the optical trap via the equipartition theorem. Figure 6.4C represents a zoom of the displacement time series showing two periods of chopping, again with no visible sign of the switching of the scattering force. By averaging the tracked time series with respect to the chopping period, the spatial displacement is revealed with subpixel resolution. In Fig. 6.4D, two cycles were averaged with all the following events resulting in a maximal displacement of 6.6 nm.

Analysis of particle movements in optical tweezers can also be done using the PSD of the particle movement [109]. The system was calibrated based on traces of the trapped particle without the scattering beam. Using Eq. (6.8) and $F_{\mathrm{ext}} = F_{\mathrm{scatt}} = 0$, the particle movement can then be described in terms of a frequency-dependent PSD by

$$\langle S(f) \rangle = \frac{4\pi\gamma k_B T}{\kappa^2 + 4\pi^2\gamma^2 f^2}, \tag{6.12}$$

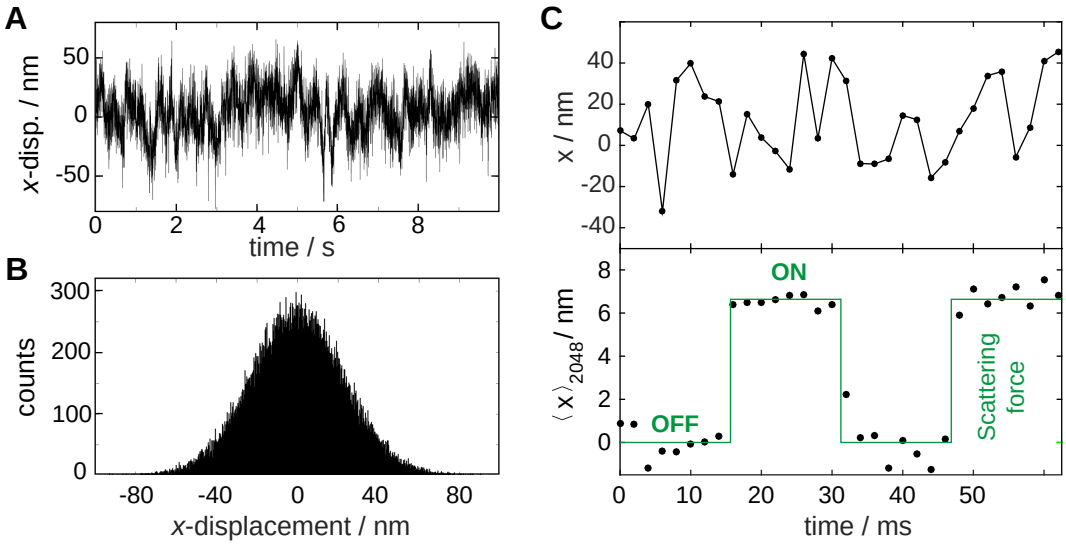

Figure 6.4 – Periodic averaging of particle displacement. (A) Raw trace of a trapped particle for $t_{\mathrm{m}} = 65.54\,\mathrm{s}$ and 2^{11} repetitions of the scattering force pushes. (B) Position distribution plot of the time series shown in A. (C) Detailed view of A showing the first two pushing cycles. The displacement caused by the scattering force is hidden by thermal fluctuations. The displacement time trace averaged with respect to t_{p} clearly shows the displacement resulting from switching the optical scattering force on and off and revealing a mean displacement of the particle of 6.6 nm.

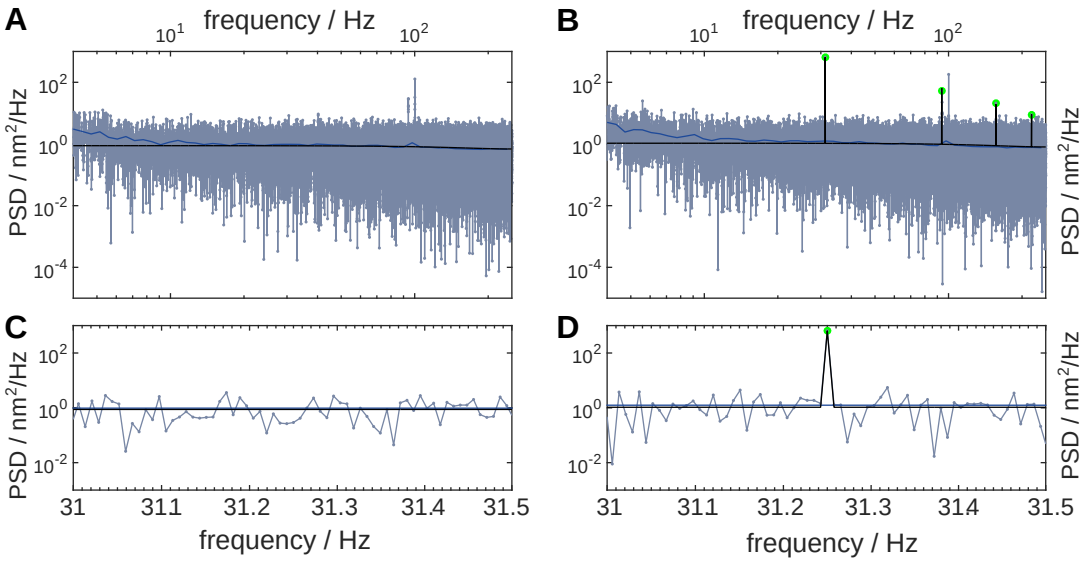

Figure 6.5 – Measured PSD. (A) PSD plot of the movement of a trapped gold nanoparticle with $t_m = 65.54\,s$ using 500 fps. The black line is a fit providing a force constant $\kappa = 2.4\,fN/nm$. Blue dashed line: average of logarithmic windows. (B) PSD plot as in A but in presence of a chopped scattering beam (532 nm, 31.25 Hz chopper frequency). Large green dots highlight the measured PSD at the chopping frequency and higher harmonics. The black line is now a plot of the analytic conversion from the peak height of the first harmonic to a corresponding value of 23 fN. (C) and (D) are zooms of A and B. Note, that the first noise peak in A does not overlap the third harmonic of the chopping frequency.

showing the typical f^{-2}-drop for high frequencies and a constant plateau for low frequencies. Figure 6.5A shows the PSD based on the measured data shown in Fig. 6.4A. The black line is a fit to the measured PSD above 20 Hz as described in the paper by Berg-Sørensen *et al.* [109], taking aliasing and blur into account. As discussed above, starting from the second harmonic, the correction does indeed account for small differences (cf. Fig. 6.2).

The fit including the temperature of 35 °C and the associated viscosity $\eta = 0.7191\,mPa\,s$ according to [267] results in a force constant of $\kappa = 2.6\,fN/nm$. The corresponding corner frequency is $f_c = 603\,Hz$ in agreement with previous work on gold nanoparticles [71, 121]. The characteristic bent at the corner frequency, known from typical tweezer power spectra, is not seen because the corner frequency is higher than the Nyquist frequency of the detection. Below 10 Hz the PSD is dominated by mechanical noise, for instance drift. In addition, two noise peaks were always present at 94.14 Hz and 100 Hz. Now turning on the chopped green scattering laser beam, a significant peak is seen at the chopping frequency as well as at odd harmonics (Fig. 6.5B). Zooms into a more narrow frequency range presented in Fig. 6.5C and D reveal that the peak at the chopping frequency is very sharp. All measured peaks nicely fit with theory.

Measurement of fN scattering forces and comparison to theory

Since the force constant is known from the calibration measurement, the first order peak corresponding to the chopping frequency, $t_p^{-1} = 31.25\,\mathrm{Hz}$, can now be used to determine the magnitude of the scattering force using Eq. (6.8). With this, the data presented in Fig. 6.5A reveals a measured scattering force of 23 fN. If the averaging technique demonstrated in Fig. 6.4B is used, an average displacement $\Delta x = 6.6 \pm 0.9$ nm is found providing a scattering force of $F_{\mathrm{scatt}} = \kappa \Delta x = 16 \pm 4$ fN. This agrees well with the value found by PSD analysis. The averaged standard deviation corresponds to averaged position data like the one shown in Fig. 6.4C and provides for $N = 2^{11}$ a minimal force sensitivity of

$$\Delta F = \sigma_{\mathrm{avg}} \kappa = \sqrt{\frac{k_B T \kappa}{N}} \approx 2.2\,\mathrm{fN}$$

exploiting the relation of κ and σ via equipartition theorem.

Having characterized the system allows us to test whether the scattering force scales linearly with the power of the scattering beam. A series of measurement was done on a single particle kept at the same position. For each measurement the power was changed and 2^{10} chopping events were measured. In Fig. 6.6, solid squares correspond to a measured value of the scattering force. The values for the optical scattering force are in the low fN regime and show the expected linear relationship with respect to laser intensity (Fig. 6.6A). A discussion of the error bars taking into account statistical uncertainties of the measured signal, the trap stiffness κ, deviation in the particle size r, and uncertainties in the temperature, T, can be found in Appendix A.3. The experimental error is in the same order of magnitude as the sensitivity of the measurements.

In order to test the spatial variation across the scattering beam, the position perpendicular to the beam direction was varied by moving the fiber relative to the trap. The resulting measured scattering forces are plotted in Fig. 6.6B. As expected, based on the Gaussian beam shape, the data points can be fitted with a Gaussian curve matching the beam width measured independently as described earlier. The maximal scattering force predicted from the fit of the spatial variation is $F_{\mathrm{scatt}}^{\mathrm{exp}} = 21.1\,\mathrm{fN}$. The error for the maximum measured force was 3.0 fN.

Now, the experimentally observed scattering force can be compared to theoretical calculations (see Section 2.3 for a general introduction). A number of different approaches exist [260, 271, 272], all relying on a knowledge of the refractive index of gold nanoparticles. Here, the scientific community mostly agrees on the dielectric function for bulk gold provided by Johnson and Christy [123] in 1972. However, it should be mentioned that large deviations in the dielectric function have been reported by several different groups [268, 273]. All these studies have been done for bulk gold, not for single particles. Therefore, finding experimental methods like the one presented here is crucial in predicting and understanding optical scattering forces.

The calculation of the theoretical optical scattering force is done using an adapted version of the *Matlab* toolbox provided by Nieminen et al. [98, 115]. The algorithm is based on the T-matrix approach to scattering theory first presented by Waterman [274, 275]. The T-matrix method allows for calculating the optical force excerted by a Gaussian laser beam on a single spherical gold nanoparticle. In the present case of a spherical, isotropic particle, the T-matrix method is closely related to Mie theory [72]. For the calculation of the optical scattering force exerted by a 532 nm laser on a 80 nm gold particle, a beam waist of 7 µm

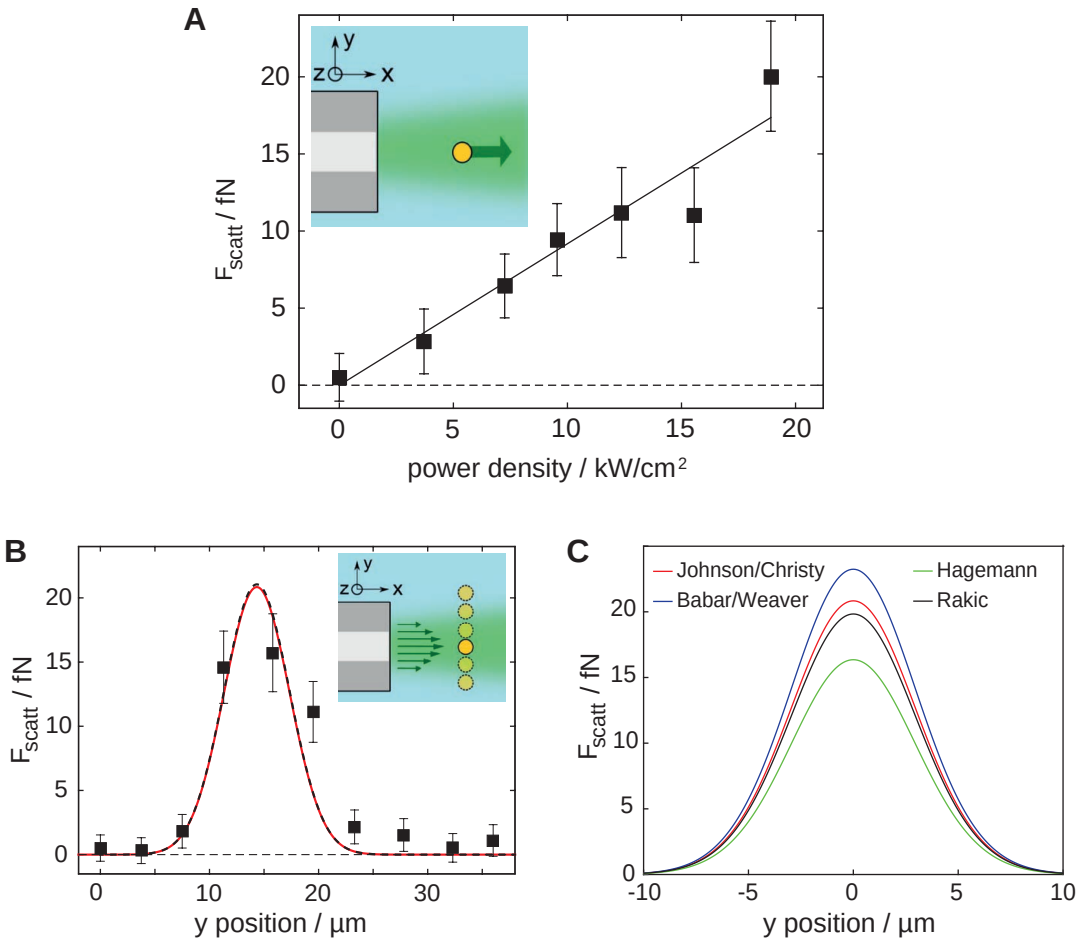

Figure 6.6 – Measurement of fN forces and comparison to Mie calculations. The insets are sketches of the experimental configuration. Solid squares mark measured forces. The error bars correspond to a maximum error estimation. (A) Measured scattering force versus applied output power of resonant laser light for $N = 2^{10}$ force pulses repeating with a frequency of 31.25 Hz corresponding to 32.77 s measurement time. (B) Measured scattering force for a spatial displacement along the Gaussian profile of the scattering beam for $N = 2^{11}$. The red curve in is the theoretical curve based on Mie simulations and Ref. [123]. Its width matches the full width half maximum value of 8.0 ± 1.8 µm from the Gaussian fit of the measured data (black dashed curve). (C) Comparison of the calculated scattering force with respect to the radial position of the particle for different refractive indices of gold. The refractive indices are taken from Johnson and Christy [123], Babar and Weaver [268], Hagemann *et al.* [269] and Rakić *et al.* [270].

at the particle position is assumed, which was interpolated from a previous measurement of the beam. The optical scattering force exerted by a 532 nm laser on an 80 nm gold particle could be calculated. The refractive index of water used in the calculations is 1.33. The choice of the refractive index of gold has a significant influence on the theoretically calculated values of the scattering force. In Fig. 6.6C, the scattering force for four different refractive indices of gold are compared. The resulting scattering forces differ by up to 6.9 fN (up to 42 %). This huge value spread due to different refractive index data reflects the difficulty of predicting optical forces theoretically.

Finally, the results of the simulation with the parameters of the spatial variation experiment are compared with corresponding measurements in Fig. 6.6B. It is seen that the spatial dependency of the theoretical scattering force is a Gaussian curve with a maximum of $F_{\mathrm{scatt}}^{\mathrm{theo}} = 21.1\,\mathrm{fN}$ (solid red curve). The maximum scattering force of the fit of the measured spatial variation is 21.1 ± 5.8 fN which is in excellent agreement with the theoretical prediction assuming a refractive index of gold as reported by Johnson and Christy [123]. To conclude, their data set seems indeed best to fit the refractive index of gold nanoparticles at a wavelength of $\lambda = 532\,\mathrm{nm}$ (cf. Fig. 6.6B).

6.3 Detection and measurement of fluidic force fields

Fluidic coupling is an important communication strategy in biological microfluidics, that applies for example in blood flow [276] or bacteria swarming [277, 278]. Two different fluid dynamic interactions can be distinguished: (i) stochastic fluctuations that are important for chemotaxis [279] and (ii) long-range deterministic coupling that governs cell-cell and cell-surface interactions [280].

As mentioned in Chapter 1 and 5, the experimental investigation of the latter is however challenging since the expected forces are usually overwhelmed by thermal forces manifesting in stochastic fluctuations. Even though fluidic fields around individual bacteria [280] and so-called bacterial carpets [281] could be determined using tracer particles, a quantitative determination of the forces has not been done. In the previous two sections, an ultrasensitive technique to measure fN forces was developed, which will now be applied to study fluidic force fields. Therefore, two different model systems will be considered. First, an artificial *microswimmer* [282–284] is employed to create an accurately defined flow field. Second, the results will be compared to the fluidic spectrum of an optically trapped bacterium.

A light-driven rotation of a colloidal microswimmer can be realized already with a conventional, non-polarized laser beam that allows a simultaneous trapping and rotation of an object with shape anisotropy [285]. This is due to a momentum transfer through the

deflected laser light that exerts a torque in distance r from the center-of-mass [286]. This torque is in equilibrium with the viscous drag γ of the rotating microswimmer:

$$F_{\text{opt}} \cdot r = \gamma \cdot 2\pi \cdot f_{\text{rot}} \tag{6.13}$$

Without the presence of gradient forces exerted by the optical tweezer, a chiral microswimmer would propel along its long axis, which has been realized earlier by Ghosh and Fischer using magnetized micro-screws in homogeneous magnetic fields [145, 146]. In the following it will be demonstrated that a high degree of control can also be achieved using optical forces.

Creation and detection of flow fields with light-driven micro-screws[3]

Colloidal micro-screws with a diameter of 530 nm and a length of 2.35 µm were fabricated from silicon dioxide (SiO_2) by glancing angle deposition[4]. The resulting structure consisted of a helical part and a 'head', represented by a silica bead with a diameter of 500 nm (Fig. 6.7A). A single-beam near-infrared (NIR, $\lambda = 1064$ nm) optical tweezer was used to trap a micro-screw in a fluidic environment along its long axis (Fig. 6.7B) in an upright microscopy setup. Under dark-field illumination, the white-light Rayleigh scattering of a trapped micro-screw allowed for its precise optical tracking. Two configurations, head up and head down, could be distinguished: While for the first case, Brownian motion was seen as typical for trapped microparticles, in the second case (head down), a rotation of the micro-object around the center of the optical trap is observed. In the following, only the rotational case will be considered.

Figure 6.7D shows frequency spectra of the tracked movement of the micro-screw for two different laser powers of the trapping laser. The width of the peaks around the mean rotation frequencies f_{rot} can be seen as a measure for the quality and reproducibility of the rotation for a given micro-screw. As expected for a helical scatterer, the rotation frequency f_{rot} showed a linear increase with increasing power of the trapping laser. Applying a modulation on the trapping laser power between two fixed values P_1 and P_2 induced a time-dependent micro-flow. Experimentally, the modulation was achieved by rotating a cover slide half-sputtered with Au-Pd in the trapping beam, which resulted in a nutation-like movement of the micro-screw in the optical trap (Fig. 6.7C).

Notably, the micro-screw's frequency spectrum shown in Fig. 6.7E now reveals two frequencies and overtones: First, an average rotation frequency f_{av} with a mean value of around 7.5 Hz which corresponds to the average trap power between the two powers P_1 and P_2. Second, the modulation frequency f_{mod} appears. The reason for this is that with the laser power, also the trap constant κ_S, which determines the micro-screw's position

[3] The presented results build on experiments performed by Dr. S. Kirchner. A detailed description of the experimental results and setups used can be found in her PhD thesis at LS Feldmann, LMU Munich, published in 2015 [287]. For the present thesis, the raw data was evaluated to obtain a measured force.

[4] Colloidal micro-screws were fabricated by D. Walker in the group of Prof. P. Fischer (MPI for Intelligent Systems, Stuttgart, Germany). Details can be found in Ref. [146].

distribution in radial direction, experiences a modulation with f_{mod}. The time-dependence of the harmonic potential thus leads to an additional oscillation in radial direction. The modulated micro-screw motion, as skteched in Fig. 6.7C, can be summarized in terms of an equation of motion in polar coordinates (r, φ):

$$\begin{aligned} m_r \ddot{r}(t) &= -\kappa\left(P\left(f_{\mathrm{mod}}, t\right)\right) \cdot r(t) - \gamma_r \dot{r} + \xi_r(t) \\ m_\varphi \ddot{\varphi}(t) &= -\gamma_\varphi \dot{\varphi}(t) + \xi_\varphi(t) \end{aligned} \tag{6.14}$$

The equation system (6.14) is a set of ordinary linear differential equations that possesses a stochastic driving term. Here, m_i and γ_i denote the effective masses and drag coefficients for radial and angular motion and $\xi_r(t)$ and $\xi_\varphi(t)$ stand for translational and rotational random thermal forces, repectively. A possible coupling of the two equations caused by the stochastic forces is not considered. The trapping laser power modulation is represented by a power-dependent, radial spring constant $\kappa\left(P\left(f_{\mathrm{mod}}, t\right)\right)$ with $P\left(f_{\mathrm{mod}}, t\right)$ being a rectangular function, alternating between a maximum value P_1 and a minimum value P_2 with a modulation frequency f_{mod}. The solution for the angular movement is of the form

$$\varphi(t) = \omega_0\left(P\left(f_{\mathrm{mod}}, t\right)\right) \cdot t = 2\pi \cdot f_{\mathrm{rot}} \cdot t,$$

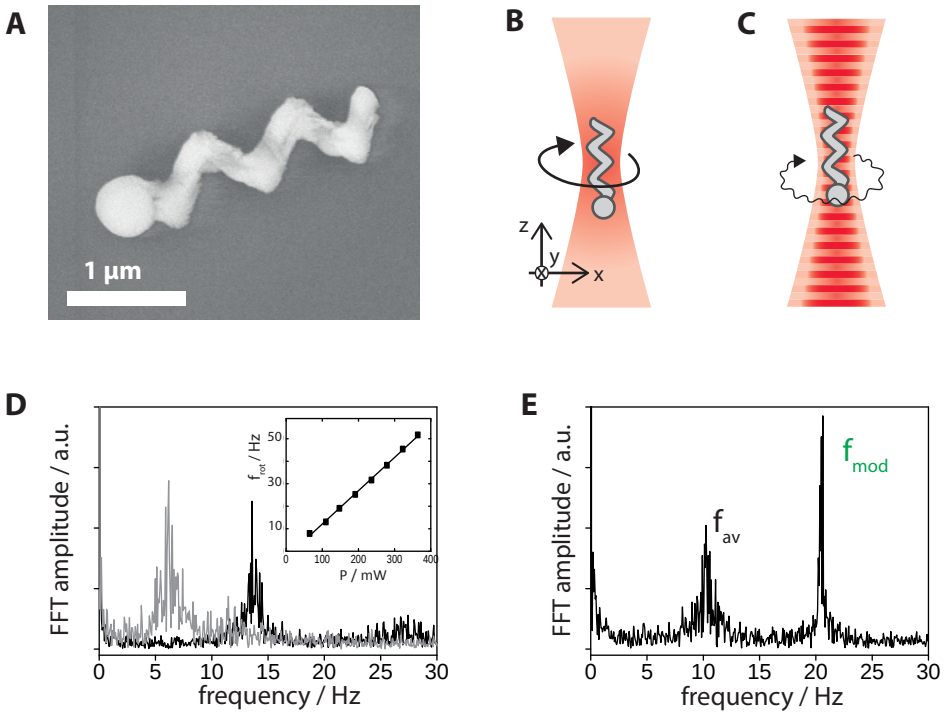

Figure 6.7 – Movement of colloidal micro-screws in an optical trap. (A) SEM image of a single micro-screw. (B) Sketch of the rotation of a micro-screw in an optical trap. (C) Sketch of the nutation-like movement of a micro-screw in an optical trap with modulated laser power. (D) and (E): Frequency spectra of tracked movement in one spatial direction of a micro-screw trapped with an optical tweezer corresponding to the configurations sketched in (B) and (C).

where ω_0 is a constant angular velocity that depends on the laser intensity. In the last step, the linear relationship between P and $\omega_0 = 2\pi \cdot f_{\text{rot}}$ as visible from the inset in Fig. 6.7D is inserted. The stochastic driving force causes a nonvanishing offset of the screw from the symmetry center of screw motion in the 2D plane. It is in the order of the width of its position distribution

$$\sigma(P) = \sqrt{\frac{k_B T}{\kappa(P)}}$$

The dynamics of the radial movement, following the first line of Eq. 6.14, is that of a driven damped spring with a power-dependent spring constant $\kappa(P(f_{\text{mod}}, t))$.

Flow field measurement

To detect the micro-flow around the micro-screw, an SiO_2 particle (diameter $d = 1.76\,\mu\text{m}$) was trapped with a second NIR laser beam with equal laser power in a distance of a few µm to the rotating micro-screw (Fig. 6.8A). The stationary flow field around the rotating micro-screw trapped with constant laser power leads to a fixed displacement of the detector bead from its equilibrium position in the optical trap [288]. Hence, the frequency spectrum of the detector does not show any distinct peaks in this case. For a modulation of the laser intensity, which induces time-dependent and periodic micro-flow, the detector spectrum reveals a peak at the modulation frequency $f_{\text{mod}} = 9\,\text{Hz}$ (Fig. 6.8B). This peak represents the radial component of the movement of the micro-screw caused by the laser modulation which is transmitted through the fluid as a mechanical wave.

In the next step, the magnitude of the periodic microflow is derived. For this, the displacement time series of the detector bead is averaged with respect to the modulation frequency f_{mod} as described in Section 6.1. This reveals a subpixel sinusoidal displacement in both spatial directions, with a maximal displacement of $\langle x \rangle_{\text{mod}} = 7\,\text{nm}$ and $\langle y \rangle_{\text{mod}} = 9\,\text{nm}$, respectively (Fig. 6.8C). For a trap constant $\kappa_{\text{det}} = 13.0\,\text{fN/nm}$ of the detector, which was determined by equipartition (see Section 2.4), a measured force can then be calculated by multiplying the trap constant with the average displacement. Forces in the order of magnitude of tens of fN could be detected depending on the distance between detector and microscrew, with a force threshold of 26 fN (see Fig. 6.8D).

The decay of the velocity field in the equatorial plane from a point-force source

$$\mathbf{F}_{\text{source}} \cdot \delta(\mathbf{r} = 0)$$

in a distance $\mathbf{r}$ can be formulated via the *Oseen tensor* G, using Eq. (2.25):

$$\mathbf{v}_{\text{meas}}(\mathbf{r}) = \mathbf{F}_{\text{source}} \cdot G(\mathbf{r}) = \frac{\mathbf{F}_{\text{source}}}{8\pi\eta} \cdot \left(\frac{1}{r} + \frac{\mathbf{r} \cdot \mathbf{r}}{r^3} \right), \tag{6.15}$$

where η represents the dynamic viscosity of water. The associated hydrodynamic force measured at the position of a detector bead, $\mathbf{F}_{\text{meas}}$, can be assessed by multiplication with the viscous drag D_{det} of the spherical detector particle. In order to fit the force

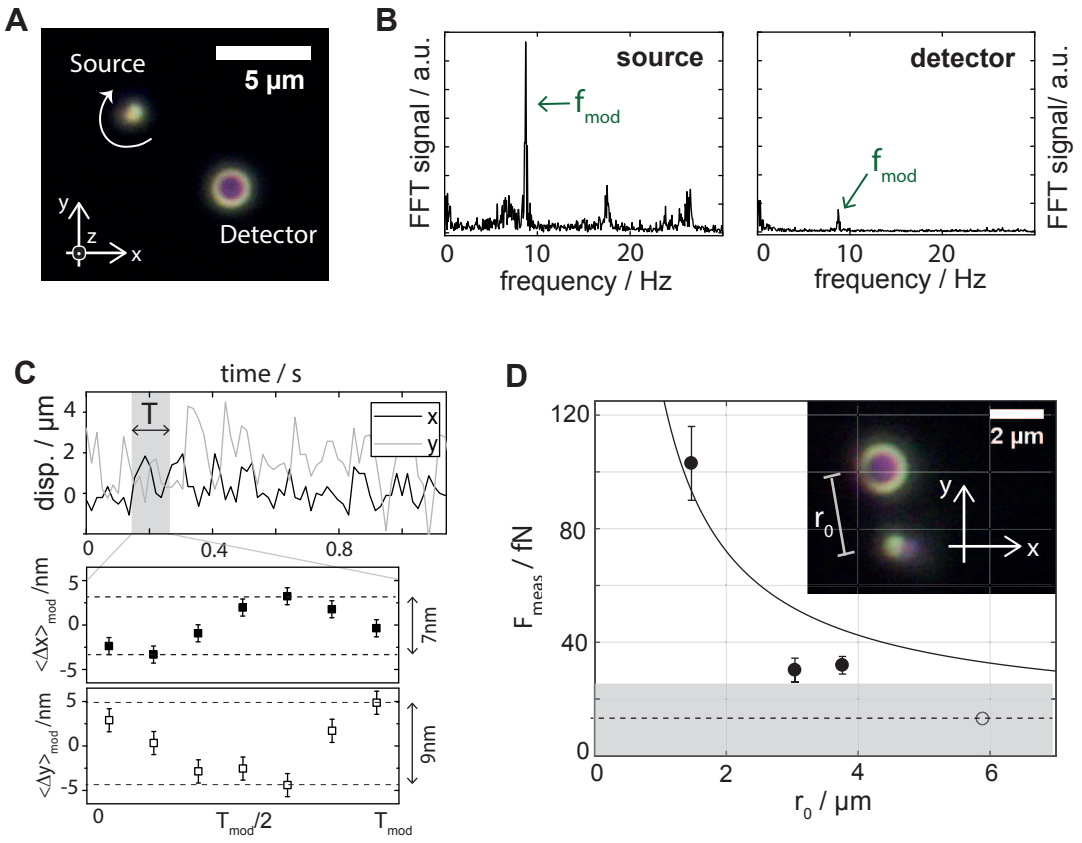

Figure 6.8 – Flow field measurements around an optically modulated microscrew. (A) Dark-field image of the experimental configuration, including a rotating micro-screw as a source of flow and an 1.76 µm SiO_2 bead as flow detector in a distance of 1.5 µm. (B) Frequency spectra measured at the source and the detector, respectively. The modulation frequency was 9 Hz. (C) Displacement trace of detector particle dominated by Brownian motion. Averaging with respect to $T_{\mathrm{mod}} = f_{\mathrm{mod}}^{-1} = 0.2\,\mathrm{s}$ yields average displacements $\langle x \rangle_{\mathrm{mod}}$ and $\langle y \rangle_{\mathrm{mod}}$ of a few nm. (D) Measurement of the force field in different distances. At 5.89 µm, no signal was measured. Each datapoint corresponds to a measurement of different micro-screws modulated with a known frequency of 5 - 10 Hz. The solid line corresponds to a fit of the source force F_{source} with Eq. (6.18).

stemming from the micro-screw, the one-dimensional Langevin equation is used to describe the movement of the detector particle located at a distance r_0 from the rotating micro-screw.

$$0 = -\kappa_{\mathrm{det}} \cdot x\,(t) - \gamma_{\mathrm{det}}\,(\dot{x}\,(t) - v_{\mathrm{meas}}\,(r_0)) - \xi\,(t)\,, \tag{6.16}$$

On averaging of Eq. (6.16) over the modulation period $T_{\mathrm{mod}} = f_{\mathrm{mod}}^{-1}$, all thermal contributions vanish so that the expression for the measured force reads:

$$F_{\mathrm{meas}}\,(r_0) = \kappa_{\mathrm{det}} \cdot \langle \Delta x \rangle_{\mathrm{mod}} = \gamma_{\mathrm{det}} \cdot v_{\mathrm{meas}}\,(r_0) \tag{6.17}$$

Using Eq. (6.15) leads to an expression for the net force F_{source} from a rotating micro-screw modeled as a point source:

$$F_{\mathrm{source}} = \frac{4}{3} \cdot \frac{r_0}{d} \cdot \kappa_{\mathrm{det}} \cdot \langle \Delta x \rangle_{\mathrm{mod}} \tag{6.18}$$

Application of Eq. (6.18) to the data yields an average value of

$$F_{\text{source}} = 89 \pm 45 \text{ fN}.$$

The solid black line in Fig. 6.8D describes the resulting fit of Eq. (6.17). This value is an average of different micro-screws, which explains the rather high error bar since the angular rotation speed is highly depending on the exact shape of the micro-screw [289]. The magnitude of the force however fits the expectations of forces relevant for bacteria interacting in swarms at low Reynolds numbers [290]. When using a mechanical lock-in strategy, directed periodic fN forces can be distinguished and measured with spatial resolution around a source of microflow.

Measurement of the force exerted by *Bacillus subtilis*[5]

The feasability of force measurements around individual bacteria will now be demonstrated. A flagellated bacterium (*Bacillus subtilis*) was trapped using a constant laser power (Fig. 6.9A). A track of a detector bead motion located nearby revealed a sharp peak in the frequency spectrum at 62 Hz (Fig. 6.9B). In this case, the spectrum shown is the geometric sum of the displacement spectra in both x and y directions. In control experiments with a mutant of *Bacillus subtilis* which does not possess flagella no such peak could be observed. Consequently, the detected signal was associated with bacterial swimming [11].

Averaging of the time series in real space reveals the detector displacement caused by the periodic microflow around the bacterium (Fig. 6.9C). A clear oscillation of the y-displacement was observed as a function of time, while Δx vanishes within the experimental uncertainty/resolution. The peak detected in Fig. 6.9B can thus be attributed to a force in y-direction and the one-dimensional description derived above can be applied.

To determine this force, the optically trapped bacterium is compared to the micro-screw experiment decribed in the previous section. For this, the spectral peak in the measurement of bacteria is associated with the modulation frequency f_{mod} applied in the micro-screw rotation experiments. Both Fourier peaks represent a periodic force pulse and with it, a time-dependent flow field around the source. Using Eq. (6.17), a force of $F_{\text{meas}} = 651\,\text{fN}$ is derived from the data of Fig. (6.9)B. With Eq. (6.18), the force exerted by the bacterium then results in

$$F_{B.subtilis} \approx 1.13\,\text{pN}.$$

Our experiment shows that an optically trapped bacterium generates an oscillatory flow field which can be studied quantitatively. This oscillatory component could be a consequence of the precession of the cell body within the optical trap. To further analyze

[5]The data used was recorded by Dr. S. Kirchner. For details on bacteria culture, experimental design and results, please see Ref. [11].

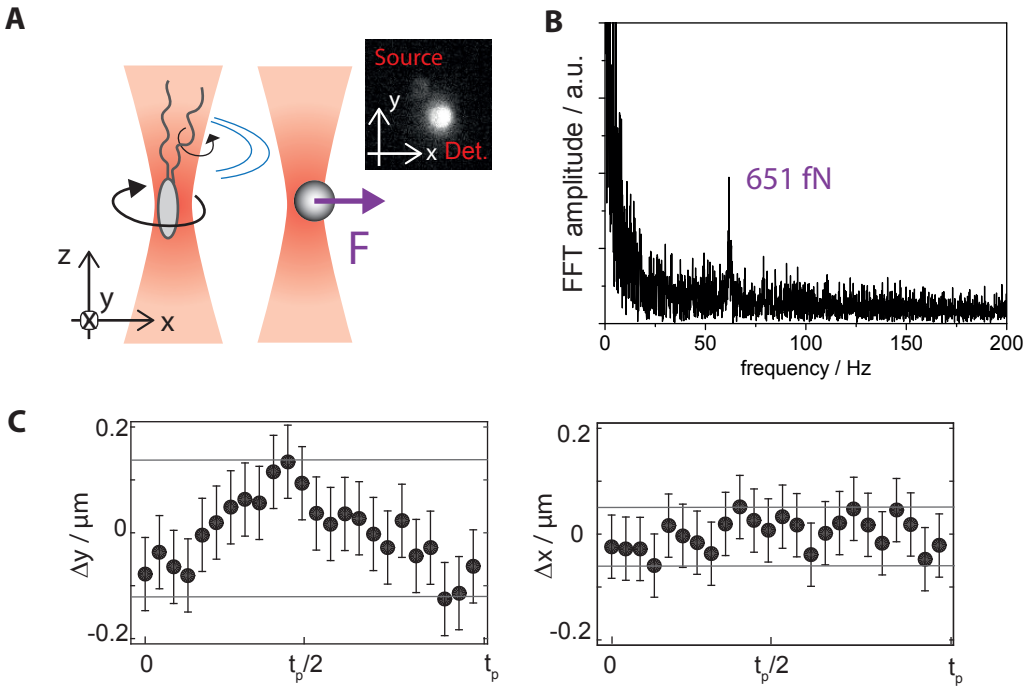

Figure 6.9 – Measurement of the Flow field around *Bacillus subtilis*; after Kirchner *et al.* [11]. (A) Sketch and dark field images of the experimental configuration and a bacterium *Bacillus subtilis*. (B) Measured frequency spectrum of the detector bead revealing a sharp peak at 62 Hz. The trap constant of the detector bead was 33 fN/nm. (C) Detector time series averaged with respect to the detected frequency resulting in average x and y displacements over on period t_p.

hydrodynamic coupling of bacterial cells, the dynamic behavior of rotating helices trapped e.g. in holographic tweezers are suited as a model system.

6.4 *Discussion:* Optical measurement of fN forces in biological systems

In photonic force spectroscopy [6, 291, 292], micro- or nanoparticles are confined in the focus of an optical tweezer and pick up the microfluidic vibration spectrum originating from a source acting on the surface of the detector bead. The small size of these optofluidic force detectors allows for a local resolution down to the nanoscale. With complex particle shapes or hybrids consisting of at least two materials as force detectors, high sensitivities of less than 100 fN have been achieved [20, 253, 255, 258, 293] and based on their anisotropy, these objects offer advanced readout possibilities To push these limits even further, a *mechanical lock-in strategy* was developed and implemented enabling the detection of fN forces in fluid and at room temperature with a spherical detector. These forces were measured in three different model systems to demonstrate the applicability of the technique. The strategy is based on a periodic repetition of a force pulse which is picked up by a spherical detector bead and analyzed in frequency space.

The limits of force resolution were explored using plasmonic nanoparticles as sensitive detectors. In Section 6.2, the scattering force acting on a single gold nanoparticle was expeirmentally determined and found a resolution threshold of 2.2 fN, corresponding to a detector displacement of a few nm. This is significantly below the force sensitivity obtained before in the context of optical tweezers applications in liquids [6, 254, 255, 258]. Regarding measurements of switchable forces with conventional optical tweezers, the force sensitivity could be improved by an order of magnitude compared to previous experiments [257], which permitted the determination of the scattering force on a plasmonic nanoparticle. Further, the refractive index of gold can be derived from the scattering force. The presented method thus allows, in principle, for a determination of the dielectric function of individual gold nanoparticles, which has not been done to date [268]. Such an experiment would however require a variation of the incident wavelength by e.g. a tunable diode laser. For $\lambda = 532\,\mathrm{nm}$, it could already be shown that the results would best fit the data of Johnson and Christy for bulk gold [123].

An improvement of the method could be achieved by a more elaborate detection system such as a photodiode and an automatization of the measurement procedure. Combining the method with single particle spectroscopy, for example by measuring the Rayleigh scattering, would enable the determination of optical properties of nanoparticles of arbitrary shape and material. Vice versa, measured optical parameters could be compared to theoretical calculations of translational and rotational diffusion of nonspherical nanoparticles [294, 295] or Hot Brownian motion [37, 38]. This would permit a validation of fundamental theoretical results in nanooptics and fluctuation theory.

Femtonewton sensitive detectors are highly desired for intracellular force measurements. Since the cellular meshwork possesses a pore size of 10–100 nm [296], particles of these dimensions could provide additional insight in subcellular processes. So far, only few experimental approaches use nanoparticles as sensitive force detectors. Plasmonic nanoparticles provide the advantage that no labeling is necessary. Moreover, these are often based on optical tweezers interfering with the cellular environment [52]. Having identified gold nanoparticles as a promising candidate for sensitive force measurements, the detection of endocytosed nanoparticles (40–80 nm) could be demonstrated inside a living cell (Fig. 6.10). By probing local perturbations within the cell cytoplasm by single particle tracking [297], periodic intracellular forces could be detected in a tweezer-free approach [298].

This approach paves the way for localized force mapping of living cells with fN resolution, which offers a broad applicability for investigating the heterogeneous nature of intracellular processes. However, for an accurate calculation of intracellular forces, the formulas derived in the present chapter are no longer valid as anomalous diffusion [51] must be taken into account (see Section 2.2 for a short introduction).

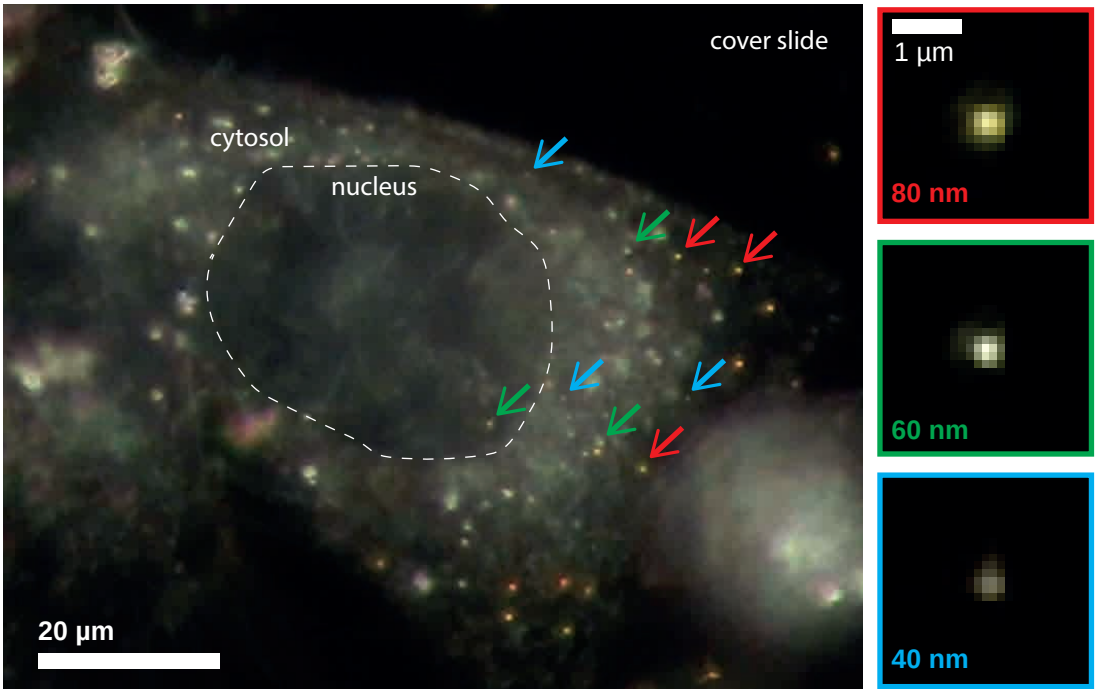

Figure 6.10 – Gold nanoparticles as intracellular force detectors. Gold nanoparticles of three different diameters are endocytosed by a CHO cell and can be seen in dark-field microscopy. A more quantitative distinction can be done by scattering spectroscopy. Single particle spectra of the three exemplary particles shown can be found in Fig. 3.6.

Hydrodynamic coupling in arrays of individual objects is a valuable test bench for intercellular communication. Over the last decade, self-propelled microswimmers of decreasing size have been developed and fabricated to understand propulsion mechanisms at low Reynolds numbers [299, 300]. Here, time-reversible swimming motion does not lead to any directed movement [23]. To model the complex locomotion strategies of microswimmers [22], custom-designed particles such as the presented micro-screw can be considered [146, 301, 302].

While the mechanistic understanding of swimming at low Reynolds numbers has become textbook knowledge today [303], the coupling between the individual swimmers is not very well investigated. This is certainly also due to a lack of appropriate techniques to measure such hydrodynamic coupling in simple setups. In theoretical work, even a synchronization between individual microparticles has been predicted [278, 304]. In Section 6.3, a time-dependent flow measurement around different sources of microflow was demonstrated. In difference to the scattering force measurement, here, the particle acts as a sensor that does not alter the force field. It was shown that a light-driven micro-screw is a good model system for bacterial propulsion since it can produce microflow of comparable magnitude in its environment.

Some examples of arrays useful for synchronization measurements are given in Fig 6.11, ranging from artificial light-driven microswimmers (Fig. 6.11A) over flagellated bacteria to cells exposed to a time-dependent trap configuration ('cell shaking', see Chapter 5). Fig-

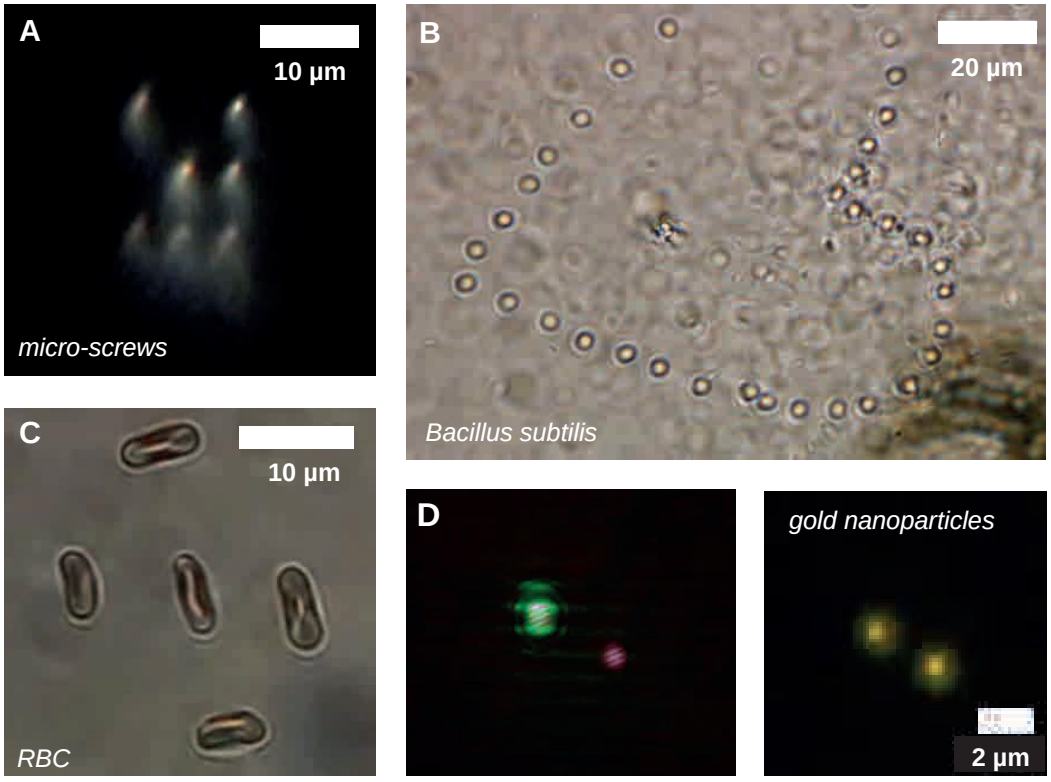

Figure 6.11 – Experimental configurations for fluid coupling experiments. (A) Array of light-driven micro-screws; (B) array of self-propelling bacteria; (C) array of red blood cells; each cell is aligned using three laser beams. (D) Left: NIR double trap overlayed with a single green laser beam. Right: Two optically trapped gold nanoparticles.

ure 6.11D shows a configuration that could be used to test theoretical results in statistical physics of systems where the condition of detailed balance is violated [305]: A double NIR optical tweezer traps two individual gold nanoparticles. An additional green laser aligned with one of the traps introduces non-equilibrium conditions by heating one of the two particles. The common principle for all configurations in Fig. 6.11 is that in an array, no additional external detector particle is used to detect the microfluidic vibrations emitted by neighbouring objects, but the interacting objects itselves act as detectors.

Chapter 7

Conclusion: *Controlling Mesoscale Mechanics with Light*

In a fluidic environment and at room temperature, Brownian noise dominates most mesoscale forces so that many common force measurement techniques become deficient. In this thesis, novel optomechanical methods were devised that are capable of detecting and quantifying changes in mechanical parameters of biological model systems. To circumvent thermal fluctuations, microfluidic force fields of known spatiotemporal modulation were introduced and combined with optofluidic detection. Using this concept, a force resolution of a few fN allowing for nanometer precise particle manipulation was achieved.

In Chapter 4, the light-controlled changes of mechanical properties and shape transformations of photoswitchable vesicles were investigated. The photosensitive vesicles were produced by electroformation from 100% photoswitchable phospholipids (*azo*–**PC**). Under UV illumination a decrease of the membrane bending rigidity of up to 1.5 orders of magnitude was found. This demonstrates that the photoisomerization of *azo*–**PC** on a molecular scale caused macroscopic changes of the mechanical membrane properties. This change in membrane bending rigidity also resulted in shape transitions of the entire vesicles. Several shape transformations, namely budding, pearling or invagination, were observed and could be controlled by the illumination conditions. Shape transitions of vesicles are commonly controlled by parameters such as temperature, chemical composition or osmotic pressure, which exhibit long ramping times and are often irreversible. The use of light as a stimulus opens unprecedented possibilities to trigger vesicle mechanics by adjusting strength and dynamics of the illumination. By 'flipping' an external UV light switch, mechanical energy in an order of magnitude that is relevant for cellular processes can be stored locally. For this, a thin membrane tube was pulled from a vesicle under UV illumination by using a focused laser beam, which remained stable. For switching on visible light, the photolipids were switched in the visible light-adapted photostationary state and the tube retracted back. Thinking one step ahead, this effect could be used in order to regulate forces and distances on the nanometer scale on demand. Combining a local control of light with the light-induced shape transitions might further enable chemical microreactors. In conclu-

sion, photoswitchable membranes represent a unique model system that allows to improve the understanding of intrinsic membrane forces in living cells.

In Chapter 5, focused laser light was utilized to 'shake' individual cells in a known pattern by a holographic laser array. In order to study the coupling between cell and fluid, a 'detector' particle was positioned in the flow field using an additional optical tweezer. Fourier transforming its displacement time series revealed a characteristic spectrum, or fingerprint, of the cell's shape, mechanical properties, its movement and its fluidic environment. Variations in any of these parameters could be traced by analyzing changes in Fourier peak ratios of the characteristic detector displacement spectrum. In the presented experiments, a variation of (i) the stiffness of red blood cells depnending on the osmotic conditions, (ii) the viscosity of the cell medium and (iii) the cell type were considered. The method of cell-fluid coupling is minimally invasive and requires neither mechanical contact nor fluorescent labeling. Performing flow-detection in a few µm distance from the cell enables a measurement of the microflow that a neighboring cell is actually exposed to. Additionally, cell-fluid coupling spectroscopy could serve as a means to distinguish one cell from another by their characteristic fingerprints from, e.g., a whole blood sample. In Section 5.1, an efficient signal processing model was proposed harboring the potential to disentangle the different factors leading to the measured detector spectrum. In this approach, the cell is modeled as an 'analog filter'. To quantify the observations, however, a deeper understanding, more accurate calibration and detailed modeling of transduction of mechanical properties in the fluid are necessary.

In Chapter 6, the resolution limits in optofluidic force detection were explored. An optically trapped gold nanoparticle was pushed periodically from the side by the scattering force of light resonant with its particle plasmon. Based on simulations of Mie scattering, fN optical forces and nm displacements of the particle are expected. Using an analytical model, scattering forces between 3 fN and 21 fN could be derived. To the best of my knowledge, this represents the smallest switchable force measured in fluid at room temperature. fN forces could potentially be important e.g. for hydrodynamic cell-cell interactions. To investigate this, measurements of the microfluidic field around an artificial microswimmer and a swimming bacterium were evaluated and indeed revealed forces in the fN to pN range over distances several µm away from the bacterial cell.

In summary, the high spatiotemporal precision of light was exploited to manipulate and measure biological systems at the micro- and nanoscale. The switchable character of light was employed to regulate dynamics and mechanics of biophysical model systems on a timescale faster than diffusion. In terms of spatial control, nanoparticles combined with a mechanical lock-in readout were used to realize nanometer-precise force probes.

Appendix A

Appendix

A.1 Molecular collision frequency and speed

A simple model is used to describe the collision frequency between a small particle with the molecules in the surrounding liquid (molecule density ρ). Assuming a spherical particle and that the molecule diameters are negligible with respect to the particle, the effective collision area A equals its cross-sectional area:

$$A = \pi r^2 \tag{A.1}$$

The volume that must be considered for the collisions is given by the volume swept by the particle within a measurement time interval t:

$$V \approx A\langle v \rangle t \tag{A.2}$$

Here, $\langle v \rangle$ is approached as the average speed of the molecules. In other word, the particle is assumed being at rest since its speed is much smaller than the speed of the molecules. Now, the Maxwell-Boltzmann probability density function for the molecular speed of noble gases is used in order to estimate the speed of the liquid molecules:

$$\langle v \rangle = \sqrt{\frac{8k_B T}{\pi m}} \tag{A.3}$$

In case of water, the average molecule speed results in $\langle v \rangle = 587\,\mathrm{m\,s^{-1}}$. The average speed of the small particle is orders of magnitude smaller and can be derived from the equipartition theorem, Eq. 2.5.

Using that the number of molecules per volume n can be derived from the molecules density ρ and the molecular mass M by $n = \rho \cdot M^{-1} \cdot N_A$, the collision frequency f_{col} and the mean free path λ can be calculated with the following formula:

$$f_{\mathrm{col}} = n\frac{dV}{dt} = n_{\mathrm{H_2O}} \cdot r^2 \sqrt{\frac{8\pi k_B T}{m}} \tag{A.4}$$

$$\lambda_{\mathrm{col}} = \frac{\langle v \rangle}{f_{\mathrm{col}}} = \left(n_{\mathrm{H_2O}} \cdot \pi \cdot r^2\right)^{-1} \tag{A.5}$$

Example values for particles with sizes relevant in this thesis (80 nm gold particle, 1 µm beads, 1 µm cells) in water as a surrounding liquid ($n_{H_2O} = 3.34 \times 10^{28}$ molecules/m^3, $M = 18\,\mathrm{g\,mol^{-1}}$) are summarized in the following table:

material	d in m	ρ in g cm^{-3}	m in kg	f_{col} in molecules/s	λ_{col} in m
gold	80×10^{-9}	19.3	5.17×10^{-18}	9.9×10^{16}	6.0×10^{-15}
SiO_2	1×10^{-6}	2.65	1.39×10^{-15}	1.5×10^{19}	3.8×10^{-17}
cell (water)	10×10^{-6}	1.00	5.24×10^{-13}	1.5×10^{21}	3.8×10^{-19}

Figure A.1 – Collision frequency and mean free path of spherical particles of different material.

We recognize that the mean free path λ_{col} is much smaller than the particle diameter, illustrating the high number of collisions. If the resulting average speeds of the particles in water are considered, which can be derived using the equipartition theorem, Eq. (2.5)

$$\langle v \rangle = \sqrt{\frac{3k_B T}{m}}, \tag{A.6}$$

Reynolds numbers can be derived using Eq. (2.1):

material	d in m	$\langle v \rangle$ in m s^{-1}	Re
gold	80×10^{-9}	0.048	3.8×10^{-3}
SiO_2	1×10^{-6}	0.0030	3.0×10^{-3}
cell (water)	10×10^{-6}	0.000 15	1.5×10^{-3}
water molecule	3×10^{-10}	586	0.1758

Figure A.2 – Reynolds numbers for thermal motion of small particles at room temperature.

For viscosity $\eta = 1.0\,\mathrm{mPa\,s}$ and density $\rho = 1.0\,\mathrm{g\,cm^{-3}}$, room temperature values were assumed from common textbook sources. In the last line, the values for a water molecule ($m = 3.0 \times 10^{-26}\,\mathrm{kg}$) are given for comparison, using Eq. (A.3). Due to the very high velocity of water molecules, here, Reynolds numbers are no longer low.
In the experiments of this thesis, the flow speeds of applied flow are smaller than the thermal average speeds $\langle v \rangle$. With this, we can assume low Reynolds numbers throughout.

A.2 Fourier transform of the periodic step force $F_{\text{ext}}(t)$

$F_{\text{ext}}(t)$ is an oscillatory driving force with a period length t_{p}, and a total length in time, $t_{\text{m}} = 2^k \cdot t_{\text{p}}$, with k an integer:

$$F_{\text{ext}}(t) = F_{\text{ext}} \cdot \sum_{0}^{k=N-1} \left[H(t - kt_{\text{p}}) - H(t - kt_{\text{p}} - \frac{t_{\text{p}}}{2}) \right] \tag{A.7}$$

where F_S is the magnitude of the force, H is the Heaviside step function and $N = \frac{t_{\text{m}}}{t_{\text{p}}}$ is the number of oscillations. The definition of the Fourier transform is applied on $F_{\text{ext}}(t)$:

$$\begin{aligned}
\hat{F}_{\text{ext}}(f) &= F_{\text{ext}} \cdot \int_{-\infty}^{\infty} \sum_{0}^{k=N-1} \left(H(t) - H\left(t - \frac{t_{\text{p}}}{2}\right) \right) e^{-i2\pi ft} dt \\
&= F_{\text{ext}} \cdot \left(\sum_{0}^{k=N-1} e^{-i2\pi fkt_{\text{p}}} \right) \int_{-\infty}^{\infty} \left(H(t) - H\left(t - \frac{t_{\text{p}}}{2}\right) \right) e^{-i2\pi ft} dt \\
&= F_{\text{ext}} \cdot \left(\sum_{0}^{k=N-1} \left(e^{-i2\pi ft_{\text{p}}} \right)^k \right) \int_{0}^{\frac{1}{2}t_{\text{p}}} e^{-i2\pi ft} dt \\
&= F_{\text{ext}} \cdot \frac{1 - e^{-i2\pi ft_{\text{m}}}}{1 - e^{-i2\pi ft_p}} \cdot \frac{i}{2\pi f} \cdot \left(e^{-i\pi ft_{\text{p}}} - 1 \right)
\end{aligned} \tag{A.8}$$

In the first transformation, a nontrivial algebraic identity is used [306]. In a last two steps, the integration is done and the geometric series expression is applied. The use of several trigonometric identities results in

$$\left\langle \hat{F}_{\text{ext}}(f)^2 \right\rangle = \frac{F_{\text{ext}}^2}{4\pi^2 f^2} \cdot \left(\frac{\sin \pi ft_{\text{m}}}{\cos \frac{\pi}{2} ft_{\text{p}}} \right)^2 \tag{A.9}$$

A.3 Maximum error calculation

The errorbars ΔF of the plot are based on a maximum error calculation, taking into account statistical uncertainties of the measured signal, the trap stiffness κ, deviation in the particle size r, and uncertainties in the temperature, T, by a linear addition of the maximally possible deviations from the calculated force by uncertainties ΔF_i

$$\Delta F = \Delta F_\sigma + \Delta F_\kappa + \Delta F_r + \Delta F_T \tag{A.10}$$

The relative contributions of all quantities is of comparable magnitude. ΔF_σ is the standard deviation of the noise of the measured signal in an interval of a few Hz around the peak. ΔF_κ is the standard deviation of the fitted κ within a series of measurement. ΔF_r is the maximal deviation of the calculated forces for the uncertainties of the particle radius ($\Delta r = 4\%$ of the particle radius r). The uncertainty of the T and with this, of the viscosity $\eta(T)$ is assumed to be 2 K as discussed earlier.
ΔF is maximal for the largest forces measured where all uncertainties ΔF_i contribute with an equal order of magnitude. For decreasing force values, ΔF decreases down to the standard deviation of the noise in the PSD, as expected. The experimental error is in the same order of magnitude as the sensitivity of the measurements.

A.4 Optical heating of a gold nanoparticle

The theoretical description of the movement of the gold nanoparticle is provided by the Langevin equation (2.16). The noise term $\xi(t)$ involves the water temperature in the vicinity of the surface of the gold nanoparticle.
Irradiation of a gold nanoparticle with light goes along with absorption of photons. For plasmonic metal nanoparticles, this is a strongly wavelength dependent process and leads to a significant temperature increase of the particle [307]. This holds especially if the focused trapping laser has a high power density, even though it is off-resonant with the particle plasmon. For this reason, we can no longer use the measured temperature of the fluid (24 °C) in the Langevin equation. The analytical model described by Eq. (6.6) involves the temperature T of the water close to the gold surface. Since the width of the position distribution of the gold nanoparticle in the experiments here is less than a particle radius and no significant cooling effects are therefor expected, the surface temperature of the particle can be used in good approximation.

The amount of absorbed laser power is $Q = \sigma I$ with σ the absorption cross-section and I the mean power density averaged over the area of the absorption cross-section. To determine the temperature distribution around the particle we used the commercial simulation software COMSOL Mulitphysics to solve the heat transfer equation numerically. We assume that the particle is surrounded by an infinite liquid volume with a fixed temperature at infinity. The material parameters used for the calculation are $C_p^{\text{gold}} = 129\,\text{J}\,\text{kg}^{-1}\,\text{K}^{-1}$ and $C_p^{\text{water}} = 4200\,\text{J}\,\text{kg}^{-1}\,\text{K}^{-1}$ for the heat capacity at constant pressure, $\lambda^{\text{gold}} = 318\,\text{W}\,\text{m}^{-1}\,\text{K}^{-1}$ and $\lambda^{\text{water}} = 0.6\,\text{W}\,\text{m}^{-1}\,\text{K}^{-1}$ for the thermal conductivity and $\rho^{\text{gold}} = 19\,300\,\text{kg}\,\text{m}^{-3}$ and $\rho^{\text{water}} = 1000\,\text{kg}\,\text{m}^{-3}$ for the density of gold and water respectively.

By applying Mie theory, the absorption cross-section of a gold nanoparticle in water irradiated with a 1064 nm trapping laser can be calculated to be $\sigma = 9.68 \times 10^{-5}\,\mu\text{m}^2$. Here, $n_{\text{gold}} = 0.26 + 6.97i$ (Johnson and Christy [123]) and $n_{\text{water}} = 1.33$ were used as the refractive index of gold and water, respectively. The power density of a Gaussian beam propagating along the z direction is given by

$$I(x,y,z) = \frac{2P}{\pi w(z)^2} \exp\left(\frac{-2(x^2+y^2)}{w(z)^2}\right) \qquad w(z) = w_0\sqrt{1+\frac{z^2}{z_0^2}}$$

where P is the total laser power, w_0 is the beam waist and z_0 is the Rayleigh length. For the simulation, measured values of the power of the NIR laser ($P = 50\,\text{mW}$) and the beam waist ($w_0 = 550\,\text{nm}$) are used. The Rayleigh length $z_0 = 480\,\text{nm}$ is chosen such that the divergence angle of the beam matches NA = 1. Simulations along the lines of Nieminen *et al.* [115] provide a stable trapping position for a distance $z_{\text{trap}} = 258\,\text{nm}$ from the focal plane. Therefore, the average power density at the particle position is $I = 8.25 \times 10^6\,\text{W}\,\text{cm}^{-2}$, and, consequently, a heating power of $Q = 8.0\,\mu\text{W}$.

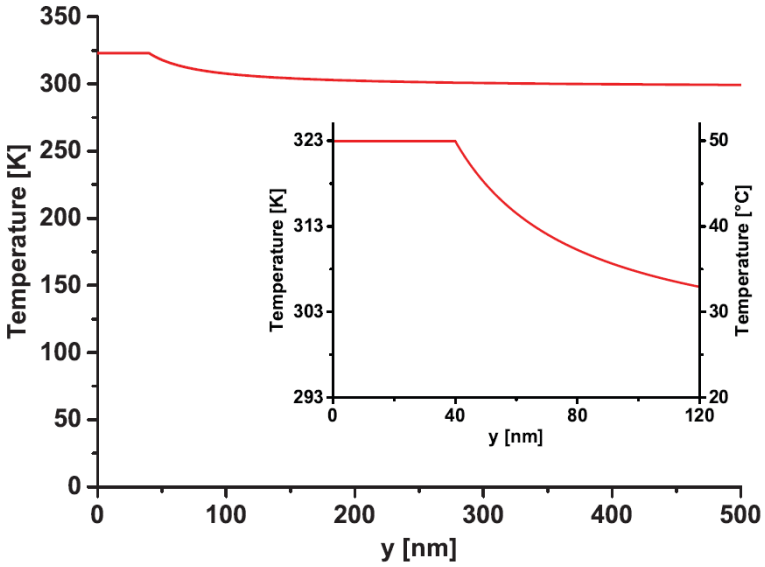

Figure A.3 – Temperature increase with respect to the distance from the center of the gold particle.

The resulting temperature distribution is shown in Fig. A.3. The temperature increase at the particle surface is $T_{\mathrm{NIR}} = 25.8\,\mathrm{K}$, which is a maximum estimation of the real temperature. For the analysis used in this work, the water temperature at the particle surface is relevant. For an estimate, Hot Brownian motion of the gold nanoparticle in case of being confined in a weak harmonic potential is considered. An effective temperature can be estimated using Eq. 2.8 [40] which applies for standard trapping conditions of gold nanoparticles of comparable size. Even if the the particle position distribution has a width of less than one particle radius, fluctuations in axial direction have been reported to be higher and thus, the approximation of a weak harmonic potential is justified.
Known variations in the input variables account for uncertainties in the order of magnitude of 1 K. The power density of the resonant laser was chosen so low that heating effects do not play a role here. This was confirmed by control measurements for the particle displacement with the green laser on and off showing that this difference in temperature cannot be resolved. For the error calculations, an uncertainty of the temperature of 2 K is assumed which is in the order of magnitude of all uncertainties. Throughout this work and for all calculations, a temperature of $T = 308\,\mathrm{K}$ is assumed. At this temperature, no formation of microbubbles is expected [308, 309].

A.5 Reaction scheme of *azo*–PC

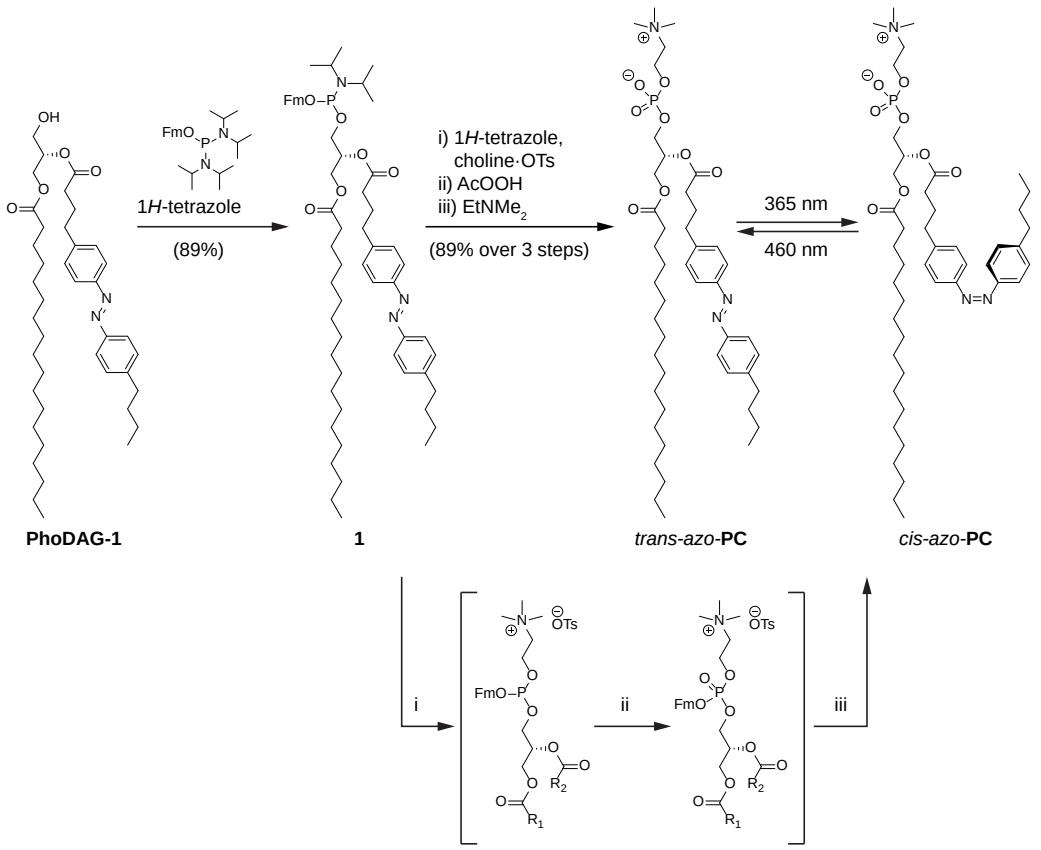

Figure A.4 – Reaction scheme. *azo*–**PC** was synthesized from the photoswitchable diacylglycerol PhoDAG-1 in high yield. Phosphoramidite chemistry was used to install the phosphocholine headgroup. *azo*–**PC** could be isomerized between its *cis*and *trans*-configurations with UV-A and blue light, respectively. Please see Ref. [153] for further details on the synthesis.

A.6 Measured vesicle bending rigidities

The bending rigidities of 16 *azo*–**PC** vesicles in both UV- and white light-adapted photostationary states were measured (1-7 measurements per value, the given error is the standard error of the mean) as described in Section 3.2. The sizes of the vesicles ranged between 2 µm and 15 µm. In most cases, the bending rigidity decreased significantly and

vesicle No.	$\kappa_{\text{trans}}/10^{-19}$J	$\kappa_{\text{cis}}/10^{-19}$J	ratio
1	$48 \cdot 10^3$	$(12 \pm 60) \cdot 10^3$	4.0
2	15.0 ± 7.8	1.8 ± 0.5	1.3
3	18.4	1.0	18
4	3.2 ± 2.9	2.2	1.5
5	$(3.7 \pm 3.7) \cdot 10^3$	$(1.5 \pm 0.4) \cdot 10^3$	2.5
6	5.05 ± 0.14	1.14 ± 0.05	4.4
7	140 ± 49	6.1 ± 1.2	23
8	1.07 ± 0.42	0.21	5.1
9	0.82 ± 0.38	0.07	12
10	0.5	0.096 ± 0.016	5.2
11	1.6 ± 0.4	0.37 ± 0.04	4.3
12	9.2 ± 5.3	1.3	7.1
13	4.6 ± 1.7	0.28 ± 0.08	16
14	0.69 ± 0.26	1.07 ± 0.19	0.64
15	0.082 ± 0.034	0.031 ± 0.007	2.6
16	0.35 ± 0.1	0.22 ± 0.02	1.6

Figure A.5 – Bending rigidities measured by deformation of individual GUVs. For each vesicle, several cycles of photoswitching were performed to obtain an average value.

reversibly for switching a vesicle between the UV-A- and white light- adapted states. These values agree (within two orders of magnitude) with bending rigidities already reported for fluid vesicle [172]. In two cases, very high bending rigidities were measured, even though the change between the two states is of the same magnitude, which could indicate multilamellar membranes.

Bibliography

[1] I. Orlanski, Bulletin of the American Meteorological Society **56**, 527 (1975).

[2] T. Hänsch and A. L. Schawlow, Optics Communications **13**, 68 (1975).

[3] T. J. Kippenberg and K. J. Vahala, Science **321**, 1172 (2008).

[4] K. C. Neuman and A. Nagy, Nature Methods **5**, 491 (2008).

[5] L. P. Ghislain, N. A. Switz, and W. W. Webb, Review of Scientific Instruments **65**, 2762 (1994).

[6] O. M. Marago, P. H. Jones, P. G. Gucciardi, G. Volpe, and A. C. Ferrari, Nature Nanotechnology **8**, 807 (2013).

[7] A. Ashkin, J. M. Dziedzic, J. E. Bjorkholm, and S. Chu, Optics Letters **11**, 288 (1986).

[8] D. G. Grier, Nature **424**, 810 (2003).

[9] A. Einstein, Annalen der Physik **322**, 549 (1905).

[10] A. Ohlinger, A. Deak, A. A. Lutich, and J. Feldmann, Physical Review Letters **108**, 018101 (2012).

[11] S. R. Kirchner, S. Nedev, S. Carretero-Palacios, A. Mader, M. Opitz, T. Lohmüller, and J. Feldmann, Applied Physics Letters **104**, 093701 (2014).

[12] S. R. Kirchner, M. Fedoruk, T. Lohmüller, and J. Feldmann, Journal of Visualized Experiments **89** (2014).

[13] S. Nedev, S. Carretero-Palacios, S. R. Kirchner, F. Jäckel, and J. Feldmann, Applied Physics Letters **105**, 161113 (2014).

[14] E. Frey and K. Kroy, Annalen der Physik **14**, 20 (2005).

[15] L. von Bertalanffy, Science **111**, 23 (1950).

[16] J. Käs and E. Sackmann, Biophysical Journal **60**, 825 (1991).

[17] S. Svetina, ChemPhysChem **10**, 2769 (2009).

[18] C.-M. Lo, H.-B. Wang, M. Dembo, and Y.-L. Wang, Biophysical Journal **79**, 144 (2000).

[19] D. E. Discher, Science **310**, 1139 (2005).

[20] Q. Huang, J. Lee, F. T. Arce, I. Yoon, P. Angsantikul, J. Liu, Y. Shi, J. Villanueva, S. Thamphiwatana, X. Ma, L. Zhang, S. Chen, R. Lal, and D. J. Sirbuly, Nature Photonics **11**, 352 (2017).

[21] E. Lauga and T. R. Powers, Reports on Progress in Physics **72**, 096601 (2009).

[22] J. Elgeti, R. G. Winkler, and G. Gompper, Reports on Progress in Physics **78**, 056601 (2015).

[23] E. M. Purcell, American Journal of Physics **45**, 3 (1977).

[24] G. Batchelor, *An Introduction to Fluid Mechanics* (Cambridge University Press, New York, 1967).

[25] A. Sommerfeld, Atti del **4**, 116 (1908).

[26] J. Howard, *Mechanics of motor proteins and the cytoskeleton* (Sinauer associates Sunderland, MA, 2001).

[27] R. Brown, Philosophical Magazine Series **4**, 161 (1828).

[28] M. von Smoluchowski, Annalen der Physik **326**, 756 (1906).

[29] P. Langevin, Comptes Rendus de l'Académie des Sciences **146**, 530 (1908).

[30] J. B. Perrin, *From Nobel Lectures, Physics 1922-1941* (Elsevier Publishing Company, Amsterdam, 1926).

[31] S. Chandrasekhar, Reviews of Modern Physics **15**, 1 (1943).

[32] A. Moscatelli, Nature Nanotechnology, doi:10.1038/nnano.2016.60 (2016).

[33] G. G. Stokes, *On the effect of the internal friction of fluids on the motion of pendulums*, vol. 9 (Pitt Press, 1851).

[34] S. Kim and S. Karilla, *Microhydrodynamics: Principles and Selected Applications* (Butterworth Series of Chemical Engineering, London, 1991).

[35] J. Waterston, Philosophical Transactions of the Royal Society of London **183**, 1 (1892).

[36] W. Feller, *Selected Papers I*, 667–699 (Springer, 2015).

[37] D. Rings, R. Schachoff, M. Selmke, F. Cichos, and K. Kroy, Physical Review Letters **105**, 090604 (2010).

[38] D. Rings, M. Selmke, F. Cichos, and K. Kroy, Soft Matter **7**, 3441 (2011).

[39] G. Baffou and R. Quidant, Laser & Photonics Reviews **7**, 171 (2012).

[40] G. Falasco, M. V. Gnann, D. Rings, and K. Kroy, Physical Review E **90**, 032131 (2014).

[41] R. Kubo, Reports on Progress in Physics **29**, 255 (1966).

[42] H. Nyquist, Physical Review **32**, 110 (1928).

[43] H. B. Callen and T. A. Welton, Physical Review **83**, 34 (1951).

[44] W. Sutherland, Philosophical Magazine Series 6 **9**, 781 (1905).

[45] A. Einstein, Annalen der Physik **324**, 371 (1906).

[46] A. Einstein, Zeitschrift für Elektrotechnik und Elektrochemie **13**, 41 (1907).

[47] J. B. Johnson, Physical Review **32**, 97 (1928).

[48] M. Büttiker, Zeitschrift für Physik B Condensed Matter **68**, 161 (1987).

[49] V. Plerou, P. Gopikrishnan, L. A. Nunes Amaral, X. Gabaix, and H. Eugene Stanley, Physical Review E **62**, 3023 (2000).

[50] H. Stanley, L. Amaral, X. Gabaix, P. Gopikrishnan, and V. Plerou, Physica A: Statistical Mechanics and its Applications **299**, 1 (2001).

[51] R. Metzler and J. Klafter, Physics Reports **339**, 1 (2000).

[52] M. Guo, A. J. Ehrlicher, M. H. Jensen, M. Renz, J. R. Moore, R. D. Goldman, J. Lippincott-Schwartz, F. C. Mackintosh, and D. A. Weitz, Cell **158**, 822 (2014).

[53] M. Saxton, Biophysical Journal **66**, 394 (1994).

[54] D. S. Lemons, American Journal of Physics **65**, 1079 (1997).

[55] N. Wiener, Journal of Mathematics and Physics **2**, 131 (1923).

[56] G. E. Uhlenbeck and L. S. Ornstein, Physical Review **36**, 823 (1930).

[57] L. van Hemmen, *Vorlesungsskript Mechanik der Kontinua* (Technische Universität München, 2006).

[58] G. Stokes, Transactions of the Cambridge Philosophical Society **8**, 287 (1845).

[59] J. Happel and H. Brenner, *Low Reynolds number hydrodynamics* (Springer, 1983).

[60] Z. Zapryanov and S. Tabakova, *Dynamics of Bubbles, Drops and Rigid Particles* (Springer, 1999).

[61] C. F. Bohren and D. R. Huffman, *Absorption and Scattering of Light by Small Particles* (Wiley-VCH Verlag GmbH, 1998).

[62] L. Novotny and B. Hecht, *Principles of Nano-Optics* (Cambridge University Press, 2012).

[63] A. Ashkin, *Optical Trapping and Manipulation of Neutral Particles Using Lasers* (World Scientific Publishing Company, 2006).

[64] H. Rubinsztein-Dunlop, A. B. Stilgoe, D. Preece, A. Bui, , and T. A. Nieminen, *Photonics: Scientific Foundations, Technology and Applications, Volume III* (John Wiley & Sons, Inc., 2015).

[65] M. Fedoruk, *Plasmonic manipulation of thermoresponsive and thermosetting polymers*, Ph.D. thesis, LMU Munich (2013).

[66] A. Ohlinger, *Akustik mit optisch gefangenen Nanopartikeln*, Ph.D. thesis, LMU Munich (2012).

[67] A. S. Urban, *Optothermal Manipulation of Phospholipid Membranes with Gold Nanoparticles*, Ph.D. thesis, LMU Munich (2010).

[68] M. V. G. Kristensen, *Manipulation and Characterisation of Biomolecular Systems using a newly developed Counterpropagating Beams Setup*, Ph.D. thesis, Aarhus University (2012).

[69] M. Dienerowitz, *Plasmonic Effects upon Optical Trapping of Metal Nanoparticles*, Ph.D. thesis, University of St. Andrews (2010).

[70] A. Ashkin, Physical Review Letters **24**, 156 (1970).

[71] F. Hajizadeh and S. Reihani, Optics Express **18**, 551 (2010).

[72] G. Mie, Annalen der Physik **330**, 377 (1908).

[73] J. A. Lock and G. Gouesbet, Journal of Quantitative Spectroscopy and Radiative Transfer **110**, 800 (2009).

[74] G. S. Hartley, Nature **140**, 281 (1937).

[75] H. Rau, Angewandte Chemie International Edition in English **12**, 224 (1973).

[76] E. Müller, *Neuere Anschauungen der organischen Chemie* (Springer-Verlag, 1957).

[77] A. Dias, M. M. D. Piedade, J. M. Simões, J. Simoni, C. Teixeira, H. Diogo, Y. Meng-Yan, and G. Pilcher, The Journal of Chemical Thermodynamics **24**, 439 (1992).

[78] N. Nishimura, T. Sueyoshi, H. Yamanaka, E. Imai, S. Yamamoto, and S. Hasegawa, Bulletin of the Chemical Society of Japan **49**, 1381 (1976).

[79] J. Griffiths, Chemical Society Reviews **1**, 481 (1972).

[80] N. Tamai and H. Miyasaka, Chemical Reviews **100**, 1875 (2000).

[81] H. Satzger, S. Spörlein, C. Root, J. Wachtveitl, W. Zinth, and P. Gilch, Chemical Physics Letters **372**, 216 (2003).

[82] T. Cusati, G. Granucci, M. Persico, and G. Spighi, The Journal of Chemical Physics **128**, 194312 (2008).

[83] G. Hampson and J. M. Robertson, Journal of the Chemical Society **409** (1941).

[84] H. M. D. Bandara and S. C. Burdette, Chemical Society Reviews **41**, 1809 (2012).

[85] E. Merino and M. Ribagorda, Beilstein Journal of Organic Chemistry **8**, 1071 (2012).

[86] J. Henzl, M. Mehlhorn, H. Gawronski, K.-H. Rieder, and K. Morgenstern, Angewandte Chemie International Edition **45**, 603 (2006).

[87] B.-Y. Choi, S.-J. Kahng, S. Kim, H. Kim, H. W. Kim, Y. J. Song, J. Ihm, and Y. Kuk, Physical Review Letters **96**, 156106 (2006).

[88] T. Fujino and T. Tahara, The Journal of Physical Chemistry A **104**, 4203 (2000).

[89] I. Lednev, T.-Q. Ye, P. Matousek, M. Towrie, P. Foggi, F. Neuwahl, S. Umapathy, R. Hester, and J. Moore, Chemical Physics Letters **290**, 68 (1998).

[90] T. Nägele, R. Hoche, W. Zinth, and J. Wachtveitl, Chemical Physics Letters **272**, 489 (1997).

[91] Y. Ootani, K. Satoh, A. Nakayama, T. Noro, and T. Taketsugu, The Journal of Chemical Physics **131**, 194306 (2009).

[92] S. Yuan, Y. Dou, W. Wu, Y. Hu, and J. Zhao, The Journal of Physical Chemistry A **112**, 13326 (2008).

[93] P. Bortolus and S. Monti, The Journal of Physical Chemistry **83**, 648 (1979).

[94] A. A. Beharry and G. A. Woolley, Chemical Society Reviews **40**, 4422 (2011).

[95] J. E. Molloy and M. J. Padgett, Contemporary Physics **43**, 241 (2002).

[96] K. C. Neuman and S. M. Block, Review of Scientific Instruments **75**, 2787 (2004).

[97] K. Dholakia, P. Reece, and M. Gu, Chemical Society Reviews **37**, 42 (2008).

[98] T. A. Nieminen, N. du Preez-Wilkinson, A. B. Stilgoe, V. L. Loke, A. A. Bui, and H. Rubinsztein-Dunlop, Journal of Quantitative Spectroscopy and Radiative Transfer **146**, 59 (2014).

[99] A. S. Urban, S. Carretero-Palacios, A. A. Lutich, T. Lohmüller, J. Feldmann, and F. Jaeckel, Nanoscale **6**, 4458 (2014).

[100] A. Lehmuskero, P. Johansson, H. Rubinsztein-Dunlop, L. Tong, and M. Käll, ACS Nano **9**, 3453 (2015).

[101] M. E. J. Friese, T. A. Nieminen, N. R. Heckenberg, and H. Rubinsztein-Dunlop, Nature **394**, 348 (1998).

[102] G. Volpe and D. Petrov, Physical Review Letters **97**, 210603 (2006).

[103] A. I. Bishop, T. A. Nieminen, N. R. Heckenberg, and H. Rubinsztein-Dunlop, Physical Review Letters **92**, 198104 (2004).

[104] A. Yao, M. Tassieri, M. Padgett, and J. Cooper, Lab on a Chip **9**, 2568 (2009).

[105] J. Millen, T. Deesuwan, P. Barker, and J. Anders, Nature Nanotechnology **9**, 425 (2014).

[106] J. R. Moffitt, Y. R. Chemla, S. B. Smith, and C. Bustamante, Annual Review of Biochemistry **77**, 205 (2008).

[107] M. Capitanio, G. Romano, R. Ballerini, M. Giuntini, F. S. Pavone, D. Dunlap, and L. Finzi, Review of Scientific Instruments **73**, 1687 (2002).

[108] T. B. Lindballe, M. V. G. Kristensen, K. Berg-Sørensen, S. R. Keiding, and H. Stapelfeldt, Optics Express **21**, 1986 (2013).

[109] K. Berg-Sørensen and H. Flyvbjerg, Review of Scientific Instruments **75**, 594 (2004).

[110] T. Li and M. G. Raizen, Annalen der Physik **525**, 281 (2013).

[111] B. Lukić, S. Jeney, Ž. Sviben, A. J. Kulik, E.-L. Florin, and L. Forró, Physical Review E **76**, 011112 (2007).

[112] M. Andersson, F. Czerwinski, and L. B. Oddershede, Journal of Optics **13**, 044020 (2011).

[113] W. P. Wong and K. Halvorsen, Optics Express **14**, 12517 (2006).

[114] G. Gouesbet, Journal of Quantitative Spectroscopy and Radiative Transfer **110**, 1223 (2009).

[115] T. A. Nieminen, V. L. Y. Loke, A. B. Stilgoe, G. Knöner, A. M. Branczyk, N. R. Heckenberg, and H. Rubinsztein-Dunlop, Journal of Optics A: Pure and Applied Optics **9**, 196 (2007).

[116] P. C. Waterman, Physical Review D **3**, 825 (1971).

[117] M. I. Mishchenko, Journal of the Optical Society of America A **8**, 871 (1991).

[118] A. S. Urban, A. A. Lutich, F. D. Stefani, and J. Feldmann, Nano Letters **10**, 4794 (2010).

[119] M. Fedoruk, M. Meixner, S. Carretero-Palacios, T. Lohmüller, and J. Feldmann, ACS Nano **7**, 7648 (2013).

[120] K. Svoboda and S. M. Block, Optics Letters **19**, 930 (1994).

[121] P. M. Hansen, V. K. Bhatia, N. Harrit, and L. Oddershede, Nano Letters **5**, 1937 (2005).

[122] G. L. Tan, M. F. Lemon, D. J. Jones, and R. H. French, Physical Review B **72**, 205117 (2005).

[123] P. B. Johnson and R. W. Christy, Physical Review B **6**, 4370 (1972).

[124] A. M. Smith, M. C. Mancini, and S. Nie, Nature Nanotechnology **4**, 710 (2009).

[125] S. Eustis and M. A. El-Sayed, Chemical Society Reviews **35**, 209 (2006).

[126] C. Sönnichsen, T. Franzl, T. Wilk, G. von Plessen, and J. Feldmann, New Journal of Physics **4**, 93 (2002).

[127] J. E. Curtis, B. A. Koss, and D. G. Grier, Optics Communications **207**, 169 (2002).

[128] G. Tricoles, Applied Optics **26**, 4351 (1987).

[129] A. M. Weiner, Review of Scientific Instruments **71**, 1929 (2000).

[130] E. R. Dufresne, G. C. Spalding, M. T. Dearing, S. A. Sheets, and D. G. Grier, Review of Scientific Instruments **72**, 1810 (2001).

[131] S. W. Hell and J. Wichmann, Optics Letters **19**, 780 (1994).

[132] T. J. Gould, D. Burke, J. Bewersdorf, and M. J. Booth, Optics Express **20**, 20998 (2012).

[133] H. Ma, Z. Liu, P. Zhou, X. Wang, Y. Ma, and X. Xu, Journal of Optics **12**, 045704 (2010).

[134] O. Bryngdahl and F. Wyrowski, Progress in Optics **28**, 1 (1990).

[135] A. Ohlinger, S. Nedev, A. A. Lutich, and J. Feldmann, Nano letters **11**, 1770 (2011).

[136] Computer-integrated systems for microoscopy and manipulation at unc-ch, supported by the nih nibib (accessed 2016).

[137] R. Parthasarathy, Nature Methods **9**, 724 (2012).

[138] S. Youssef, S. Gude, and J. O. Rädler, Integrative Biology **3**, 1095 (2011).

[139] M. V. Kristensen, P. Ahrendt, T. B. Lindballe, O. H. A. Nielsen, A. P. Kylling, H. Karstoft, A. Imparato, L. Hosta-Rigau, B. Stadler, H. Stapelfeldt, and et al., Optics Express **20**, 1953 (2012).

[140] C. R. Roeske, *Entwicklung einer lasermikroskopischen Methode zur mechanischen Analyse von Vesikeln*, Bachelor's thesis, LMU Munich (2015).

[141] F. Winterer, *Manipulation of Plasmonic Nanoparticles by Optically Driven Thermal Convection*, Master's thesis, LMU Munich (2015).

[142] E. Sackmann, H.-P. Duwe, and H. Engelhardt, Faraday Discussions of the Chemical Society **81**, 281 (1986).

[143] W. Helfrich, Zeitschrift für Naturforschung C **28**, 693 (1973).

[144] R. M. Hochmuth, Journal of Biomechanics **33**, 15 (2000).

[145] M. J. Brett and M. M. Hawkeye, Science **319**, 1192 (2008).

[146] A. Ghosh and P. Fischer, Nano Letters **9**, 2243 (2009).

[147] E. Sackmann, Science **271**, 43 (1996).

[148] W. C. Lin, C. H. Yu, T. S, and J. T. Groves, Current Protocols in Chemical Biology **2**, 235 (2010).

[149] M. I. Angelova and D. S. Dimitrov, Faraday Discussions of the Chemical Society **81**, 303 (1986).

[150] M. I. Angelova, S. Soléau, P. Méléard, F. Faucon, and P. Bothorel, *Progress in Colloid & Polymer Science*, 127–131 (Springer Nature, 1992).

[151] S. Braig, B. U. S. Schmidt, K. Stoiber, C. Händel, T. Möhn, O. Werz, R. Müller, S. Zahler, A. Koeberle, J. A. Käs, and A. M. Vollmar, New Journal of Physics **17**, 083007 (2015).

[152] J. A. Frank, D. A. Yushchenko, D. J. Hodson, N. Lipstein, J. Nagpal, G. A. Rutter, J.-S. Rhee, A. Gottschalk, N. Brose, C. Schultz, and D. Trauner, Nature Chemical Biology **12**, 755 (2016).

[153] C. Pernpeintner, J. A. Frank, P. Urban, C. R. Roeske, S. D. Pritzl, D. Trauner, and T. Lohmüller, Langmuir **33**, 4083 (2017).

[154] S. Suresh, Acta Materialia **55**, 3989 (2007).

[155] E. Paluch and C.-P. Heisenberg, Current Biology **19**, 790 (2009).

[156] U. S. Eggert, T. J. Mitchison, and C. M. Field, Annual Review of Biochemistry **75**, 543 (2006).

[157] H. T. McMahon and J. L. Gallop, Nature **438**, 590 (2005).

[158] E. Paluch, C. Sykes, J. Prost, and M. Bornens, Trends in Cell Biology **16**, 5 (2006).

[159] N. Elkhatib, M. B. Neu, C. Zensen, K. M. Schmoller, D. Louvard, A. R. Bausch, T. Betz, and D. M. Vignjevic, Current Biology **24**, 1492 (2014).

[160] G. G. Borisy and T. M. Svitkina, Current Opinion in Cell Biology **12**, 104 (2000).

[161] S. M. Rafelski and J. A. Theriot, Annual Review of Biochemistry **73**, 209 (2004).

[162] K. Trajkovic, C. Hsu, S. Chiantia, L. Rajendran, D. Wenzel, F. Wieland, P. Schwille, B. Brugger, and M. Simons, Science **319**, 1244 (2008).

[163] S. Abounit and C. Zurzolo, Journal of Cell Science **125**, 1089 (2012).

[164] R. Bar-Ziv, T. Tlusty, E. Moses, S. A. Safran, and A. Bershadsky, Proceedings of the National Academy of Sciences **96**, 10140 (1999).

[165] M. Théry and M. Bornens, Current Opinion in Cell Biology **18**, 648 (2006).

[166] S. Singer and G. L. Nicolson, Membranes and Viruses in Immunopathology; Day, SB, Good, RA, Eds 7–47 (1972).

[167] O. G. Mouritsent and K. Jørgensen, Molecular Membrane Biology **12**, 15 (1995).

[168] E. Sackmann, FEBS Letters **346**, 3 (1994).

[169] J. N. Israelachvili, *Intermolecular and Surface Forces* (Elsevier, 2011).

[170] P. Walde, K. Cosentino, H. Engel, and P. Stano, ChemBioChem **11**, 848 (2010).

[171] M. Tate, E. Eikenberry, D. Turner, E. Shyamsunder, and S. Gruner, Chemistry and Physics of Lipids **57**, 147 (1991).

[172] R. Dimova, S. Aranda, N. Bezlyepkina, V. Nikolov, K. A. Riske, and R. Lipowsky, Journal of Physics: Condensed Matter **18**, 1151 (2006).

[173] U. Seifert, Advances in Physics **46**, 13 (1997).

[174] H. Deuling and W. Helfrich, Journal de Physique **37**, 1335 (1976).

[175] H. Yuan, C. Huang, and S. Zhang, Soft Matter **6**, 4571 (2010).

[176] S. Svetina and B. Žekš, European Biophysics Journal **17**, 101 (1989).

[177] L. Miao, U. Seifert, M. Wortis, and H.-G. Döbereiner, Physical Review E **49**, 5389 (1994).

[178] A. J. Markvoort, R. A. van Santen, and P. A. J. Hilbers, The Journal of Physical Chemistry B **110**, 22780 (2006).

[179] U. Seifert, K. Berndl, and R. Lipowsky, Physical Review A **44**, 1182 (1991).

[180] Q. Li, G. Lee, C. Ong, and C. Lim, Biochemical and Biophysical Research Communications **374**, 609 (2008).

[181] F. M. Menger and M. I. Angelova, Accounts of Chemical Research **31**, 789 (1998).

[182] H. Döbereiner, J. Käs, D. Noppl, I. Sprenger, and E. Sackmann, Biophysical Journal **65**, 1396 (1993).

[183] R. Lipowsky, Nature **349**, 475 (1991).

[184] Y. Yu and S. Granick, Journal of the American Chemical Society **131**, 14158 (2009).

[185] R. Bar-Ziv, E. Moses, and P. Nelson, Biophysical Journal **75**, 294 (1998).

[186] C. Ménager, D. Guemghar, R. Perzynski, S. Lesieur, and V. Cabuil, Langmuir **24**, 4968 (2008).

[187] K. P. Sinha, S. Gadkari, and R. M. Thaokar, Soft Matter **9**, 7274 (2013).

[188] R. Dimova, N. Bezlyepkina, M. D. Jordö, R. L. Knorr, K. A. Riske, M. Staykova, P. M. Vlahovska, T. Yamamoto, P. Yang, and R. Lipowsky, Soft Matter **5**, 3201 (2009).

[189] J. Broichhagen, J. A. Frank, and D. Trauner, Accounts of Chemical Research **48**, 1947 (2015).

[190] W. A. Velema, W. Szymanski, and B. L. Feringa, Journal of the American Chemical Society **136**, 2178 (2014).

[191] J. M. Kuiper and J. B. F. N. Engberts, Langmuir **20**, 1152 (2004).

[192] H. Fujiwara and Y. Yonezawa, Nature **351**, 724 (1991).

[193] K. Ishii, T. Hamada, M. Hatakeyama, R. Sugimoto, T. Nagasaki, and M. Takagi, ChemBioChem **10**, 251 (2009).

[194] T. Hamada, Y. T. Sato, K. Yoshikawa, and T. Nagasaki, Langmuir **21**, 7626 (2005).

[195] T. Shima, T. Muraoka, T. Hamada, M. Morita, M. Takagi, H. Fukuoka, Y. Inoue, T. Sagawa, A. Ishijima, Y. Omata, T. Yamashita, and K. Kinbara, Langmuir **30**, 7289 (2014).

[196] X. Song, J. Perlstein, and D. G. Whitten, Journal of the American Chemical Society **119**, 9144 (1997).

[197] C.-H. Lee, W.-C. Lin, and J. Wang, Physical Review E **64**, 020901 (2001).

[198] G. Koster, A. Cacciuto, I. Derényi, D. Frenkel, and M. Dogterom, Physical Review Letters **94**, 068101 (2005).

[199] T. Bornschlögl, S. Romero, C. L. Vestergaard, J.-F. Joanny, G. T. V. Nhieu, and P. Bassereau, Proceedings of the National Academy of Sciences **110**, 18928 (2013).

[200] H. Fliegl, A. Köhn, C. Hättig, and R. Ahlrichs, Journal of the American Chemical Society **125**, 9821 (2003).

[201] D. G. Whitten, Accounts of Chemical Research **26**, 502 (1993).

[202] B. Alberts, A. Johnson, J. Lewis, M. Raff, K. Roberts, and P. Walter, *Molecular biology of the cell* (Garland Science, 2008).

[203] M. Leaver, P. Domínguez-Cuevas, J. M. Coxhead, R. A. Daniel, and J. Errington, Nature **457**, 849 (2009).

[204] H. Kress, E. H. K. Stelzer, D. Holzer, F. Buss, G. Griffiths, and A. Rohrbach, Proceedings of the National Academy of Sciences **104**, 11633 (2007).

[205] S. Romero, A. Quatela, T. Bornschlogl, S. Guadagnini, P. Bassereau, and G. Tran Van Nhieu, Journal of Cell Science **125**, 4999 (2012).

[206] A. R. Bausch and K. Kroy, Nature Physics **2**, 231 (2006).

[207] I. A. Chen, Current Biology **19**, 327 (2009).

[208] S. Suresh, J. Spatz, J. Mills, A. Micoulet, M. Dao, C. Lim, M. Beil, and T. Seufferlein, Acta Biomaterialia **1**, 15 (2005).

[209] G. Y. Lee and C. T. Lim, Trends in Biotechnology **25**, 111 (2007).

[210] S. S. An, B. Fabry, X. Trepat, N. Wang, and J. J. Fredberg, American Journal of Respiratory Cell and Molecular Biology **35**, 55 (2006).

[211] F. Michor, J. Liphardt, M. Ferrari, and J. Widom, Nature Reviews Cancer **11**, 657 (2011).

[212] S. Suresh, Nature Nanotechnology **2**, 748 (2007).

[213] S. E. Cross, Y.-S. Jin, J. Rao, and J. K. Gimzewski, Nature Nanotechnology **2**, 780 (2007).

[214] C. Zensen, I. E. Fernandez, O. Eickelberg, J. Feldmann, and T. Lohmüller, Advanced Science **4**, 1600238 (2016).

[215] K. König, Histochemistry and Cell Biology **114**, 79 (2000).

[216] M. Dao, C. Lim, and S. Suresh, Journal of the Mechanics and Physics of Solids **51**, 2259 (2003).

[217] R. Hochmuth and R. Waugh, Annual Review of Physiology **49**, 209 (1987).

[218] E. Evans, Biophysical Journal **43**, 27 (1983).

[219] S. Hénon, G. Lenormand, A. Richert, and F. Gallet, Biophysical Journal **76**, 1145 (1999).

[220] R. Rand and A. Burton, Biophysical Journal **4**, 115 (1964).

[221] Y. Tan, D. Sun, J. Wang, and W. Huang, IEEE Transactions on Biomedical Engineering **57**, 1816 (2010).

[222] S. Rancourt-Grenier, M.-T. Wei, J.-J. Bai, A. Chiou, P. P. Bareil, P.-L. Duval, and Y. Sheng, Optics Express **18**, 10462 (2010).

[223] L. Landau and E. Lifshitz, *Theory of Elasticity*, vol. 7 (Butterworth-Heinemann, 1986).

[224] K. Menard, *Dynamic Mechanical Analysis - A Practical Analysis* (CRC Press, 2008), 2nd ed.

[225] X. Cai, J. Luo, X. Yang, H. Deng, J. Zhang, S. Li, H. Wei, C. Yang, L. Xu, R. Jin, Z. Li, W. Zhou, J. Ding, J. Chu, L. Jia, Q. Jia, C. Tan, M. Liu, and J. Xiao, Oncotarget **6**, 22905 (2015).

[226] J. Guck, S. Schinkinger, B. Lincoln, F. Wottawah, S. Ebert, M. Romeyke, D. Lenz, H. M. Erickson, R. Ananthakrishnan, D. Mitchell, J. Käs, S. Ulvick, and C. Bilby, Biophysical Journal **88**, 3689 (2005).

[227] W. Xu, R. Mezencev, B. Kim, L. Wang, J. McDonald, and T. Sulchek, PLoS ONE **7**, 46609 (2012).

[228] M. Plodinec, M. Loparic, C. A. Monnier, E. C. Obermann, R. Zanetti-Dallenbach, P. Oertle, J. T. Hyotyla, U. Aebi, M. Bentires-Alj, R. Y. H. Lim, and C.-A. Schoenenberger, Nature Nanotechnology **7**, 757 (2012).

[229] V. Swaminathan, K. Mythreye, E. T. O'Brien, A. Berchuck, G. C. Blobe, and R. Superfine, Cancer Research **71**, 5075 (2011).

[230] J. A. Cribb, L. D. Osborne, K. Beicker, M. Psioda, J. Chen, E. T. O'Brien, R. M. Taylor II, L. Vicci, J. P.-L. Hsiao, C. Shao *et al.*, Scientific reports **6** (2016).

[231] O. Otto, P. Rosendahl, A. Mietke, S. Golfier, C. Herold, D. Klaue, S. Girardo, S. Pagliara, A. Ekpenyong, A. Jacobi *et al.*, Nature Methods **12**, 199 (2015).

[232] J. Guck, F. Lautenschläger, S. Paschke, and M. Beil, Integrative Biology **2**, 575 (2010).

[233] P. Paterlini-Brechot and N. L. Benali, Cancer Letters **253**, 180 (2007).

[234] K. Pantel, R. H. Brakenhoff, and B. Brandt, Nature Reviews Cancer **8**, 329 (2008).

[235] R. M. Hoffman, Nature Reviews Cancer **5**, 796 (2005).

[236] U. Neugebauer, T. Bocklitz, J. H. Clement, C. Krafft, and J. Popp, The Analyst **135**, 3178 (2010).

[237] M. Zürch, S. Foertsch, M. Matzas, K. Pachmann, R. Kuth, and C. Spielmann, Journal of Medical Imaging **1**, 031008 (2014).

[238] V. P. Zharov, E. I. Galanzha, E. V. Shashkov, N. G. Khlebtsov, and V. V. Tuchin, Optics Letters **31**, 3623 (2006).

[239] J. Chen, J. Li, and Y. Sun, Lab on a Chip **12**, 1753 (2012).

[240] G. A. Wagnieres, W. M. Star, and B. C. Wilson, Photochemistry and Photobiology **68**, 603 (1998).

[241] K. Vishwanath and N. Ramanujam, *Fluorescence Spectroscopy In Vivo* (Wiley, 2000).

[242] D. Desmaele, M. Boukallel, and S. Régnier, Journal of Biomechanics **44**, 1433 (2011).

[243] K. E. Kasza, A. C. Rowat, J. Liu, T. E. Angelini, C. P. Brangwynne, G. H. Koenderink, and D. A. Weitz, Current Opinion in Cell Biology **19**, 101 (2007).

[244] D.-H. Kim, P. K. Wong, J. Park, A. Levchenko, and Y. Sun, Annual Review of Biomedical Engineering **11**, 203 (2009).

[245] D. Wirtz, K. Konstantopoulos, and P. C. Searson, Nature Reviews Cancer **11**, 512 (2011).

[246] T. Yeung, P. C. Georges, L. A. Flanagan, B. Marg, M. Ortiz, M. Funaki, N. Zahir, W. Ming, V. Weaver, and P. A. Janmey, Cell Motility and the Cytoskeleton **60**, 24 (2004).

[247] Y.-T. Hsiao, J.-H. Wang, Y.-C. Hsu, C.-C. Chiu, C.-J. Lo, C.-W. Tsao, and W. Y. Woon, Applied Physics Letters **100**, 203702 (2012).

[248] N. C. Darnton, L. Turner, S. Rojevsky, and H. C. Berg, Biophysical Journal **98**, 2082 (2010).

[249] J. Kim, H.-S. Kim, S. Han, J.-Y. Lee, J.-E. Oh, S. Chung, and H.-D. Park, Lab on a Chip **13**, 1846 (2013).

[250] X. Trepat, L. Deng, S. S. An, D. Navajas, D. J. Tschumperlin, W. T. Gerthoffer, J. P. Butler, and J. J. Fredberg, Nature **447**, 592 (2007).

[251] J. Hescheler and R. Speicher, European Biophysics Journal **17**, 273 (1989).

[252] S. Schreppler, N. Spethmann, N. Brahms, T. Botter, M. Barrios, and D. M. Stamper-Kurn, Science **344**, 1486 (2014).

[253] D. B. Phillips, S. H. Simpson, J. A. Grieve, R. Bowman, G. M. Gibson, M. J. Padgett, J. G. Rarity, S. Hanna, M. J. Miles, and D. M. Carberry, Europhysics Letters **99**, 58004 (2012).

[254] D. B. Phillips, G. M. Gibson, R. Bowman, M. J. Padgett, S. Hanna, D. M. Carberry, M. J. Miles, and S. H. Simpson, Optics Express **20**, 29679 (2012).

[255] M. R. Pollard, S. W. Botchway, B. Chichkov, E. Freeman, R. N. J. Halsall, D. W. K. Jenkins, I. Loader, A. Ovsianikov, A. W. Parker, and R. Stevens, New Journal of Physics **12**, 113056 (2010).

[256] N. Villadsen, D. Ø. Andreasen, J. Hagelskjær, J. Thøgersen, A. Imparato, and S. R. Keiding, Optics Express **23**, 13141 (2015).

[257] A. Rohrbach, Optics Express **13**, 9695 (2005).

[258] O. M. Marago, P. H. Jones, F. Bonaccorso, V. Scardaci, P. G. Gucciardi, A. G. Rozhin, and A. C. Ferrari, Nano Letters **8**, 3211 (2008).

[259] C. Zensen, N. Villadsen, F. Winterer, S. R. Keiding, and T. Lohmüller, Applied Physics Letters Photonics **1**, 026102 (2016).

[260] A. Rohrbach and E. H. K. Stelzer, Journal of the Optical Society of America A, Optics and Image Science **18**, 839 (2001).

[261] M. Dienerowitz, M. Mazilu, P. J. Reece, T. F. Krauss, and K. Dholakia, Optics Express **16**, 4991 (2008).

[262] A. O. Govorov, W. Zhang, T. Skeini, H. Richardson, J. Lee, and N. A. Kotov, Nanoscale Research Letters **1**, 84 (2006).

[263] A. O. Govorov and H. H. Richardson, Nano Today **2**, 30 (2007).

[264] M. Toshimitsu, Y. Matsumura, T. Shoji, N. Kitamura, M. Takase, K. Murakoshi, H. Yamauchi, S. Ito, H. Miyasaka, A. Nobuhiro, Y. Mizumoto, H. Ishihara, and Y. Tsuboi, The Journal of Physical Chemistry C **116**, 14610 (2012).

[265] M. Perner, P. Bost, U. Lemmer, G. von Plessen, J. Feldmann, U. Becker, M. Mennig, M. Schmitt, and H. Schmidt, Physical Review Letters **78**, 2192 (1997).

[266] M. Fedoruk, M. Meixner, S. Carretero-Palacios, T. Lohmüller, and J. Feldmann, ACS Nano **7**, 7648 (2013).

[267] Tech. rep., The International Association for the Properties of Water and Steam (2008).

[268] S. Babar and J. H. Weaver, Applied Optics **54**, 477 (2015).

[269] H.-J. Hagemann, W. Gudat, and C. Kunz, The Journal of the Optical Society of America **65**, 742 (1975).

[270] A. D. Rakic, A. B. Djurisic, J. M. Elazar, and M. L. Majewski, Applied Optics **37**, 5271 (1998).

[271] M. Mansuripur, Optics Express **12**, 5375 (2004).

[272] J. P. Barton, D. R. Alexander, and S. A. Schaub, Journal of Applied Physics **66**, 4594 (1989).

[273] R. L. Olmon, B. Slovick, T. W. Johnson, D. Shelton, S.-H. Oh, G. D. Boreman, and M. B. Raschke, Physical Review B **86**, 235147 (2012).

[274] P. Waterman, Proceedings of the IEEE **53**, 805 (1965).

[275] M. I. Mishchenko, L. D. Travis, and D. W. Mackowski, Journal of Quantitative Spectroscopy and Radiative Transfer **55**, 535 (1996).

[276] D. Huh, W. Gu, Y. Kamotani, J. B. Grotberg, and S. Takayama, Physiological Measurement **26**, 73 (2005).

[277] M. F. Copeland and D. B. Weibel, Soft Matter **5**, 1174 (2009).

[278] M. Kim and T. R. Powers, Physical Review E **69**, 061910 (2004).

[279] R. Stocker, J. R. Seymour, A. Samadani, D. E. Hunt, and M. F. Polz, Proceedings of the National Academy of Sciences **105**, 4209 (2008).

[280] K. Drescher, J. Dunkel, L. H. Cisneros, S. Ganguly, and R. E. Goldstein, Proceedings of the National Academy of Sciences **108**, 10940 (2011).

[281] N. Darnton, L. Turner, K. Breuer, and H. C. Berg, Biophysical Journal **86**, 1863 (2004).

[282] L. Paterson, Science **292**, 912 (2001).

[283] S. Franke-Arnold, L. Allen, and M. Padgett, Laser & Photonics Review **2**, 299 (2008).

[284] S. J. Parkin, G. Knöner, T. A. Nieminen, N. R. Heckenberg, and H. Rubinsztein-Dunlop, Physical Review E **76** (2007).

[285] R. C. Gauthier, Applied Physics Letters **67**, 2269 (1995).

[286] A. Yamamoto and I. Yamaguchi, Japanese Journal of Applied Physics **34**, 3104 (1995).

[287] S. Kirchner, *Focused optical beams for driving and sensing helical and biological microobjects*, Ph.D. thesis, LMU Munich (2015).

[288] G. Knöner, S. Parkin, N. R. Heckenberg, and H. Rubinsztein-Dunlop, Physical Review E **72**, 031507 (2005).

[289] D. Walker, M. Kübler, K. I. Morozov, P. Fischer, and A. M. Leshansky, Nano Letters **15**, 4412 (2015).

[290] A. Persat, C. D. Nadell, M. K. Kim, F. Ingremeau, A. Siryaporn, K. Drescher, N. S. Wingreen, B. L. Bassler, Z. Gitai, and H. A. Stone, Cell **161**, 988 (2015).

[291] E.-L. Florin, A. Pralle, J. Heinrich Hörber, and E. H. Stelzer, Journal of Structural Biology **119**, 202 (1997).

[292] A. Pralle, E.-L. Florin, E. H. Stelzer, and J. H. Hörber, Single Molecules **1**, 129 (2000).

[293] L. Ikin, D. M. Carberry, G. M. Gibson, M. J. Padgett, and M. J. Miles, New Journal of Physics **11**, 023012 (2009).

[294] P. V. Ruijgrok, N. R. Verhart, P. Zijlstra, A. L. Tchebotareva, and M. Orrit, Physical Review Letters **107**, 037401 (2011).

[295] J. M. Tsay, S. Doose, and S. Weiss, Journal of the American Chemical Society **128**, 1639 (2006).

[296] K. Luby-Phelps, *International Review of Cytology*, 189–221 (Elsevier, 1999).

[297] D. Wirtz, Annual Review of Biophysics **38**, 301 (2009).

[298] M. Li, *Optical Cellular Delivery and Intracellular Sensing of fN Forces Using Gold Nanoparticles*, Ph.D. thesis, LMU Munich (2016).

[299] S. J. Ebbens and J. R. Howse, Soft Matter **6**, 726 (2010).

[300] W. Wang, W. Duan, S. Ahmed, T. E. Mallouk, and A. Sen, Nano Today **8**, 531 (2013).

[301] P. Fischer and A. Ghosh, Nanoscale **3**, 557 (2011).

[302] A. Ghosh, D. Paria, H. J. Singh, P. L. Venugopalan, and A. Ghosh, Physical Review E **86**, 031401 (2012).

[303] E. Sackmann and R. Merkel, *Lehrbuch der Biophysik* (Wiley-VCH, 2010).

[304] M. Reichert and H. Stark, The European Physical Journal E **17**, 493 (2005).

[305] C. Battle, C. P. Broedersz, N. Fakhri, V. F. Geyer, J. Howard, C. F. Schmidt, and F. C. MacKintosh, Science **352**, 604 (2016).

[306] T. B. Lindballe, *The counter-propagating optical trap: Characterization and pulsed laser manipulation of trapped objects*, Ph.D. thesis, Aarhus University (2012).

[307] Y. Seol, A. E. Carpenter, and T. T. Perkins, Optics Letters **31**, 2429 (2006).

[308] M. T. Carlson, A. J. Green, and H. H. Richardson, Nano Letters **12**, 1534 (2012).

[309] M. Li, T. Lohmüller, and J. Feldmann, Nano Letters **15**, 770 (2015).

List of Abbreviations and Variables

ADC	analog-igital conversion
CCD	charge-coupled device
CW	continuous wave
CFCS	cell-fluid coupling spectroscopy
CGH	computer-generated hologram
DAC	digital-analog conversion
DFC	dark-field condenser
DLS	dynamic light scattering
FCS	fetal calf serum
FFT	Fast Fourier transformation
GLMT	Generalized Lorenz-Mie theory
GUI	graphical user interface
GUV	giant unilamellar vesicle
HOT	holographic optical tweezers
LED	light-emitting diode
LMU	Ludwig Maximilians-Universität
LP	long-pass (filter)
LUV	large unilamellar vesicle
MSD	mean squared displacement
NA	numerical aperture
NF	notch filter
NIR	near-infrared
PBS	phosphate buffered saline
PEG	polyethyleneglycole
PSD	power spectral density
RBC	red blood cell
SLM	Spatial Light Modulator
SUV	small unilamellar vesicle
UV	ultra-violet

A		absorption
α	$= \alpha' + i \cdot \alpha''$	complex polarizability
$\mathbf{B}$		magnetic flux density
c	$299\,792\,458\,\mathrm{m\,s^{-1}}$	speed of light in vacuum
δ_{ij}		Kronecker delta
d		dimensionality
D	$= \frac{k_B T}{\gamma}$	diffusion constant
D_α		generalized diffusion constant
E		Young's modulus
$\mathbf{E}$		electrical field
E_{stretch}		stretching energy
ϵ		dielectric constant
ϵ_0	$8.854\,187 \times 10^{-12}\,\mathrm{F\,m^{-1}}$	dielectric constant of the vacuum
F		curvature energy
$\mathbf{f}_{\mathrm{cell}}$	$= \mathbf{f}_{\mathrm{cell}}^{(1)} * \mathbf{f}_{\mathrm{cell}}^{(2)} * \ldots$	analog cell filter
$\mathbf{f}_{\mathrm{trans}}$		transmission filter
F_{drag}		drag force
F_{ext}		external force
F_{grad}		drag force
F_{harmonic}		spring force
F_{rp}		radiation pressure
F_{scatt}		scattering force
γ		damping constant, drag coefficient
η		dynamic viscosity
η_W		viscosity of water
η_m		hypotonic dilution parameter
f_0	$= \frac{1}{2\pi}\sqrt{\frac{\kappa}{m}}$	mechanical resonance frequency
f_c	$= \frac{\kappa}{2\pi\gamma}$	corner frequency
G		Oseen tensor
G_{field}		field momentum
G_{mech}		mechanical momentum
h_e		elastic thickness
$\mathbf{H}$		magnetic field intensity
$\mathbf{I}$		input signal vector
k_B		$1.380\,64 \times 10^{-23}\,\mathrm{J/K}$ Boltzmann constant
κ		trap stiffness
$\kappa_B, \kappa_G, \kappa_S$		mean, Gaussian, spontaneous bending rigidity

L		length
$\mathbf{L}$		angular momentum
λ		wavelength
m		particle mass
μ		magnetic susceptibility
μ_0	$1.256\,637 \times 10^{-6}\,\mathrm{N\,A^{-2}}$	magnetic permeability of the vacuum
N		number of particles
n		refractive index
ν_p		Poisson ratio
p		pressure
p_{rp}		radiation pressure
$\mathbf{p}$		dipole moment
Ψ		spherical wavefunction
Q		quality factor
ρ		density
r		radius
R		reflectivity
Re		Reynolds number
$S\left(f\right)$		power spectral density
$\mathbf{S}$		Poynting vector
$\mathbf{S}_{\mathrm{det}}$	$= (S_1, S_2, S_3, \ldots)$	Fourier peak signal vector
σ		standard deviation
σ_{scatt}		scattering cross-section
T		temperature
$\mathbb{T}$		Maxwell's stress tensor
t_{m}		measured time
t_{mom}	$= \frac{m}{\gamma}$	momentum relaxation time
t_{p}		period length
t_{tr}	$= \frac{\gamma}{\kappa}$	trap relaxation time
T		transmission
v		velocity, flow speed
V		volume
ω		angular frequency
$\xi\left(t\right)$		thermal/stochastic force

Acknowledgments

The last three and a half years have been a wonderful time for me, both scientifically and personally. Many people were involved in this and I would like to thank all of them for their friendship, help, time, guidance and understanding.

First of all, I would like to thank Dr. **Theo Lohmüller** who supervised my PhD thesis. We had so many fruitful, enjoyable, productive, and even heated discussions that always brought forward our common research. I think we made up an excellent tandem and really hope he thinks the same. Theo teached me a lot about science, scientific writing and presenting. I further want to thank Theo for the great and unique atmosphere he was able to create in our subgroup and the *photoswitches group* which, for me, is the basis of scientific progress. Finally, he was always receptive to listening (and solving!) all kinds of problems.

I want to thank Prof. Dr. **Jochen Feldmann** for giving me the opportunity to conduct my research in his group. I would like to thank him for the support to present and share my results within the scientific community and the chance to be part of the NIM graduate program.

Many thanks to the scientists I was allowed to cooperate with. In particular, I want to thank Dr. **Naja Villadsen** and Prof. Dr. **Søren Keiding** from Aarhus University (Denmark) for a very productive and intense cooperation. With Naja, I spent hours and hours just pushing particles and programming Matlab code and we're still friends. Further, the cooperation with Dr. **James Frank** and Prof. Dr. **Dirk Trauner** was extremely pleasant, including high quality scientific discussions and great samples. Apart from that, James helped very much in improving the writing of manuscripts and abstracts. I wish him all the best for his scientific career. Finally, I want to thank Prof. Dr. **Oliver Eickelberg** and Dr. **Simone Braig** for the fruitful collaboration, inspiring discussions and reliable samples.

Special thanks to **Christoph Maier** and **Patrick Urban** for the excellent teamwork and the great fun we had in the lab, in the coffee kitchen and as an *Admin Team*. They have contributed significantly to my thesis. I want to thank **Felix Winterer**, **Christian Roeske** and **Stefanie Pritzl** whom I had the chance to work with during their Master theses. I wish Steffi all the best for continuing some of this work in her PhD.

Thanks a lot to our PhD student generation, especially **Christoph Maier**, **Patrick Urban**, **Verena Hintermayr**, **Aurora Manzi** and **Florian Ehrat** for the great time together and your friendship, during and after work. With the members of the *Golden Circle*, we had an excellent time in Sicily which we will hopefully repeat! Thank you Dr. **Sabrina Simoncelli**, Dr. **Silke Kirchner**, Dr. **Miao Li**, **Jasmina Sichert** and **Thomas Simon** for the enjoyable time together and for always motivating me in your very special ways.

I cordially thank **Gerlinde Adam**, **Stefan Niedermaier** and **Christian Holopirek** for their support with administrative and technical questions. Thanks to all assistants, PostDocs, PhD, Master and Bachelor students in the group for providing a very friendly and pleasant atmosphere and for any help you provided me.

Last but certainly not least, I want to thank my parents **Monika** and **Wilfried Zensen**, my sister **Nina** and my brother **Richard** for always backing me up and for their love. Special thanks to my father for inspiring me to study physics in his very own way and my mother for her support and patient proofreading. The final extra big thank you goes to my husband **Matthias Pernpeintner**, for listening to and understanding of small and big problems, including those in nanomechanics and semiconductor physics, and also for just being there.